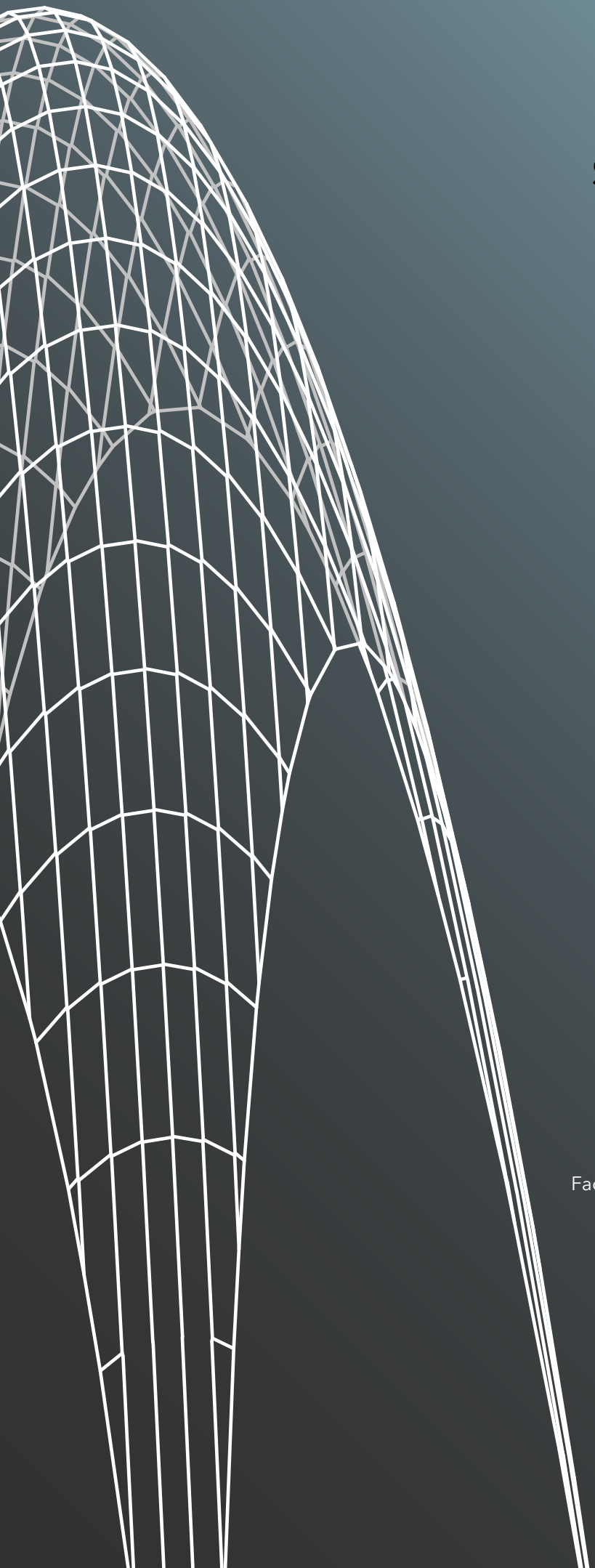

SHELL STRUCTURES

On the relationship between moment hills, stress functions and thrust surfaces in the design of shell structures

MSC GRADUATION THESIS

Delft University of Technology

Faculty of Architecture & the Built Environment

Master track Building Technology

Pim Buskermolen

January 29, 2018

Delft University of Technology
Faculty of Architecture & The Built Environment
Department of Architectural Engineering & Technology (AE&T)
Julianalaan 134, 2628 BL Delft

Pim Buskermolen (author)
Student number: 4219228

Members of the graduation committee:

Ir. A. Borgart (first mentor)
Department of Structural Mechanics

Dr. M. Turrin (second mentor)
Department of Design Informatics

Drs. A. Mulder (graduation committee)
Department of Architecture

TU Delft

ABSTRACT

This thesis aims to provide a better understanding on the relationship between the mechanical and geometrical properties of shell structures. In search hereof, an attempt is made to describe the thrust surface; a geometrical representation of the in-plane force trajectories through a structure. There exists a well-known relation between the parabolic shape of a (two-dimensional) catenary and the moment line of a simply-supported beam subjected to a distributed load, a relation which is similar to the three-dimensional case of shell structures. In this thesis, this relation is further exploited in the creation of various shell structures, using the moment hill of various simple plate cases. The moment hills of twistless plates as shell structures pose promising results with respect to shell-like behaviour. In the process of generating shell structures from moment hills of twistless plates, establishing the correct boundary conditions has proven to be essential in obtaining shell geometry with maximum shell-like behaviour. The Airy stress function is utilised to get further insight into the mechanical behaviour of shells. Exploiting the reciprocal relation between this Airy stress function and the diagram of forces allowed for both the design and analysis of shells. Taking the reciprocal figure of a discretised version of the Airy stress function results in a force polyhedron which by nature is in equilibrium. It was proven that the rules of graphic statics apply here, the angular defect between two planes then act as force vectors. By means of the force polyhedron a distinction can be made between tensile and compressive forces through any structure. Calculating the angular defect in an edge of the Airy stress polyhedron results in the force through its corresponding edge in its reciprocal figure. This thesis proposes multiple parametric tools with which the reciprocal figure of any Airy stress function can be created. These tools provide insight in the structural behaviour of a shell structure, and aid in the design of shells in the preliminary design stage.

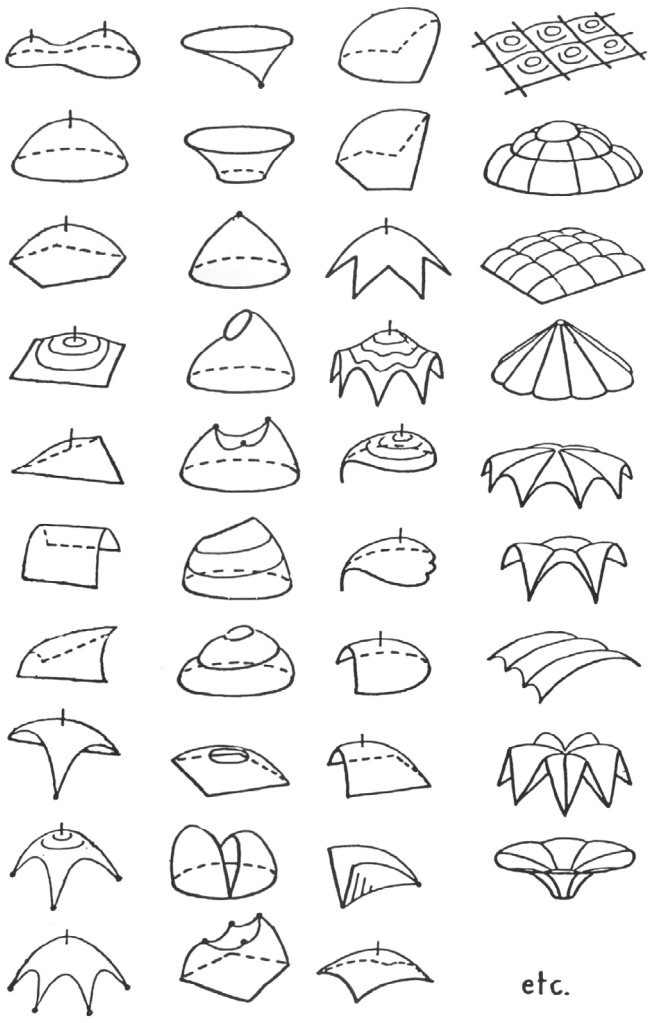
etc.

TABLE OF CONTENTS

GLOSSARY

K	Gaussian curvature
g	Change of Gaussian curvature
κ_{xx}, κ_{yy}, κ_{xy}	Curvature caused by bending moments
ε_{xx}, ε_{yy}, ε_{xy}	Normal strains
n_{xx}, n_{yy},n_{xy}	Membrane forces
m_{xx}, m_{yy}, m_{xy}	Bending moments
$\bar{M}$	Reduced sum of bending moments
ν	Poisson's ratio
γ	Shear strains
σ	Normal stress
τ	Shear stress
Γ	Primal grid
Γ^*	Dual grid
ζ	Scale factor
k	Principal curvature
R	Radius
φ	Angle
ϕ	Airy stress function
q	Distributed force (*across a line*)
p	Distributed force (*across a surface*)
w	Displacement (*perpendicular to surface*)
V	Vertex
E	Edge
P	Plane

1. INTRODUCTION

1 INTRODUCTION

1.1 BACKGROUND

1.1.1 FUNICULAR STRUCTURES

Structures are considered funicular if they act solely in compression or tension for a given loading (Block, 2009). Heinz Isler suggested 39 shapes for funicular vaults, ending with *"etc."* to demonstrate the unlimited possibilities (Isler, 1959). A two-dimensional cable, or a three-dimensional cable-net structure are examples of funicular systems, since they can only take up tensile forces. This occurrence can clearly be observed in hanging models, which are only loaded by their own weight and assume a state of equilibrium. Robert Hooke (1675) explained the analogy between a hanging chain and an arch as early as 1748. Translated from Latin, his explanation reads: *"As hangs the flexible line, so but inverted will stand the rigid arch"*. A hanging chain forms a catenary that is in tension due to its own weight, analogous to an arch that stands in compression under its own weight (Figure 1.1).

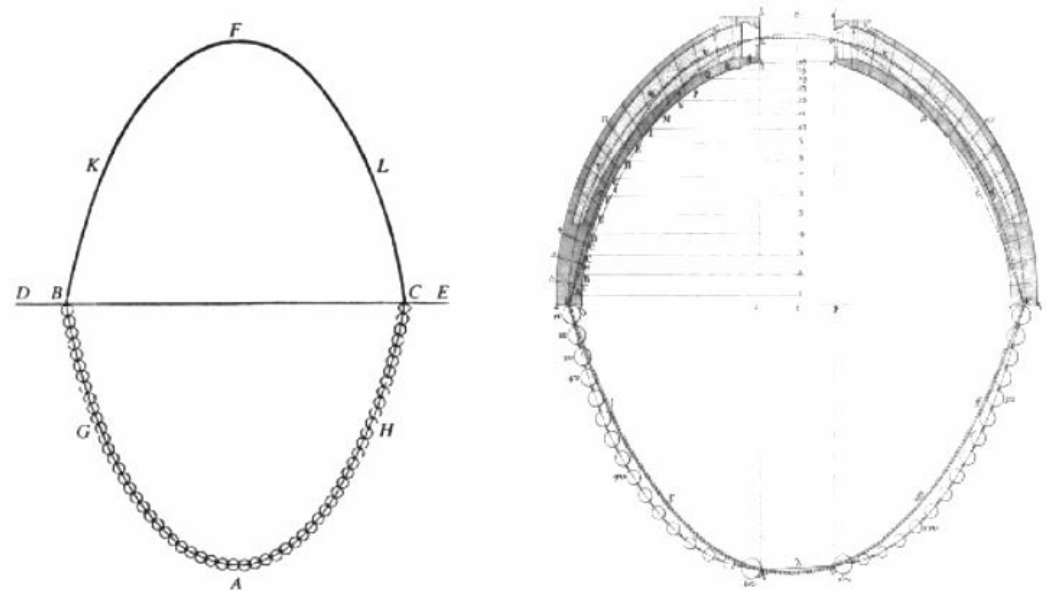

Figure 1.1: (a) hanging catenary that forms an arc when inverted, (b) analysis of the dome of St. Peter's basilica by Poleni (retrieved from: Block, De Jong, & Ochsendorf, 2006)

1.1.2 HISTORY OF SHELL STRUCTURES

In the 19th century, Antoni Gaudí applied hanging models as a method to design arches in buildings, and thus used the inverse relation between structures in tension and those in compression. Form-finding as such allowed Gaudí to design slender structures, because bending moments were minimised. Instead, primarily normal forces occurred that were transferred in-plane. More recent designers of funicular structures are engineer Heinz Isler and the architect Félix Candela, respectively known for (among others) the Recherswil Schale from 1965 (Figure 1.2) and l'Oceanogràfic in Valencia from 2003 (Figure 1.3).

1.1.3 METHODS FOR DESIGNING SHELL STRUCTURES

The hanging model proved an intuitive and helpful method for the design of shells. However, it is not commonly used nowadays. With the introduction of computational design and optimisation, it was considered obsolete. More recent methods have incorporated computation, such as the Force Density Method (FDM) and the finite element method (FEM). The former will be further elaborated in *3.4*. The latter, the finite element method, is nowadays the most commonly used method for structural analysis. It is however a very linear tool in its use, impeding application in the early design stages. It therefore does not prove useful in the preliminary design of shell structures.

Another method for analysing and designing shell structures is the Thrust Network Analysis method proposed by Philippe Block (2009). The thrust network is a network of nodes and branches, through which compression is absorbed. The coordinates of the nodes correspond with the shape of the funicular structure. This method, however, does not fully describe the relation between the mechanical and geometrical properties of such structures.

Figure 1.2: Recherswil Schale by Isler (retrieved from: Wikipedia)

Figure 1.3: L'Oceanogràfic in Valencia, designed by Félix Candela (retrieved from: Wikipedia)

1.1.4 THRUST SURFACE

The flow of forces through a shell structure is better explained and visualised by the thrust surface, a three-dimensional version of the thrust-line (Tiggeler, 2009). In two-dimensional structures a discrepancy between the thrust-line and the actual structure causes a bending moment, which is similar to the three-dimensional situation. Accordingly, a shell structure that is exactly the geometry of its thrust surface is expected to show minimal bending moments. Determining the thrust surface is therefore very interesting in the design of shell structures. A conclusive description of the geometry of the thrust surface for all shapes and boundary conditions does not exist yet.

1.2 CURRENT STATE OF RESEARCH

A lot of research on the structural behaviour of funicular structures has already been carried out. Heinz Isler (1926-2009), Frei Otto (1925-2015) and Félix Candela (1910-1997) applied graphic statics in the design of shell structures, enabling them to determine the optimal load paths. More theoretical research has been conducted by Christopher Calladine (University of Cambridge), and later Andrew Borgart (TU Delft) and Philippe Block (MIT), amongst many others.

Phillippe Block and his team have done extensive research on graphic statics for funicular (masonry) structures. The focus started in two-dimensional structures, but later evolved into three-dimensional structures. During his PhD studies, Block developed the Thrust Network Analysis, providing a method of designing funicular structures.

In his currently ongoing dissertation project, Borgart (my first mentor) aims to link the geometrical and mechanical properties of shell structures, in an effort to improve the understanding of their structural behaviour. He has also supported several MSc graduates in their graduation projects, forming a developing research over the years. This thesis continues on this established framework. The following perspectives have been taken so far:

- de Leuw, M. (2005): *'De steilste helling methode' (the steepest hill method): 'The influence of the geometry on the stress trajectories in randomly curved shells'*
- Tiggeler, L. (2009): *3D thrust-plane*
- Liem, Y. (2011): *Graphic statics in funicular design: calculating force equilibrium through complementary energy*
- van den Dool (2012): *Optimizing shell structures: by calculating the minimum complementary energy*
- van Dijk, N. (2014): *Graphic statics in arches and curved beams: finding force equilibrium through total complementary energy*
- Rozendaal, R. (2014): *Shells and arches: developing a new method to calculate shells and arches through graphic statics*
- Ros, J. (2017): *Graphically calculating arcs and shells by using the lowest complementary energy*

1.3 PROBLEM STATEMENT

Shell structures are highly statically indeterminate, making them difficult structures to calculate. Calculation of such structures requires indirect methods, such as the Finite Element Method (FEM). Such tools are often used by structural engineers nowadays, but have three main disadvantages (Borgart & Oosterhuis, 2010): firstly, FEM applications always offer discrete solutions as a result of the mathematical formulation that the method is based on. Secondly, the solution is no longer expressed in terms of parameters, but merely numerical; the solution is quantitative and no longer qualitative. Thirdly, the FEM method is not parametric; for every variance in geometry a new model has to be built.

At the same time, existing methods for assessing the thrust surface of funicular structures are either not feasible, or provide the designer with an infinite amount of possibilities, rather than a single optimal structure. No method exists yet that gives comprehensive insight in the structural behaviour of shell structures, or allows for use by designers in an early stage of the design process. These observations have lead to the following problem statement:

Problem:
'There is a lack of knowledge on the relation between the geometry and the mechanical behaviour of shell structures, resulting in challenges for the (structural) designer in the preliminary design stage of shells.'

Sub-problems:
- There exists no conclusive description of the thrust surface of shell structures.
- Existing structural analysis tools are mostly non-linear and are therefore difficult to use in the preliminary design stage of shell structures.
- Existing structural design tools return limited (visual) feedback on the mechanical behaviour of shell structures.

1.4 OBJECTIVES

This thesis aims to provide a better understanding of the structural behaviour of shell structures. With this knowledge, the goal is to create a parametric design tool, allowing designers to design shell structures in the early design stages. Also, the tool must allow for the assessment of the structural behaviour of existing shells. The tool shall be made so that it provides clear and comprehensive insight into the structural behaviour of the shell design. The main objective is stated as follows:

Main objective:
'Define the relation between geometrical and mechanical properties of shell structures, and with that develop a parametric design tool for shells.'

In order to achieve this objective, the following sub-objectives have been formulated:

Sub-objectives:
- Obtain a comprehensive understanding of the geometry of the thrust surface of shell structures.
- Develop a tool with which shell structures can be designed in the early design stage, which is intuitive to use and returns direct (graphical) feedback to the user.

1.4.1 FINAL PRODUCTS

Ultimately, this thesis will have as a result the following products:

- Description of the thrust surface geometry of shell structures with different boundary conditions.
- Parametric structural design tool for shells.

1.4.2 HYPOTHESIS

This research starts with new findings on the moment hill of a flat plate subjected to a projected load, relating it to the geometry of the thrust surface of a shell structure. From these findings the following hypothesis is formed, that will be used as starting point:

'An analogy is present between (1) the geometry of a moment hill of a plate and (2) the thrust surface of a shell subjected to a distributed load, and their boundary conditions are mutually related.'

1.5 RESEARCH QUESTIONS

In order to fulfil the main objective stated in *1.4*, the following research question is stated:

Main question:
'How can the relation between the geometrical and mechanical properties of shell structures be formulated and result in an intuitive and graphical design tool for (structural) designers?'

To allow for a conclusive answer to this question, the following sub-questions are formulated:

Sub-questions:
- How are the geometry and the thrust surface of a shell related to one another, and how can this relation be described?
- How can a parametric structural tool be developed to design shell structures?
- How can such a design tool be made intuitive and give (graphical) feedback to the user?

1.6 METHODOLOGY

This thesis provides an in-depth study into the theory behind shell geometry and its mechanics, as well as some geometric mathematics. These fields together later form the basis for the parametric design tool. The thesis is divided into six chapters, each of which corresponds chronologically with a phase in the research:

- *Introduction:* Introduces the topic and provides the reason behind writing this thesis. The objectives of the research are clarified here.
- *Theoretical framework:* General theory on structural mechanics as well as geometry is explained here. Different possible boundary conditions for loads, supports and materials are also explained.
- *Existing methods:* Different methods of assessing and designing shell structures are evaluated. In this chapter, relevant existing literature on the topic is assessed and summarised. This desktop research serves as a theoretical framework that forms the basis for the subsequent research.
- *Plate and shell analogies:* The hypothesis from *1.4.2* is first assessed. Together with the findings from the literature research, a better understanding and description of the thrust surface is explored. FEM will be applied to quickly review test results. Based on the results from this analogy, the end result is a proposed description of one or multiple shell types and their corresponding planes of thrust. Different geometrical shapes are hereby evaluated.
- *Parametric design tool:* The description from the previous section is translated into a design tool in Grasshopper. Input parameters are related to the desired shape of the final shell.
- *Conclusion:* This chapter contains the conclusions, recommendations and reflection of the thesis. It reviews the achievements of the research, and discusses possible future research topics.

1.7 RELEVANCE

Scientific relevance: A lot of research on shell structures has already been done. However, insight into the relation between the mechanical and geometrical properties of shells still remains incomplete. Block (2009) developed a method (Thrust Network Analysis) with which graphic statics is applied three-dimensionally for indeterminate free-form structures. The method is interesting, but very complicated and provides limited insight into the load-path of a structure. This thesis attempts to go beyond that: it gives a comprehensive understanding of the thrust surface geometry, which is guiding for an optimised shell structure.

Societal relevance: This thesis aims to provide more comprehensive knowledge on shell structure mechanics that makes it easier for designers to shape such shell structures. Ultimately, it provides designers with a tool that visualises the thrust surface, giving insight into the mechanical properties. The knowledge gained by this research is also applicable across other disciplines within structural mechanics. In *6.3*, a more elaborate reflection on the relevance and societal impact of this research is given.

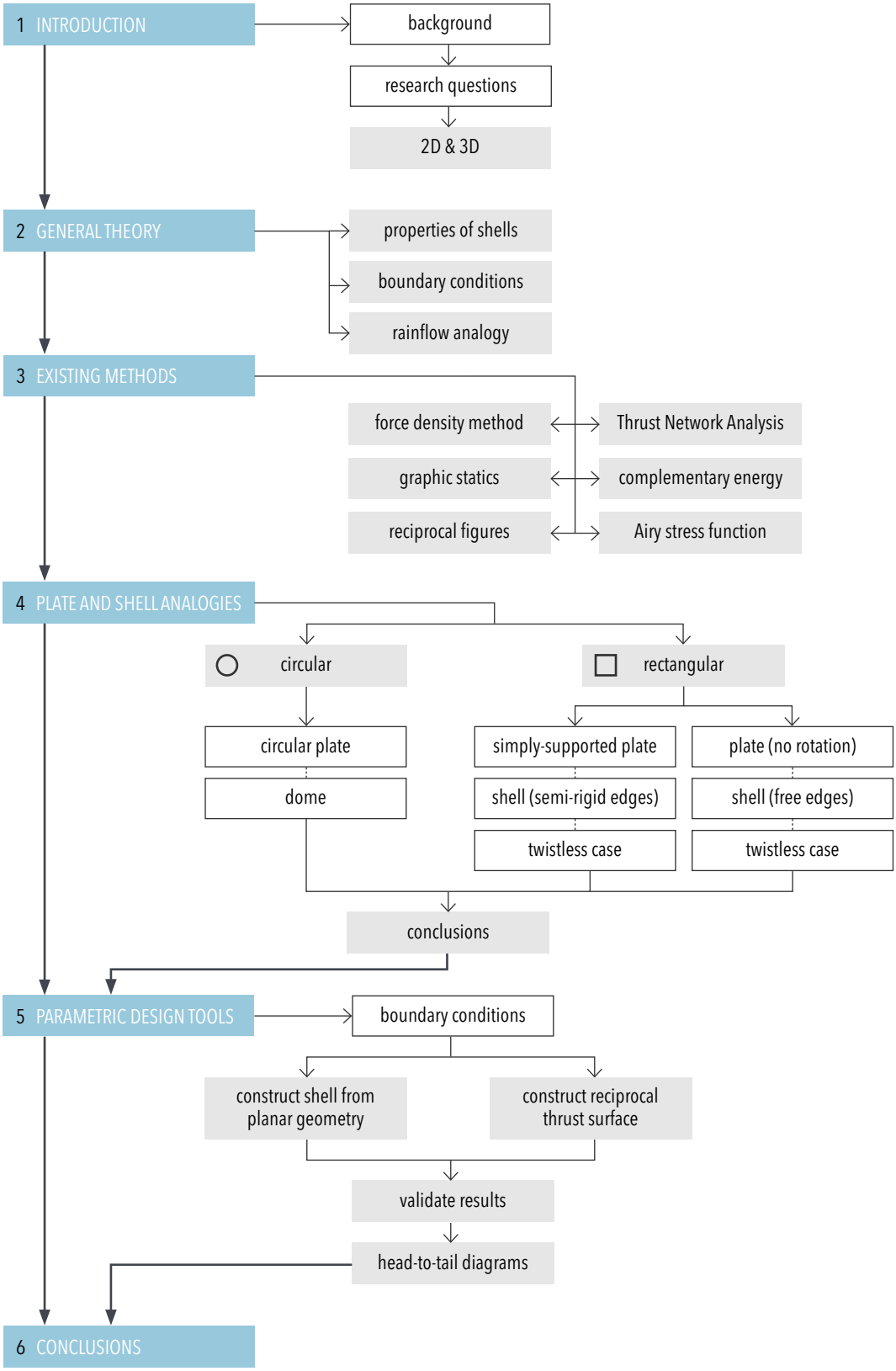

Figure 1.4: Structure research process

2. GENERAL THEORY

2 THEORETICAL FRAMEWORK

2.1 PROPERTIES OF SHELLS

A shell can be considered an isotropic plate, that has a very small ratio between the thickness and the span. We can define a shell by its middle plane, thickness and material properties. The difference between a plate and a shell is that the middle plane in plates is flat, and curved in shells. Therefore, shells can carry out-of-plane loads by in-plane membrane forces, which plates cannot. This is the major reason that shells are as strong as they are. The theory behind this behaviour is called the membrane theory (Blaauwendraad & Hoefakker, 2014).

2.1.1 GAUSSIAN CURVATURE OF A SURFACE

Consider the surface in Figure 2.1. At any point A on the surface, a plane tangential to the surface can be drawn. The normal to the surface at that point is the normal to that tangent plane. A plane through point A that contains the normal is the normal to the middle surface normal sections of the surface at A. Every curve has a local curvature k and a corresponding radius of curvature r. If the origin is at the positive side of the

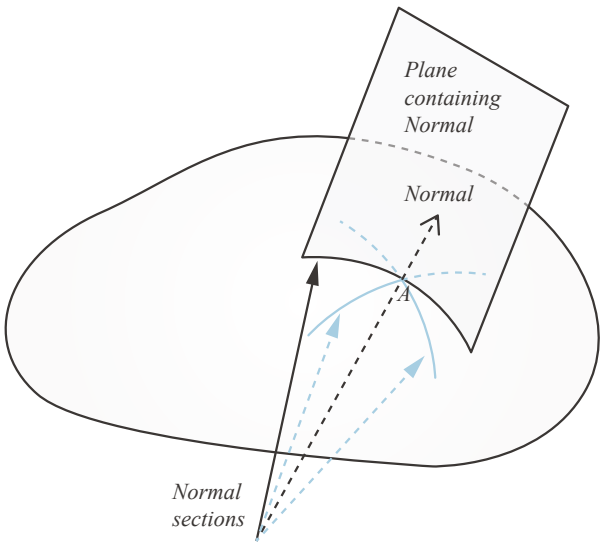

Figure 2.1: Intersection of a plane with a surface (retrieved from: Blaauwendraad & Hoefakker, 2014)

normal to the surface, then $r = k$. If it is at the negative side of the normal, then $r = -k$ (Blaauwendraad & Hoefakker, 2014).

At point A an infinite number of plane curves can be drawn. Out of these curves, one has a minimum curvature, which is the principal curvature κ_1, another has a maximum curvature, which is the principal curvature κ_2 of the surface at A. These curvatures are always perpendicular to each other. Using these curvature lines, it is possible to draw a UV-coordinate system onto any surface. By using the normal vectors to the surfaces as z-axes, a three-dimensional coordinate system UVW is made. Such a coordinate system is often used in 3D-modelling applications such as Rhinoceros.

The Gaussian curvature K is given by the product of the principal curvatures κ_1 and κ_2. With the principal curvatures, their corresponding principal radii can also be calculated [2.1]. The principal radii are the inverse of the principal curvatures. The Gaussian curvature can be zero, positive and negative. If the curvature is zero, the shell is considered to be monoclastic. If it is positive, the shell is considered synclastic. If the curvature is negative, the shell is considered anticlastic (Figure 2.2) (Blaauwendraad & Hoefakker, 2014).

$$K = \kappa_1 \kappa_2 = \frac{1}{R_1 R_2} \qquad [2.1]$$

$$R_1 = \frac{1}{\kappa_1} \quad and \quad R_2 = \frac{1}{\kappa_2} \qquad [2.2]$$

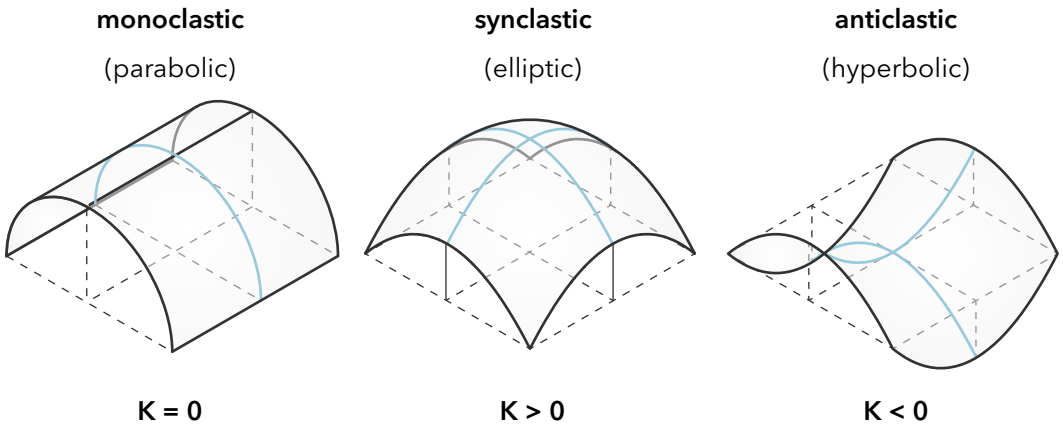

Figure 2.2: Types of Gaussian curvatures

All surfaces from Figure 2.2 are surfaces of translation. They can be generated by sliding one curve across another, having the same section across the entire curve.

2.1.2 DEVELOPABILITY OF A SURFACE

The developability of a surface is given by the ability to deform a planar surface without cutting or stretching. If this is not possible, then it is said to be undevelopable (Blaauwendraad & Hoefakker, 2014). Both cases are shown in Figure 2.3. Double-curved surfaces ($K < 0$ or $K > 0$) are undevelopable while single-curved surfaces ($K = 0$) are developable. The developability is a geometrical property of a surface, but is of structural significance. A developable surface for instance, is typically easier to fabricate, but is less strong. Less energy is needed to deform the surface than with that of an undevelopable surface.

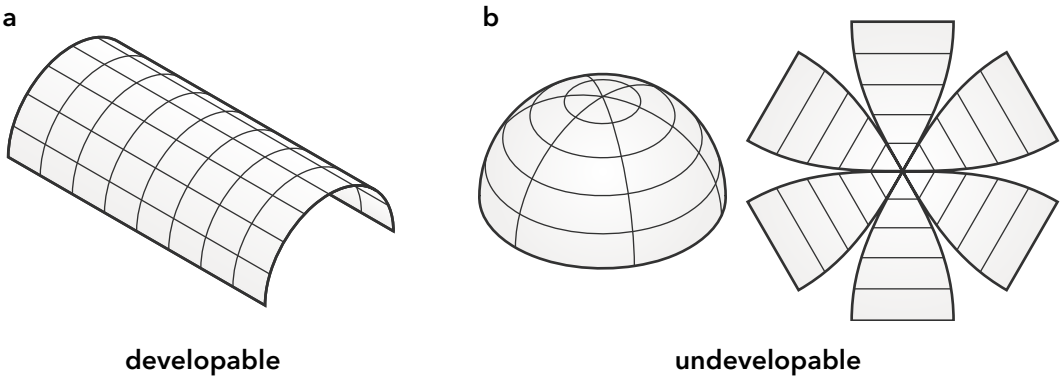

Figure 2.3: Examples of a surface that can be developed (a) and a surface that cannot be developed (b) (retrieved from: Blaauwendraad & Hoefakker, 2014)

2.1.3 DESCRIPTION OF SHELL STRUCTURES

The three conventional shell shapes are analytically explained below (Figure 2.4). Each of these surfaces is a surface of translation; they can be created by sliding one curve across another. The z-coordinate in each x-y coordinate is determined by the radius in that point, and follows a parabolic path.

Parabolic cylinder:

$$z = \frac{1}{2r} y^2 \qquad [2.3]$$

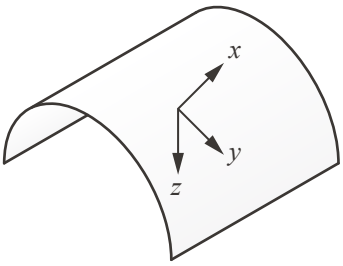

Elpar:

$$z = \frac{1}{2r_1} x^2 - \frac{1}{2r_2} y^2 \qquad [2.4]$$

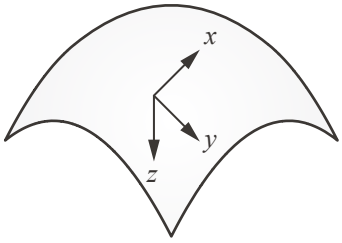

Hyppar:

$$z = \frac{1}{2r_1} x^2 - \frac{1}{2r_2} y^2 \qquad [2.5]$$

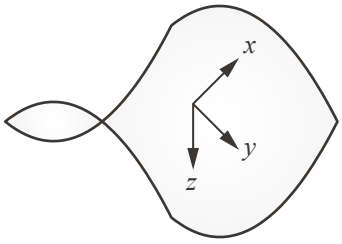

Figure 2.4: Analytical expressions for shallow shells

2.1.4 DIFFERENTIAL EQUATIONS FOR SHELLS

To provide a complete and clear explanation of the structural behaviour of shells, a short overview of forces acting on a shell element is given. Figure 2.5 shows a thin shell element as part of a larger shell structure. It is assumed to merely take up membrane forces, meaning that no bending, torsion, and transverse shear stresses occur (Blaauwendraad & Hoefakker, 2014). In the element, four types of vectors can be distinguished: displacements u, strains e, membrane forces s, and loads p. The four vectors are related to each other by three relations: the kinematic relation, the constitutive relation and the equilibrium relation (Figure 2.6). The relations can all be expressed in differential equations.

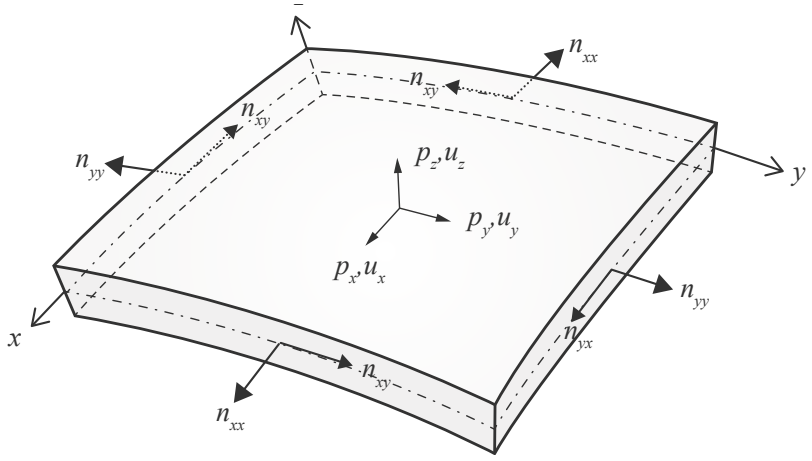

Figure 2.5: Definition of displacements, loading and membrane forces (retrieved from: Blaauwendraad & Hoefakker, 2014)

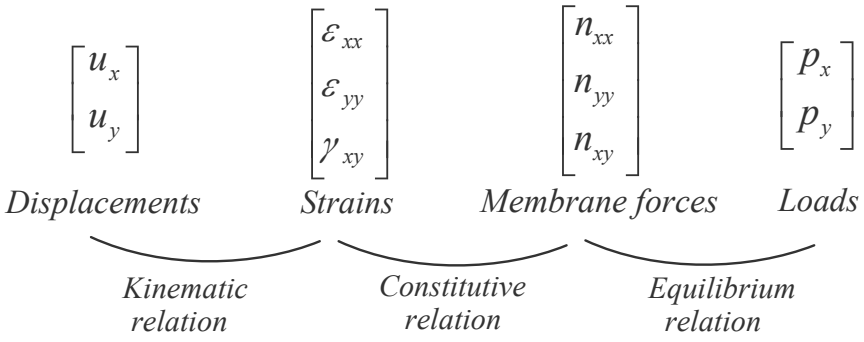

Figure 2.6: Scheme of relationships in membrane theory (retrieved from: Blaauwendraad & Hoefakker, 2014)

This thesis section does not go in-depth on all specific differential equations between vector families in an element. For now, only the nature of each relation will be elaborated, which will form a theoretical basis for following sections in this chapter.

Kinematic relation: Displacements u_x and u_y are in the direction of the principal curvatures k_1 and k_2, tangential to the middle surface. u_z is normal to the middle surface, in the direction of the local z-axis (see *2.1.1*) (Blaauwendraad & Hoefakker, 2014). The strain vector e as a result of displacements u_x, u_y and u_z is described by [2.6], showing that the strain in any direction is equal to the difference in displacement in that direction.

$$\varepsilon_{xx} = \frac{du_x}{dx} \qquad \varepsilon_{yy} = \frac{du_y}{dy} \qquad \gamma_{xy} = \frac{du_x}{dy} + \frac{du_y}{dx} \tag{2.6}$$

The strain can also be written as a product of the principal curvature k and the displacement u, completing the matrix of the kinematic relation [2.7].

$$\begin{bmatrix} \varepsilon_{xx} \\ \varepsilon_{yy} \\ \gamma_{xy} \end{bmatrix} = \begin{bmatrix} \frac{d}{dx} & 0 & -k_1 \\ 0 & \frac{d}{dy} & -k_2 \\ \frac{d}{dy} & \frac{d}{dx} & 0 \end{bmatrix} \begin{matrix} u_x \\ u_y \\ u_z \end{matrix} \tag{2.7}$$

Constitutive relation: The first constitutive relation was developed by Robert Hooke, and is known as Hooke's law. Following this principle, the assumption is made that the shell material behaves linearly-elastic. The relation is in this case between the stress n and strain (ε & γ), given by the matrix [2.8] (Blaauwendraad & Hoefakker, 2014).

$$\begin{matrix} n_{xx} \\ n_{yy} \\ n_{xy} \end{matrix} = \frac{Et}{1-v^2} \begin{bmatrix} 1 & v & 0 \\ v & 1 & 0 \\ 0 & 0 & \frac{1-v}{2} \end{bmatrix} \begin{matrix} \varepsilon_{xx} \\ \varepsilon_{yy} \\ \gamma_{xy} \end{matrix} \tag{2.8}$$

Equilibrium relation: The scheme in Figure 2.6 shows that there are three unknowns, and therefore three equations must be derived. The equilibrium components p_x and p_y are easily composed, since they correspond with those of a flat plate loaded in-plane. The equilibrium component for p_z requires further investigation of the curvature of the middle surface (Blaauwendraad & Hoefakker, 2014). It was explained in *2.1.1* that the coordinate system of a surface is placed relative to its principal curvatures k_1 and k_2 which in their turn are negative or positive based on their location to the normal. A load p_z tangential to the surface results in membrane forces n_{xx} and n_{yy} and in a difference in angle (Figure 2.7). From the relation between the principal curvatures k and radii R [2.2], the last equilibrium equation can be derived [2.9].

$$\frac{dn_{xx}}{dx} + \frac{dn_{yx}}{dy} + p_x = 0$$

$$\frac{dn_{yy}}{dy} + \frac{dn_{xy}}{dx} + p_y = 0 \qquad [2.9]$$

$$k_1 n_{xx} + k_2 n_{yy} + p_z = 0$$

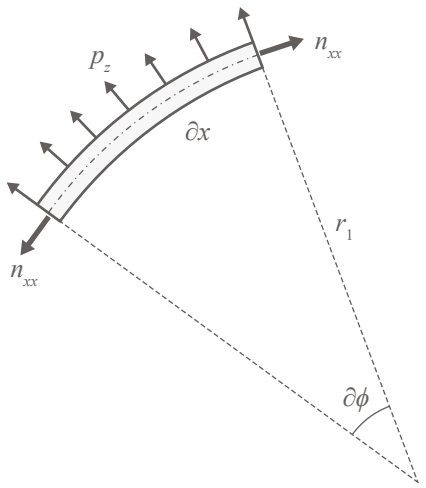

Figure 2.7: Membrane forces n_{xx} and normal load p (retrieved from: Blaauwendraad & Hoefakker, 2014)

2.2 BOUNDARY CONDITIONS

For this thesis, it is essential that the boundary conditions of every analysed element are determined carefully. For instance, some boundary conditions must be applied to the S-surface, and others to the B-surface as described in *3.2* later in this thesis. Therefore, in this chapter a number of boundary conditions are established and distinguished in order to achieve uniformity throughout all analysis cases. Load cases and support conditions and material properties are assessed respectively.

2.2.1 LOAD CASES

Throughout this thesis, in three-dimensional cases a projected load as opposed to a distributed load is assumed. The projected load resembles the dead load of an element, whereas the distributed load can be imagined a snow load. Establishing this distinction is essential, as it has consequences on the calculation of statical problems.

The importance of making the distinction between different load cases clear also became apparent in the research of Riemens (2015). Riemens got inaccurate results in the assessment of shell structures using his parametric tool. He concluded that his tool proved to be accurate for shallow shells, but became increasingly inaccurate with an

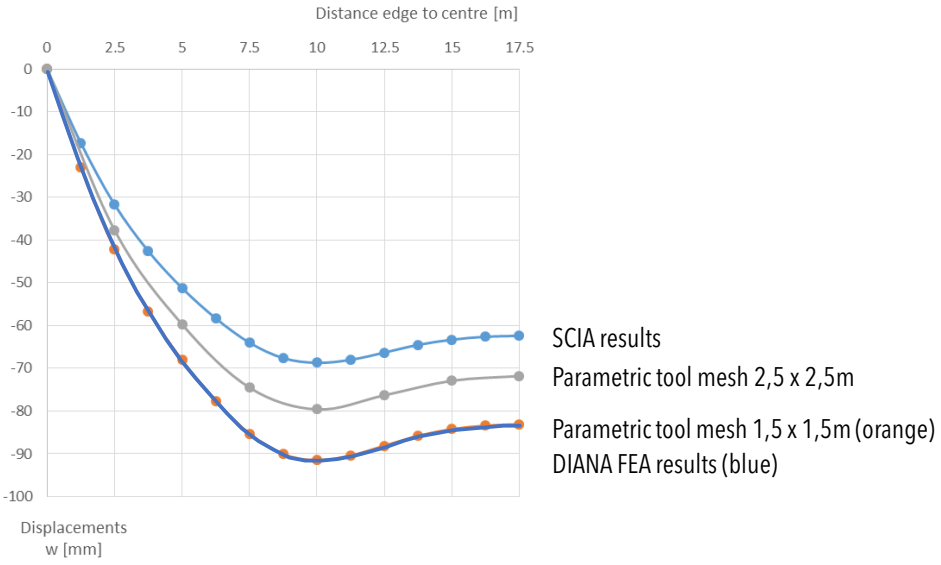

Figure 2.8: Results displacement parametric tool Riemens compared to DIANA FEA with a projected load as opposed to a distributed load

increasing R. The calculation of the '*Hallenbad shell*', has been recomputed in DIANA FEA, but now with a projected load instead of a distributed load. The results for the displacement w_z are compared in Figure 2.8. It can be concluded that the results are highly accurate for the case of a projected load. To avoid confusion, the difference between a projected and a distributed load is further explained in this section.

Consider a dome like in Figure 2.9. The dome is subjected to an evenly distributed snowload q_{snow}. The intensity of the load is equal to the horizontal span times q. If we consider snowload q as actual snowflakes falling onto the structure, we can imagine it to be projected. The width of the snowload is then distributed across the entire length of the arc, resulting in a decreased intensity per unit of length. When a dead load is considered, it is already projected, so the value per unit of length is known. The distinction is visualised in Figure 2.10.

In order to calculate the load perpendicular to the surface $q_{\perp}$ for the structure subjected to the snowload, we consider an angle α between the horizontal axis and the tangent in a point. Now q_{snow} over the roof area is governed by $q_{snow} = S \cdot \cos\alpha$. To determine the total load perpendicular to the roof surface, we must once again use α. This gives us [2.10]. When we calculate the load perpendicular to the roof surface as a result of the dead load, we use [2.11]. Since the difference between the projected load and the distributed load is determined by α, for shallow shells the difference is often negligible.

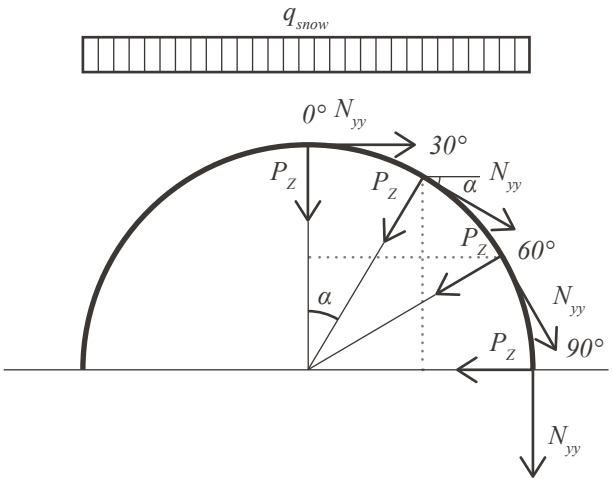

Figure 2.9: Section of a dome subjected to a snow load q

load due to snow:

(distributed)

load due to own weight:

(projected)

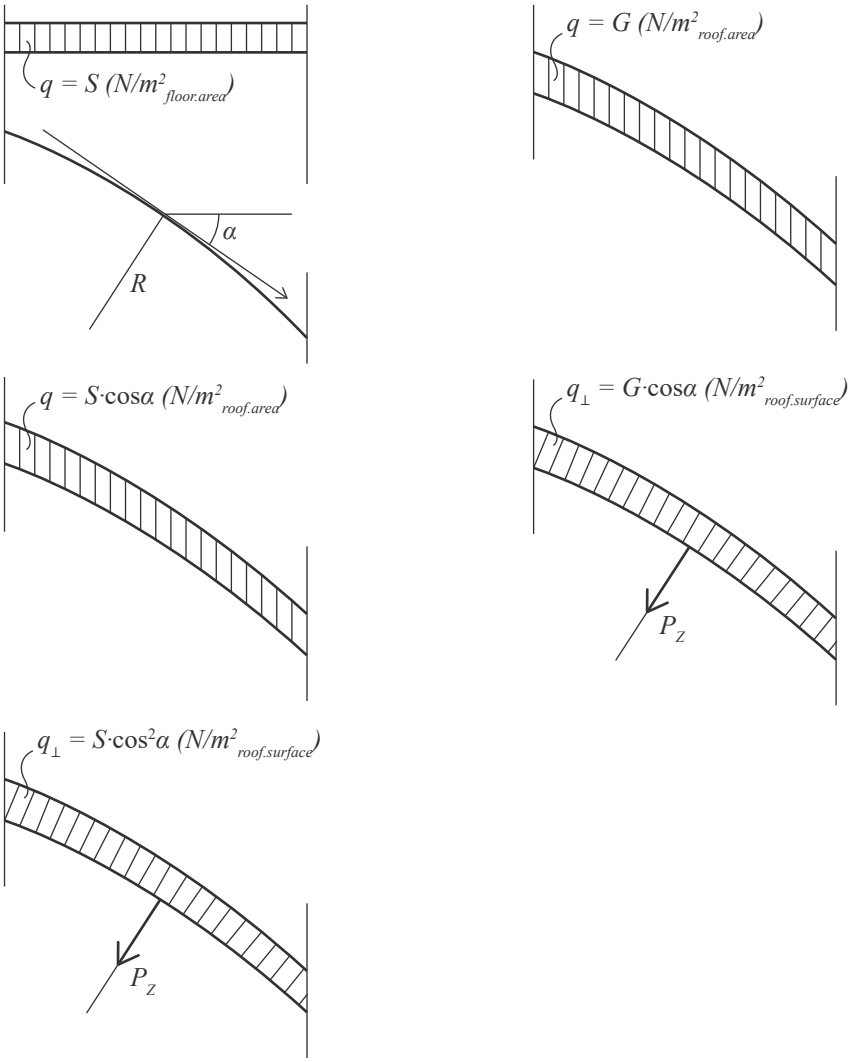

Figure 2.10: Calculation load perpendicular to surface (distributed load and projected load)

$$q_{\perp snow.load} = P_{zSn} = S \cdot \cos^2 \alpha \qquad [2.10]$$

$$q_{\perp own.weight} = P_{zEG} = G \cdot \cos \alpha \qquad [2.11]$$

2.2.2 SUPPORT CASES

It is important to distinguish the possible support cases. Later in this thesis, these will be used to show the influence on the relationship between a shell and its projection. The following support conditions can be distinguished (Table 2.1). Here n is the direction normal to the corresponding edge. All edge conditions are visualised in Figure 2.11. The symmetry edge can be considered an edge along which the loads are mirrored, allowing for displacements w, but ensuring a rotation $\varphi = 0$. We can compare it with a continuous floor on columns, for instance.

Support type	Displacement	Reaction force	Angle/curvature
Free edge	$w \neq 0$	$f = 0$	$\frac{\partial^2 w}{\partial n^2}$
Clamped edge	$w = 0$	$f \neq 0$	$\frac{\partial w}{\partial n}$
Semi-rigid edge	$w = 0$	$f \neq 0$	$\frac{\partial^2 w}{\partial n^2}$
Symmetry edge	$w \neq 0$	$f = 0$	$\frac{\partial w}{\partial n}$

Table 2.1: Boundary conditions supports parametric tool

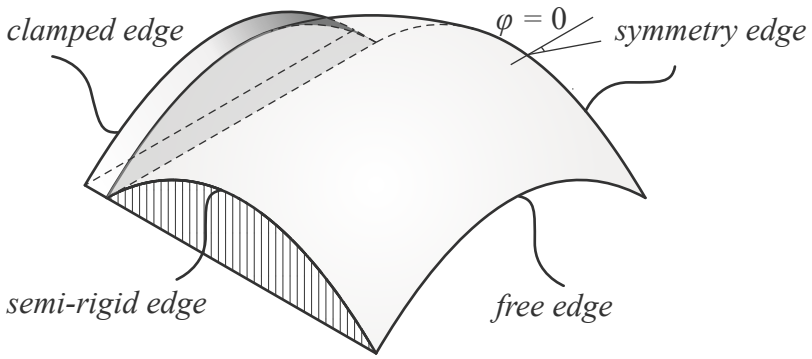

Figure 2.11: Different edge conditions

2.3 RAINFLOW ANALOGY

W.J. Beranek introduced the rainflow analogy, which illustrates the direction of the load trajectories in an element (Figure 2.12). He considered the sum of bending moments m_{xx} and m_{yy} as 'hill', and the load as a rain shower. The trajectories v_n are comparable to the streamlines of flowing water; the water always flows parallel to the trajectories (Blaauwendraad, 2010). The rainflow analogy can therefore be used to determine out-of-plane structural behaviour.

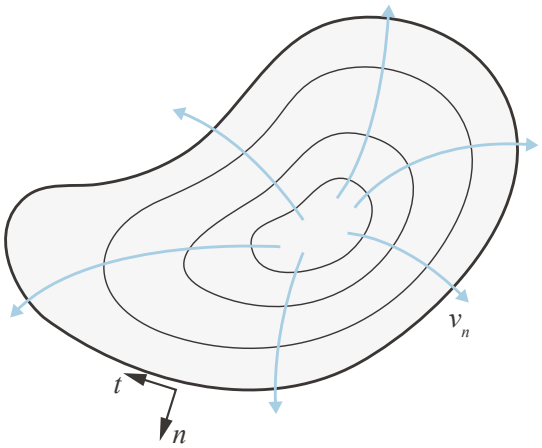

Figure 2.12: Rainflow analogy. Water flows in the direction of the deepest slope (retrieved from: Blaauwendraad, 2010)

The principal shear forces can be determined using the sum of bending moments $\bar{M}$, which is calculated through the following equation [2.12]:

$$\bar{M} = \frac{m_{xx} + m_{yy}}{1 + v} = -D \cdot \Delta w \qquad [2.12]$$

Poisson's ratio v is taken into account in this equation. Further into this thesis, primarily an isotropic material is assumed, giving that $v = 0$. This gives a sum of bending moments $\bar{M} = m_{xx} + m_{yy}$. Now, to calculate the shear forces v_x and v_y, one takes the second derivative of the sum of bending moments with respect to the x- and y-axes [2.13]:

$$v_x = \frac{d}{dx} \cdot \bar{M} \quad \textit{and} \quad v_y = \frac{d}{dy} \cdot \bar{M} \qquad [2.13]$$

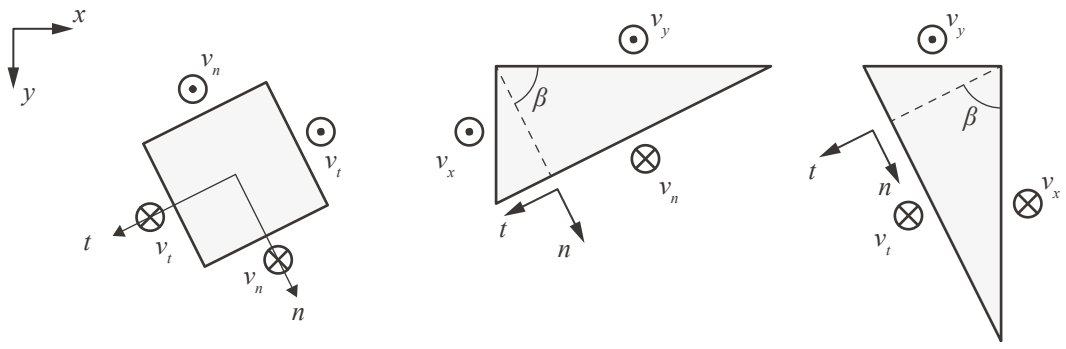

Figure 2.13: Equilibrium of plate parts (retrieved from: Blaauwendraad, 2010)

In Figure 2.13, two triangular elements are illustrated with the shear forces acting on their edges. Two orthogonal sets of axes are shown; the x-y set and the n-t set. The angle between two sets is given by β. The shear forces acting on the element on the left are drawn as arrows. The top of the arrow is indicated by a dot, and the back by a cross. An arrow coming towards the reader indicates shear forces on faces with a negative normal vector; an arrow moving away indicates shear forces on faces with a positive normal vector. The shear force in any arbitrary direction (v_n & v_t) under angle α in respect to the x- and y-axes can now be calculated (Borgart & Oosterhuis, 2010). For this one must know the shear force in x-direction v_x and in y-direction v_y, resulting in the following formulas [2.14]:

$$v_n = v_x \cos\beta + v_y \sin\beta \qquad [2.14]$$

$$v_t = v_x \sin\beta + v_y \cos\beta \qquad [2.15]$$

To determine the direction and maximum value of v_n, it is required that $dv_n/d\beta = 0$. Using the formula for the shear force v_t from [2.15], it can be established that $v_t = -v_x \sin\beta + v_y \cos\beta = 0$. From equations [2.14] and [2.15] it can also be concluded that v_t is zero when v_n is maximal and vice versa. The direction angle of the trajectory is then calculated by [2.16] (Blaauwendraad, 2010).

$$\tan\beta_0 = \frac{v_y}{v_x} \qquad [2.16]$$

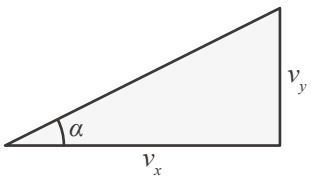

Figure 2.14: Relation between v_x and v_y

The relation between v_x and v_y is displayed in Figure 2.14. Now, using Pythagoras' theorem, the maximal shear force $v_{n,\max}$ can be determined [2.17].

$$v_{n,\max} = \sqrt{{v_x}^2 + {v_y}^2} \qquad where \qquad v_t = 0 \qquad [2.17]$$

The gradient of the contour lines of the $\bar{M}$-hill surface is zero, and the steepest slope is always perpendicular to these contour lines. Therefore the contour lines are determined by the minimal shear forces and the rainflow by the maximal shear forces. The principal shear force can then be written as [2.18]:

$$v_n = \frac{d}{dn}(\cdot\bar{M}) \qquad [2.18]$$

2.3.1 COMPUTATIONAL APPLICATION

With recent computational possibilities, the rainflow analogy can now be projected onto the $\bar{M}$-hill, giving clear insight into how loads are directed to the supports through shear forces. Oosterhuis (2010) developed a parametric tool with which an $\bar{M}$-hill and its reciprocal rainflow image can be generated of a given load case on a structure. This tool will be applied throughout this thesis to obtain insight in the force flow of assessed structures.

3. EXISTING METHODS

3 EXISTING METHODS

3.1 GRAPHIC STATICS

3.1.1 GRAPHIC STATICS

Graphic statics is a method of graphically describing forces acting on a static structure. In this method forces are plotted as vectors, each with its own direction and magnitude. The external forces on each structure are plotted to a scale of length to forces on a load line. Working from the load line, the forces in the members of the structure are determined by scaling the lengths of lines constructed parallel to the members (Greenwold & Allen, 2001). The result is a force diagram as displayed in Figure 3.1, called the force polygon. So long as all forces combined form a closed loop, the structure is in equilibrium.

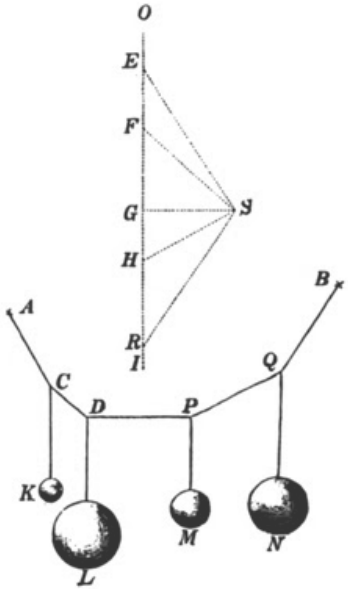

Figure 3.1: Graphic statics as described by Pierre Varignon in his book Nouvelle Mecanique Ou Statique from 1725 (retrieved from: http://eat-a-bug.blogspot.com)

The procedure is as follows:

A uniformly distributed load is reduced to a series of point loads, distributed along the x-axis (Figure 3.2). The forces are drawn to scale as vectors. The forces are then added together using the '*head-to-tail*' method, in which the head of the first vector is

connected to the tail of the second, and so on. The result is a polyline, which is the sum of all individual forces and therefore equal to the initial distributed load.

Next, the polar coordinate is drawn on an arbitrary location next to the force polyline (Figure 3.3). Lines are drawn between the heads and tails and the polar coordinate, resulting in a series of triangles. These triangles are the force polygons describing the force equilibrium in the node of the structure on that specific location (Liem, 2011).

Since adjacent polygons share at least one member, their vectors are of the same length and direction. Therefore, the axial forces in that member are also equal. Figure 3.2 and Figure 3.3 show a direct graphical relation between the force network and its possible solutions (Block, 2009). An infinite number of solutions for the thrust line is possible, but the 'optimal' solution cannot be determined this way.

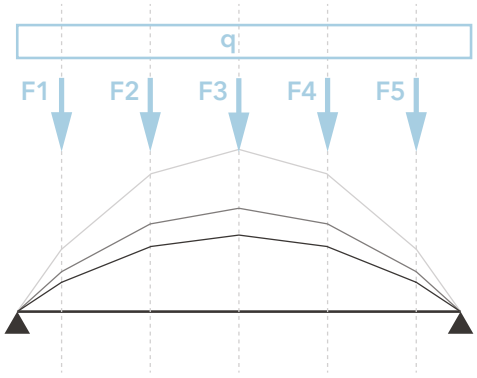

Figure 3.2: Distributed load is reduced to parallel pointloads

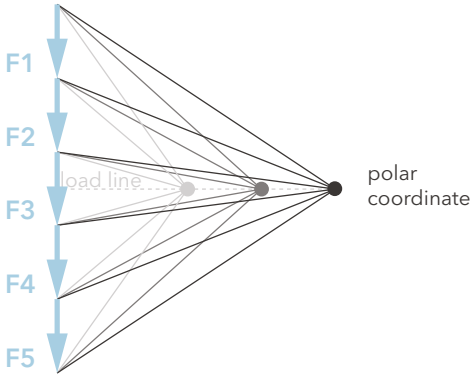

Figure 3.3: Pointloads are connected to polar coordinate

3.1.2 THRUST LINE ANALYSIS

Equilibrium in a masonry arch can be visualised using a 'line of thrust' (Block, DeJong, & Ochsendorf, 2006). The line of thrust is a conceptual line that represents the path of the compressive forces through a funicular structure. For a purely funicular structure to be in equilibrium, the line of thrust must lie entirely within the section of the material. If this is not the case, the structure will collapse (unless tensile reinforcement is present).

The method of Thrust Line Analysis (Block et al., 2006) builds upon this principle. Consider a random arch as the one in Figure 3.4a. The arch consists of masonry blocks stacked on top of each other, forming a structure solely in compression. The structure is static, so all blocks are in equilibrium. The force polygon as described in *3.1* can be applied to each of the blocks. Three forces act on the highlighted block in Figure 3.4a (Figure 3.4b), resulting in the force polygon in Figure 3.4d.

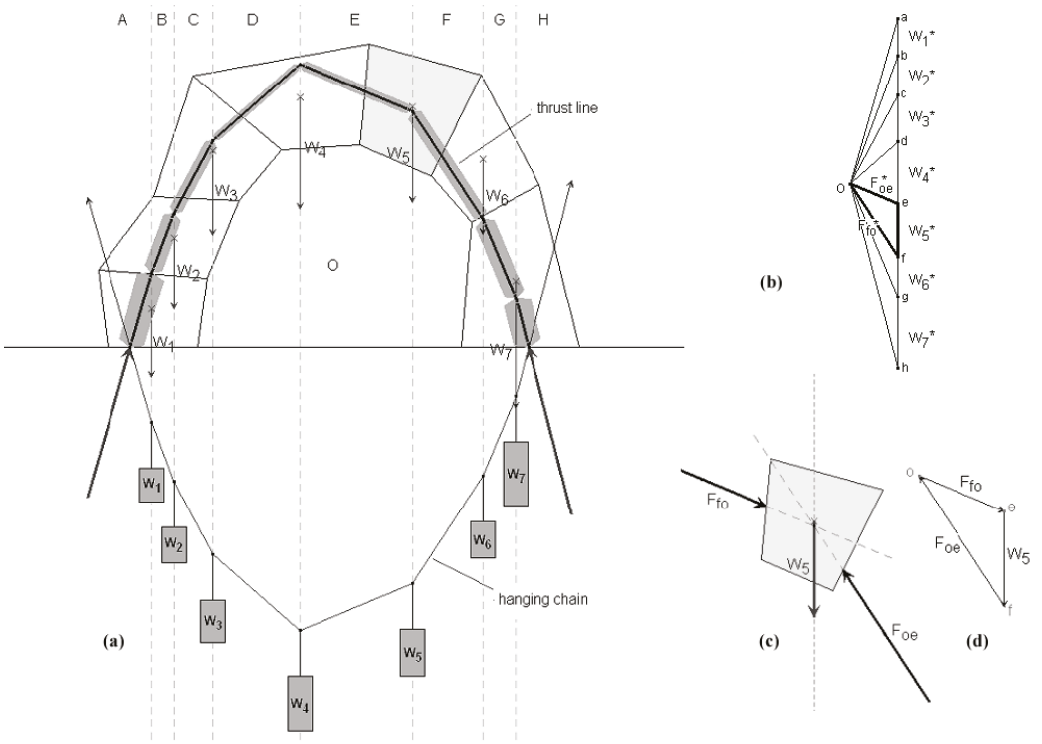

Figure 3.4: For a random arched structure, (a) a possible thrust line and its equivalent hanging chain are constructed using graphic statics; (b) the force equilibrium of the system is represented in the funicular polygon; (c) the equilibrium of one of the *voussoirs*, and, (d) the vectors representing the forces in and on the block (retrieved from: Block et al., 2006)

The magnitude of each force depends on the weight of its corresponding block. Thus, the height of the line of thrust is determined by the weight of the structure. Consequently, each funicular arch structure has a minimum and maximum line of thrust, corresponding to a minimum and maximum weight of the structure. Figure 3.5 shows an example of this. The line of thrust can be considered an inverted catenary (van Dijk, 2014).

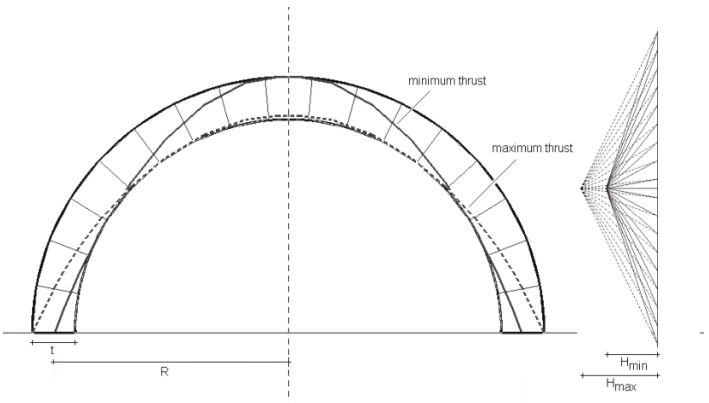

Figure 3.5: Arch with minimum and maximum line of thrust (retrieved from: Block et al., 2006)

3.1.3 THRUST NETWORK ANALYSIS

Until now, graphic statics, including arch analysis, was limited to two-dimensional systems. To allow for graphical description of three-dimensional systems, Block & Ochsendorf (2007) proposed the '*Thrust Network Analysis*' method. The method was primarily intended to assess equilibrium in masonry vaults, but also proved to be useful as a design tool for funicular structures.

The method is analogous to graphic statics in the sense that it utilises a graphical representation of forces in a system by applying force polygons. Key elements in the process are force networks, interactive reciprocal diagrams, the use of envelopes defining the solution space and linear optimisation. The latter makes it a responsive and insightful method.

Thrust Network Analysis works as follows (Block & Ochsendorf, 2007):

a. First, a solution envelope is defined. The envelope supplies boundaries within which the solution must lie. The boundaries are defined by a minimum and maximum value (Figure 3.6). When exploring the thrust network of an existing masonry structure, these will be the border planes of the structure (also see *3.1.2*). When designing a funicular structure, these limits can be the design envelope.

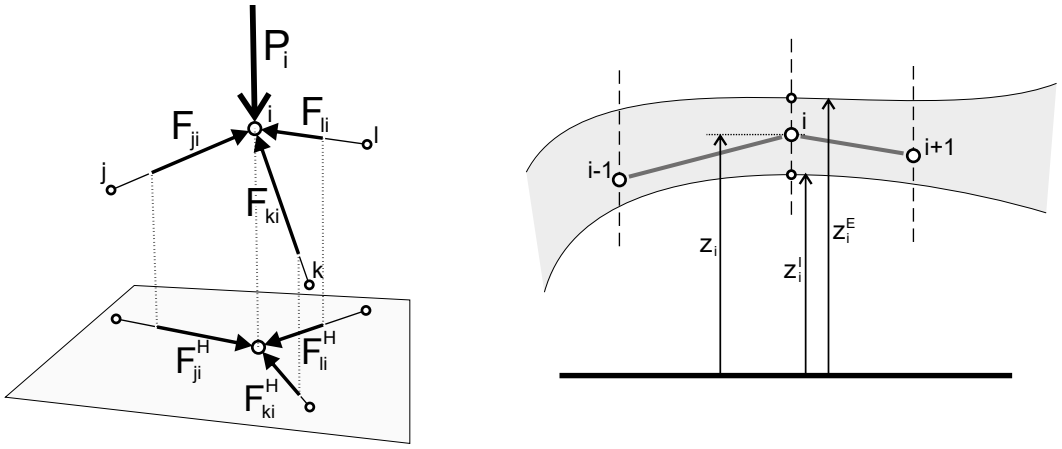

Figure 3.6: The constraints come from (a) static equilibrium in every node under the applied loading and (b) the given boundaries, resulting in nodal height constraints (retrieved from: Block, 2009)

b. Subsequently, a possible force pattern topology is constructed, typically generated automatically by a script. This is called the primal grid Γ (Figure 3.7). It is a series of loaded nodes, connected by branches that represent possible load paths throughout the structure.
c. Weights are assigned to each node by distributing the dead load of a structure across these nodes. As needed, additional weights can be applied.
d. A dual grid Γ^* is generated from the primal grid Γ. The dual grid is the reciprocal figure of the primal grid, meaning that forces acting on a node are transformed into force polygons. The applied loads disappear after this conversion, meaning that the scale of forces becomes unknown. This unknown scale ζ determines the height of the structure, and depends on the horizontal forces subjected to it.
e. In Figure 3.7, all nodes are three-valent, meaning that the structure is statically determinate; one reciprocal dual grid Γ^* is possible for a given primal grid Γ. In case of a network with a valency higher than three, the structure becomes statically indeterminate. Now the dual grid Γ is determined by the force distribution, which can be adjusted manually (Figure 3.9).
f. Using the geometry of the primal grid Γ and the dual grid Γ^*, the loads on the nodes and the boundary conditions, the problem can be solved through one-step linear optimisation.

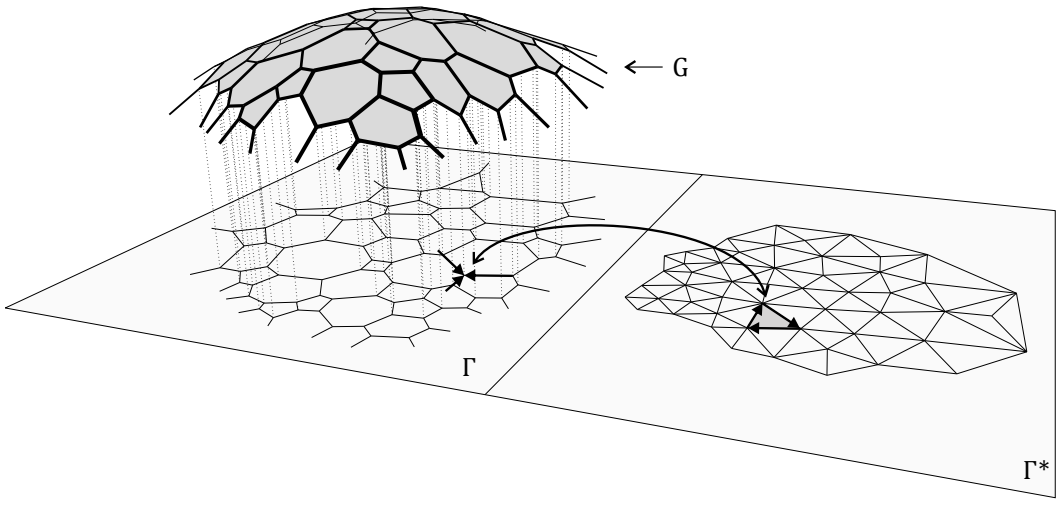

Figure 3.7: Relationship between compression shell (G), its planar projection (primal grid Γ) and the reciprocal diagram (dual grid Γ^*) to determine equilibrium (retrieved from: Block & Ochsendorf, 2007)

The results should all lie within the given boundaries, i.e. (Block & Ochsendorf, 2007):

$$z_i^{\,I} \leq z_i \leq z_i^{\,E} \qquad [3.1]$$

To obtain all possibilities in that range, the minimum and maximum r ($= 1/\zeta$) should be found. The establishment of the scale factor ζ provides the magnitude of the horizontal forces. An analogy is present between the scale factor ζ in the Thrust Network Analysis and the repositioning of the polar coordinate in graphic statics (Liem, 2011).

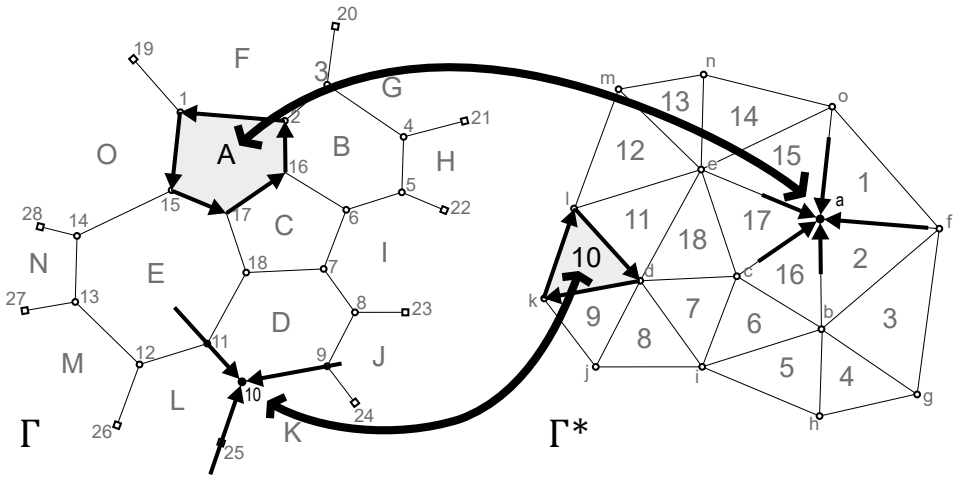

Figure 3.8: Reciprocal relation between the primal grid Γ and the dual grid Γ^* (retrieved from: Block, 2009)

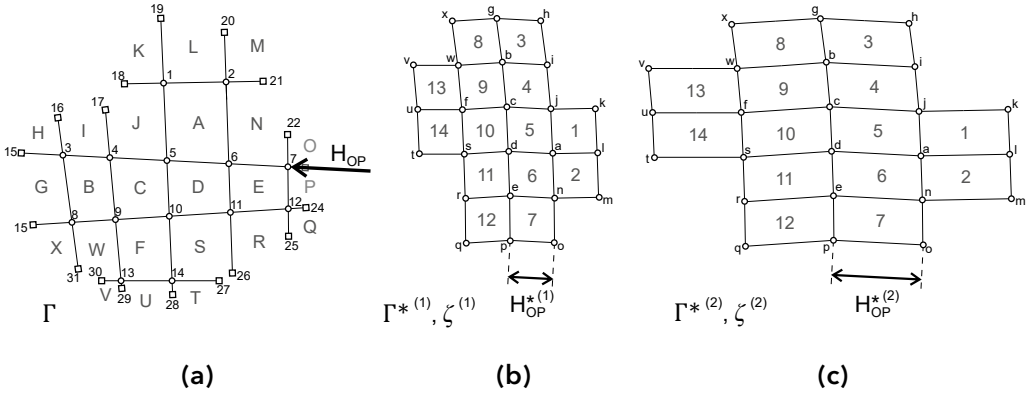

Figure 3.9: For an indeterminate primal grid (a), multiple dual grids corresponding to different internal distribution of the (horizontal) forces are possible (b-c) (retrieved from: Block, 2009)

3.2 STATIC-GEOMETRIC ANALOGY

An analogy exists between the *statical* equilibrium equations and the *geometric* compatibility equations in the theory of thin shell structures (Calladine, 1977). The correspondence is facilitated by two innovations; (1) the conceptual split of a shell structure into a stretching (S) and bending (B) surface, and (2) the use of change of Gaussian curvature *g* as a prime variable.

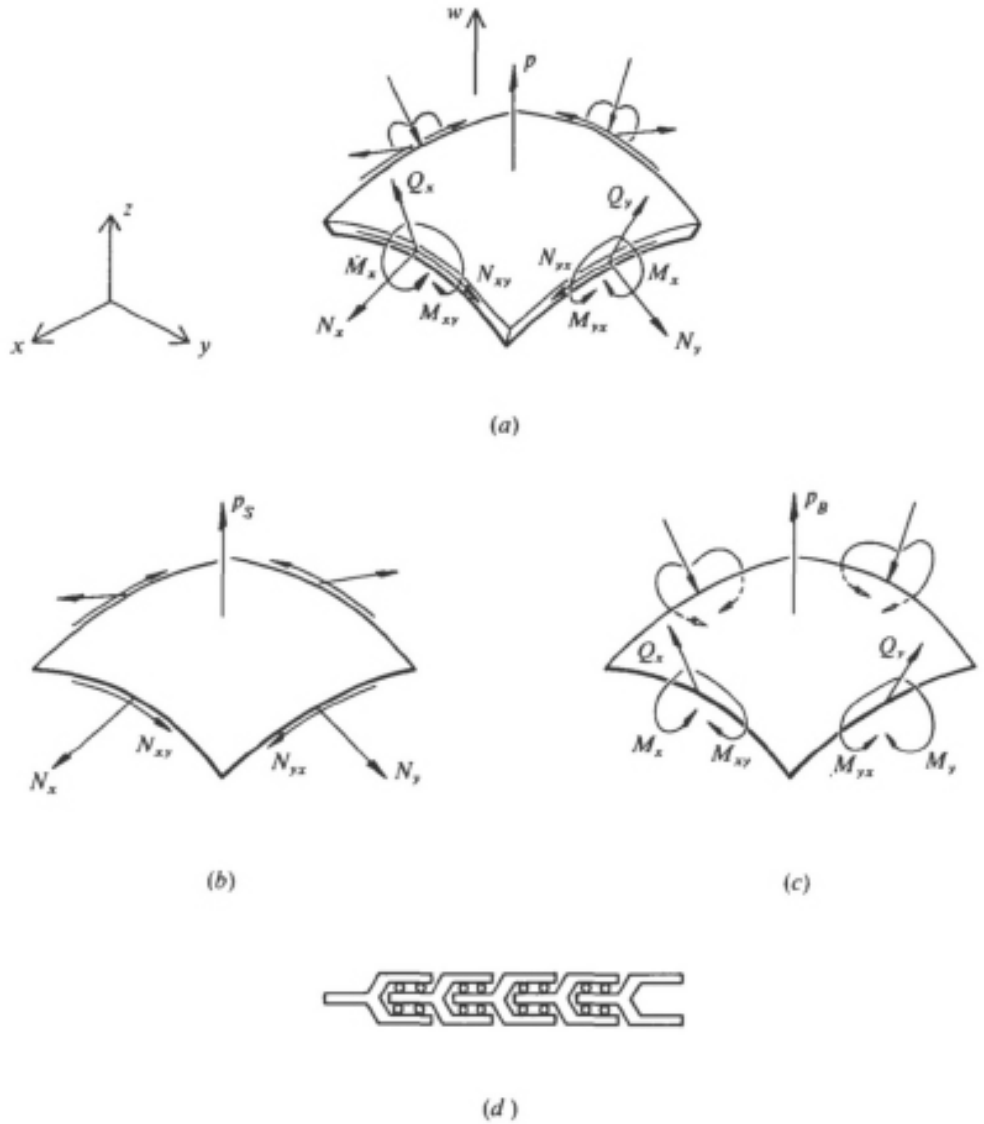

Figure 3.10: An element of a shallow shell showing positive sense of pressure loading, all stress resultants and displacements (a), the S-surface (b), the B-surface (c), a straight beam illustrating the physical characteristics of the B-surface (d) (retrieved from: Calladine, 1977)

Figure 3.10a shows a section of a thin shell, with its corresponding normal surface traction stress resultants N_x, N_y, N_{xy}, out-of-plane shear stress resultants Q_x, Q_y and bending and twisting stress resultants M_x, N_x, N_{xy}, similar to that in *2.1.4*. In Figure 3.10b and c, these have been divided into two groups: N (1), and Q and M (2).

The first group corresponds with the S-surface, that carries forces in-plane only, but is incapable of absorbing bending moments or shear forces. A surface like this is comparable to a thin sheet or a string, that can only carry tensile loads. The second group corresponds with the B-surface; it is incapable of carrying tensile loads, but can sustain bending moments and shear forces. Real examples rarely exist, but an imagination is visualised in Figure 3.10d. Its roller supports have the ability to transfer bending moments and shear forces, but no normal forces (Calladine, 1977).

To express the mutual reaction between the parts, a force variable p and a displacement variable g are introduced. These describe the duality between the surfaces; the sum of the forces acting on the S- and B-surfaces results in equilibrium, resulting in [3.2]. Also, it is assumed that both surfaces are always equal to one another. Accordingly, the values of g_s and g_b coincide, resulting in [3.3]:

$$p = p_s + p_b \qquad [3.2]$$

$$g_S = g_B \qquad [3.3]$$

With the knowledge of [3.2] and [3.3], the static-geometric analogy can be constructed. The following dualities are hereby established, in which ϕ is the Airy stress function, ω is the normal component, ε is the normal strain and γ is the shear strain:

$$\begin{array}{lll} N_x \leftrightarrow \kappa_y & \varepsilon_x \leftrightarrow M_y & \phi \leftrightarrow -\omega \\ N_y \leftrightarrow \kappa_x & \varepsilon y \leftrightarrow M_x & g_S \leftrightarrow p_B \\ N_{xy} \leftrightarrow \kappa_{xy} & \gamma_{xy} \leftrightarrow 2M_y & p_S \leftrightarrow g_B \end{array} \qquad [3.4]$$

From this, the equations for the S- and B-surface are constructed (Figure 3.11).

Equations S1 and S2 are the equilibrium equations for an element of the S-surface (Calladine, 1977). S3 is the stress-function definition, S4 is the single compatibility equation. S5 is the isotropic version of Hooke's law of elasticity for the S-surface.

A student of Calladine, Pavlovic (1984) constructed a scheme based on this theory to calculate a shell element. It is based on an iterative process of calculating p_B with an arbitrary value of p_S. If $p_s + p_B$ equals p, the correct solution is found. Naturally, this means that the relationship between p_S and p_B is vital for the calculations. Nowadays, a calculation process like this can easily be conducted by means of computation.

$$\frac{N_x}{R_1}+\frac{N_y}{R_2}=p_S \qquad \text{(S 1)}$$

$$\left.\begin{aligned}\frac{\partial N_x}{\partial x}+\frac{\partial N_{xy}}{\partial y}&=0\\ \frac{\partial N_y}{\partial y}+\frac{\partial N_{xy}}{\partial x}&=0\end{aligned}\right\} \qquad \text{(S 2)}$$

$$\left.\begin{aligned}N_y=\frac{\partial^2\phi}{\partial x^2},\quad N_{xy}&=-\frac{\partial^2\phi}{\partial x\,\partial y},\\ N_x&=\frac{\partial^2\phi}{\partial y^2}\end{aligned}\right\} \qquad \text{(S 3)}$$

$$\frac{\partial^2\epsilon_y}{\partial x^2}-\frac{\partial^2\gamma_{xy}}{\partial x\,\partial y}+\frac{\partial^2\epsilon_x}{\partial y^2}=-g_S \qquad \text{(S 4)}$$

$$\left.\begin{aligned}\epsilon_x&=(N_x-\nu N_y)/Et\\ \epsilon_y&=(N_y-\nu N_x)/Et\\ \gamma_{xy}&=2(1+\nu)\,N_{xy}/Et\end{aligned}\right\} \qquad \text{(S 5)}$$

$$\frac{\kappa_y}{R_1}+\frac{\kappa_x}{R_2}=g_B \qquad \text{(B 1)}$$

$$\left.\begin{aligned}\frac{\partial \kappa_y}{\partial x}-\frac{\partial \kappa_{xy}}{\partial y}&=0\\ \frac{\partial \kappa_x}{\partial y}-\frac{\partial \kappa_{xy}}{\partial y}&=0\end{aligned}\right\} \qquad \text{(B 2)}$$

$$\left.\begin{aligned}\kappa_x=-\frac{\partial^2 w}{\partial x^2},\quad \kappa_{xy}&=-\frac{\partial^2 w}{\partial x\,\partial y},\\ \kappa_y&=-\frac{\partial^2 w}{\partial y^2}\end{aligned}\right\} \qquad \text{(B 3)}$$

$$\frac{\partial^2 M_x}{\partial x^2}+\frac{2\partial^2 M_{xy}}{\partial x\,\partial y}+\frac{\partial^2 M_y}{\partial y^2}=-p_B \qquad \text{(B 4)}$$

$$\left.\begin{aligned}M_y&=D(\kappa_y+\nu\kappa_x)\\ M_x&=D(\kappa_x+\nu\kappa_y)\\ M_{xy}&=D(1-\nu)\kappa_{xy}\end{aligned}\right\} \qquad \text{(B 5)}$$

Figure 3.11: Equations S-surface (left) and B-surface (right) in the static-geometric analogy in a shell surface (retrieved from: Calladine, 1977)

3.3 COMPLEMENTARY ENERGY

Statically determinate structures can be solved using direct methods, which work via a linear approach. For more complicated, indeterminate structures, however, indirect methods must be used. The Finite Element Method (FEM) is such a method, and so is the method of complementary energy. In this section, an explanation is given of complementary energy and it is shown how it can be applied to calculate indeterminate structures. A division is made between normal forces and bending moments.

Consider a cube of 1 x 1 x 1, loaded uniaxially by a stress σ. This load causes the material to deform by an amount ε. Accordingly, when a load σ is present, $\delta\sigma$ causes the strain to increase by $\delta\varepsilon$ (Figure 3.12a). Load σ performs an amount of work (energy) equal to $\sigma \cdot \delta\varepsilon$. The total amount of work, also called the deformation energy per unit of volume E'_s, equals (Blaauwendraad, 2002):

$$E'c = \int_0^{\varepsilon} \sigma \delta\varepsilon \qquad with\ \sigma = \sigma(\varepsilon) \qquad [3.5]$$

Deformation energy is considered potential energy, which is accumulated in the material. The deformation energy E'_s is described by the area under the curve (Figure 3.12b). The remaining area above the curve describes the complementary energy E'_c (Figure 3.12c). In this example, an elastic material is assumed, resulting in a curved slope. The shape of the curve therefore depends on the material properties.

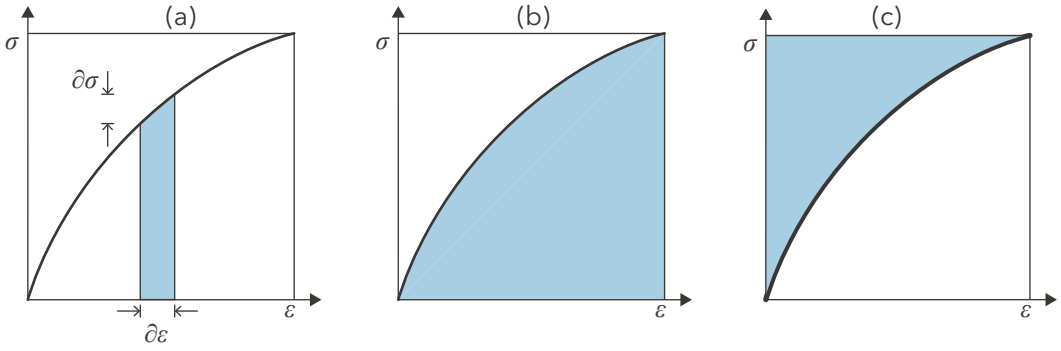

Figure 3.12: Relationship $\partial\sigma$ and $\partial\varepsilon$ (a); Deformation energy (potential energy) (b); Complementary energy (c) (retrieved from: Blaauwendraad, 2002)

When assuming a linearly-elastic material, however, Hooke's law applies. The stress σ and elongation ε then are related linearly. In this case, the deformation energy E'_s equals the complementary energy E'_c. Hooke's law then describes the following constitutive property, where E is Young's Modulus (Blaauwendraad, 2002):

$$\sigma = E \cdot \varepsilon \qquad \textit{(stiffness formulation)}$$
$$\varepsilon = \frac{\sigma}{E} \qquad \textit{(flexibility formulation)} \qquad [3.6]$$

Accordingly, the deformation energy E'_s can be described as follows:

$$E'_s = \frac{1}{2}\sigma\varepsilon \qquad [3.7]$$

which with [3.6] can be rewritten as:

$$E'_s = \frac{1}{2}E\varepsilon^2 \qquad [3.8]$$

Similarly, the formulas for the complementary energy E'_c can be established:

$$E'_c = \frac{1}{2}E\sigma^2 \qquad [3.9]$$

and:

$$E'_c = \frac{1}{2}\frac{\sigma^2}{E} \qquad [3.10]$$

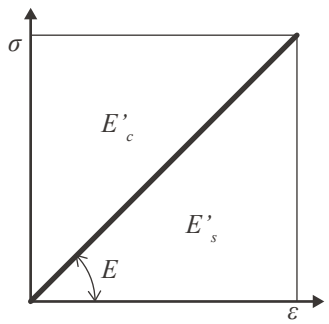

Figure 3.13: Elongation as a function of stress in linearly-elastic materials

In the following sections, units with linearly-elastic material properties are assumed.

3.3.1 NORMAL FORCES

In the previous section, the deformation energy E'_s and complementary energy E'_c were expressed as functions of the stress σ and strain ε. The stress σ is linearly related to the normal forces N subjected to an object, depending on the sectional area A (Borgart & Liem, 2011). This gives the following equations for the stress σ:

$$\sigma = \frac{N}{A} \qquad [3.11]$$

$$\sigma = E \cdot \varepsilon \qquad [3.12]$$

Also, the normal force N can be described as:

$$N = E \cdot A \cdot \varepsilon \qquad [3.13]$$

Rewriting [3.10] and [3.13] gives:

$$E'_{s;N} = \frac{1}{2} N\varepsilon = \frac{1}{2} EA\varepsilon^2 \quad \textit{(per unit of length)} \qquad [3.14]$$

$$E'_{c;N} = \frac{1}{2} \varepsilon N = \frac{1}{2} \frac{N^2}{EA} \quad \textit{(per unit of length)} \qquad [3.15]$$

Figure 3.14b visualises the definition of $E'_{s;N}$ and $E'_{c;N}$ as described in [3.14] and [3.15]. The area above the curve is equal to $E'_{s;N}$ and the area below is equal to $E'_{c;N}$. Since a linearly-elastic material is assumed, the areas are equal to each other, so the deformation energy equals the complementary energy.

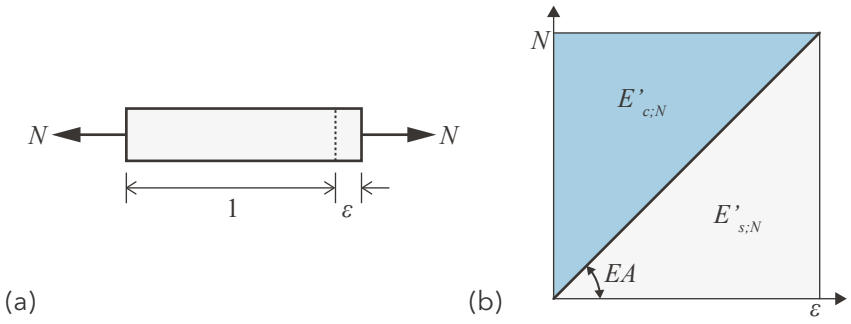

Figure 3.14: Object subjected to tension (retrieved from: Blaauwendraad, 2002)

3.3.2 BENDING MOMENTS

Similar to the complementary energy due to normal forces $E'_{c;N'}$ bending moments in an object also result in complementary energy ($E'_{c;M}$). When an object is subjected to a bending moment, a curvature κ is assumed (Figure 3.15a). In [3.16] the relation between the bending moment M, Young's Modulus E, the moment of Inertia I and the curvature κ is described (Blaauwendraad, 2002).

$$M = E \cdot I \cdot \kappa \quad \textit{(stiffness formulation)} \qquad \kappa = \frac{M}{EI} \quad \textit{(flexibility formulation)} \qquad [3.16]$$

The complementary energy $E'_{c;M}$ is a product of the bending moment M and the curvature κ, which can also be expressed as a function of EI and M, or as a function of EI and κ (Figure 3.15b). This results in functions for $E'_{s;M}$ and $E'_{c;M}$:

$$E'_{s;M} = \frac{1}{2}\kappa = \frac{1}{2}EI\kappa^2 \qquad \textit{(per unit of length)} \qquad [3.17]$$

$$E'_{c;M} = \frac{1}{2}\kappa M = \frac{1}{2}\frac{M^2}{EI} \qquad \textit{(per unit of length)} \qquad [3.18]$$

An analogy is present between the complementary energy from normal forces $E'_{c;N}$ and that from the bending moment $E'_{c;B}$. Comparing [3.15] and [3.18] shows similarities between (1) normal force N and bending moment M, (2) the strain ε and the curvature κ and (3) the sectional area A and the moment of Inertia I. In either case, a load, a displacement and the geometry of the section determine the accumulated energy in a material.

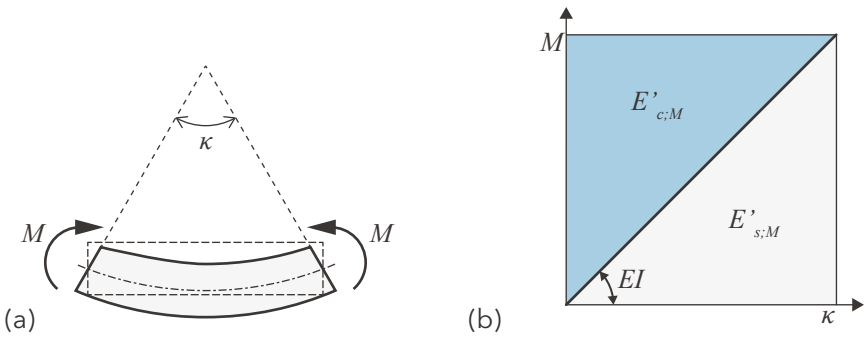

Figure 3.15: Object subjected to bending (retrieved from: Blaauwendraad, 2002)

3.3.3 TOTAL COMPLEMENTARY ENERGY

In *3.1*, the conceptual division between normal forces N and bending moments M in a geometric body has proven to be a valid method for statical calculations. A similar approach is taken in the calculation of structures through complementary energy. *3.3.1* and *3.3.2* explain respectively how the complementary energy by normal force $E'_{c;N}$ and by bending moments $E'_{c;M}$ are calculated numerically. Combining them, the total complementary energy can be determined ([3.19] & [3.20]).

$$\sum E'_c = E'_{c;N} + E'_{c;M} \qquad \textit{(per unit of length)} \qquad [3.19]$$

$$\sum E'_c = \frac{1}{2}\frac{N^2}{EA} + \frac{1}{2}\frac{M^2}{EI} \qquad \textit{(per unit of length)} \qquad [3.20]$$

The formula in [3.20] can be simplified. Both $E'_{c;N}$ and $E'_{c;M}$ contain $1/2E$, which can be eliminated from the equation. This will result in an invalid value for the total complementary energy, but the minimum stays in the same place. Also, A and I can be rewritten, since:

$$A = d \cdot t \qquad [3.21]$$

$$I = \frac{1}{12}dt^3 \qquad \textit{(assuming a rectangular section)} \qquad [3.22]$$

The value for d is irrelevant, and is therefore eliminated from the equation. Substituting [3.21] and[3.22] into [3.20] gives (van Dijk, 2014):

$$\sum E'_c = \bar{N}^2 + \frac{12\bar{M}^2}{t^2} \qquad \textit{(per unit of length)} \qquad [3.23]$$

3.4 FORCE DENSITY METHOD

Another form-finding method is the force density method, first introduced by Schek (1973). It is based on the mathematical assumption that the ratio between the length and the tension within each cable element is a constant value (Lewis, 2003). This force density ratio Q ultimately determines the height of the structure. The force density method does not constrain possible network forms by any geometrical restrictions. The only boundary conditions are: (1) the shape shall be in an equilibrium state, and (2) the cables or bars are connected at the nodes as joints. The method calculates the equilibrium state of a predefined net structure by transforming a system of non-linear equilibrium equations into a system of linear equilibrium equations by introducing a constant force-density ratio (Liem, 2011).

The net structure is composed of a number of nodes that are connected by branches. Two types of nodes are distinguished, being: fixed nodes and free nodes. For the fixed nodes, the x-, y and z-coordinates are known. These x-, y-, and z-coordinates are unknown for the free nodes. The x, y, and z components of the external forces acting on each node are also known. An example for a simple situation is given in Figure 3.16. Left is a conceptualised topology of a net structure with four fixed nodes and five free nodes. Right is the corresponding matrix in which the connections between the branches and nodes are stated.

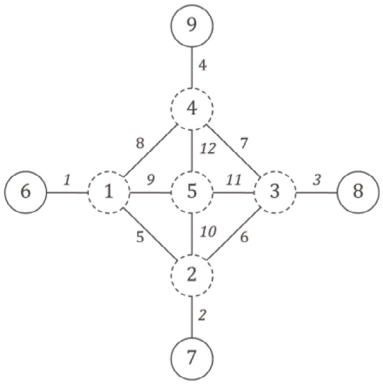

$$C_s = \begin{array}{c} \\ \mathbf{1} \\ \mathbf{2} \\ \mathbf{3} \\ \mathbf{4} \\ \mathbf{5} \\ \mathbf{6} \\ \mathbf{7} \\ \mathbf{8} \\ \mathbf{9} \\ \mathbf{10} \\ \mathbf{11} \\ \mathbf{12} \\ \\ \end{array} \begin{array}{c} \begin{array}{ccccccccc} \mathbf{1} & \mathbf{2} & \mathbf{3} & \mathbf{4} & \mathbf{5} & \mathbf{6} & \mathbf{7} & \mathbf{8} & \mathbf{9} \end{array} \\ \begin{bmatrix} 1 & \cdot & \cdot & \cdot & \cdot & -1 & \cdot & \cdot & \cdot \\ \cdot & 1 & \cdot & \cdot & \cdot & \cdot & -1 & \cdot & \cdot \\ \cdot & \cdot & 1 & \cdot & \cdot & \cdot & \cdot & -1 & \cdot \\ \cdot & \cdot & \cdot & 1 & \cdot & \cdot & \cdot & \cdot & -1 \\ 1 & \cdot & \cdot & -1 & \cdot & \cdot & \cdot & \cdot & \cdot \\ 1 & -1 & \cdot & \cdot & \cdot & \cdot & \cdot & \cdot & \cdot \\ \cdot & 1 & -1 & \cdot & \cdot & \cdot & \cdot & \cdot & \cdot \\ \cdot & \cdot & 1 & -1 & \cdot & \cdot & \cdot & \cdot & \cdot \\ \cdot & \cdot & \cdot & 1 & -1 & \cdot & \cdot & \cdot & \cdot \\ 1 & \cdot & \cdot & \cdot & -1 & \cdot & \cdot & \cdot & \cdot \\ \cdot & 1 & \cdot & \cdot & -1 & \cdot & \cdot & \cdot & \cdot \\ \cdot & \cdot & 1 & \cdot & -1 & \cdot & \cdot & \cdot & \cdot \end{bmatrix} \\ \begin{array}{ccccccccc} & & \boldsymbol{C} & & & & \boldsymbol{C_f} & & \end{array} \end{array}$$

Figure 3.16: Graph and branch-node matrix $C_s = [C \;\; C_f]$ (retrieved from: Schek, 1973)

All nodes are numbered from 1 to n and all branches from 1 to m. The usual branch-node matrix is defined by [3.24].

$$c(i,j) = \begin{cases} +1 & for\ i(j) = 1 \\ -1 & for\ k(j) = 1 \\ 0 & in\ other\ cases \end{cases} \quad [3.24]$$

With this, a branch-node matrix with m nodes and n_s columns can be set up. By classification of free nodes n and fixed nodes n_f, two sub-matrices are distinguished [3.25] (Oosterhuis, 2010).

$$C_s = C + C_f = \left[\begin{array}{ccc|ccc} c_{f_{11}} & \cdots & c_{f_{1n}} & c_{f_{1n+1}} & \cdots & c_{f_{1n_s}} \\ \vdots & \ddots & \vdots & \vdots & \ddots & \vdots \\ c_{f_{m1}} & \cdots & c_{f_{mp}} & c_{f_{m1}} & \cdots & c_{f_{mp}} \end{array}\right] \quad [3.25]$$

Now, several matrices containing force density values (node coordinates and loads) must be formed that are necessary for the assembly of the system of equilibrium equations. First, three n_f-dimensional matrices are formed by specifying the x-, y- and z-coordinates of the fixed points:

$$x_f = \begin{bmatrix} x_{f_1} \\ \vdots \\ x_{f_n} \end{bmatrix} \quad y_f = \begin{bmatrix} y_{f_1} \\ \vdots \\ y_{f_n} \end{bmatrix} \quad z_f = \begin{bmatrix} z_{f_1} \\ \vdots \\ z_{f_n} \end{bmatrix} \quad [3.26]$$

Subsequently, three n_f-dimensional matrices are formed by specifying loads p_x, p_y, and p_z for the free nodes n [3.27]:

$$p_x = \begin{bmatrix} p_{x_1} \\ \vdots \\ p_{x_n} \end{bmatrix} \quad p_y = \begin{bmatrix} p_{y_1} \\ \vdots \\ p_{y_n} \end{bmatrix} \quad p_z = \begin{bmatrix} p_{z_1} \\ \vdots \\ p_{z_n} \end{bmatrix} \quad [3.27]$$

Then, a diagonal $m \times m$ dimensional force density matrix Q is formed by specifying the force density values [3.29]. The force density value is given by [3.28].

$$q = L^{-1} \cdot s \quad [3.28]$$

$$Q = \begin{bmatrix} q_{11} & 0 & 0 \\ 0 & 0 & 0 \\ 0 & 0 & q_{mm} \end{bmatrix} \quad [3.29]$$

Now that all the required matrices have been defined, for each dimension (x, y, z), an equilibrium equation can be formulated [3.30]:

$$\begin{aligned} C^t QCx + C^t QC_f x_f &= p_x \\ C^t QCx + C^t QC_f y_f &= p_y \\ C^t QCx + C^t QC_f z_f &= p_z \end{aligned} \quad [3.30]$$

Each equation can be rewritten by introducing D [3.31], resulting in the equilibrium equations in [3.32]:

$$\begin{aligned} D &= C^t QC \\ D_f &= C^t QC_f \end{aligned} \quad [3.31]$$

$$\begin{aligned} D_x &= D_f D_x = p_x \\ D_y &= D_f D_y = p_y \\ D_z &= D_f D_z = p_z \end{aligned} \quad [3.32]$$

The goal is to find the new x-, y-, and z-coordinates, so the equations from [3.32] must be rewritten to [3.33]:

$$\begin{aligned} x &= D^{-1}(p_x - D_f x_f) \\ y &= D^{-1}(p_y - D_f y_f) \\ z &= D^{-1}(p_z - D_f z_f) \end{aligned} \quad [3.33]$$

Solving the three systems of linear equilibrium equations, the new coordinates of the free nodes can be determined. By then using the branch-node matrix, the points of the corresponding mesh can be constructed resulting in a membrane. The shape will be determined by the force density. Figure 3.17 shows a variety of possibilities from Scheck (1973) that were formed with different force densities.

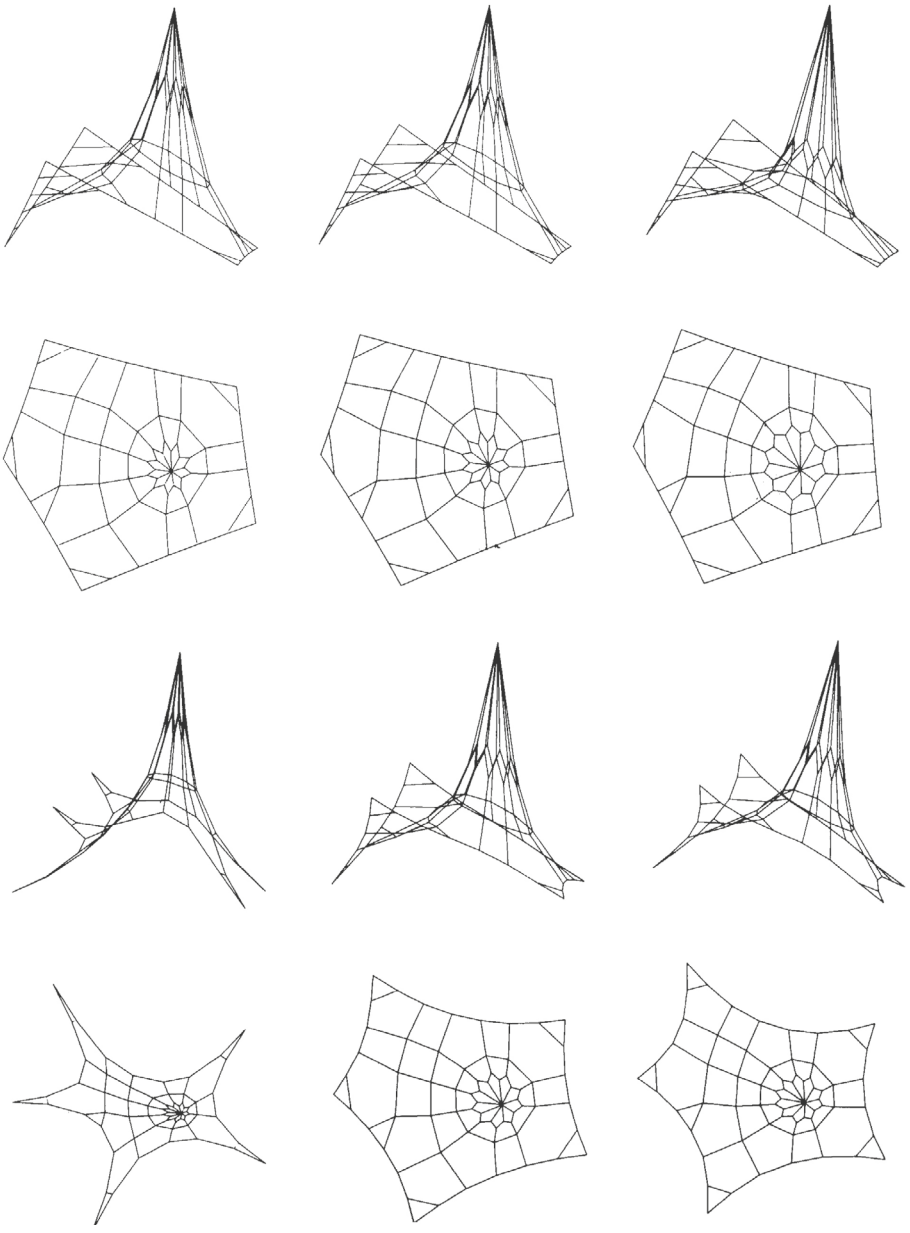

Figure 3.17: Global changes in the force densities of a cable net structure (retrieved from: Scheck, 1973)

3.5 RECIPROCAL FIGURES

In *3.1*, the concept of graphic statics was explained. In graphic statics, the reciprocity between the 'form' and 'force' diagrams is a fundamental notion. This dual relation allows for the analysis and design of structural systems, and helps in visualising force transfer. We explained how a simple two-dimensional system could be assessed using graphic statics, but also how indeterminate systems posed challenges. Similarly, the construction of large force diagrams can be a tedious exercise.

The use of the Airy stress polyhedron in constructing force diagrams was already discovered by Maxwell (1870) in the nineteenth century. Maxwell observed that every self-stressed two-dimensional truss is the projection of a three-dimensional polyhedron. This three-dimensional polyhedron is essentially a discretisation of an Airy stress surface. Now, it was recently demonstrated that not only two-dimensional trusses could be related to the Airy stress function, but that also three-dimensional force diagrams could be developed using this reciprocity (Vansice, Kulkarni, Hartz, Konstantatou, & Baker, 2018). In this section, first a brief introduction of reciprocal diagrams and the different types of reciprocity is given. Next, it is explained how to construct a reciprocal diagram of any polyhedron. This can then be related to the Airy stress polyhedron, which will be applied in a parametric tool later in this thesis (*5.1.2*).

3.5.1 FRAMES AND DIAGRAMS OF FORCES

A structural frame in concept is just a system of straight lines connecting a number of points. When we study equilibrium of such a system, we can consider these points to act on each other with forces that have the direction of a straight line connecting these points. When these forces attempt to pull the points towards each other, we speak of tension. When the forces keep the points apart, we speak of compression (Maxwell, 1870). An important notion here is that if we consider a point in a structure that is in equilibrium, all forces acting on this point must also be in equilibrium. Hence, if we would draw a force polygon from the forces acting in this point, with the directions as vectors and the force magnitude as length, this polygon would form a closed loop. This statement holds for two-dimensional systems as in *3.1.1*, but should by default also

hold for complex three-dimensional systems. The essential property of reciprocity is the mutual relationship, like five over three is related to three over five. All properties in a form diagram are reciprocal to that of a force diagram and vice versa.

In order to get a better understanding of reciprocal figures, let us first evaluate a simple two-dimensional case. Consider the force polygon as in Figure 3.18a. Each line represents a force, acting on the point in which it meets other lines. We can, however, even consider the polygon without the notion of forces at all. We then just regard it as a geometrical polygon with points, lines and faces. The polygon consists of a triangle ABC, separated into three triangles by lines P, Q and R. Each line in the polygon has a corresponding line in its reciprocal figure that faces in the perpendicular direction (Maxwell, 1870). The lines that meet in a point in the first diagram, form a closed polygon in the second, and vice versa. The example given in the figure is, however, the Maxwell projection. Would we construct a Cremona diagram, then all corresponding lines would run parallel. This duality was first introduced by Poncelet, and is summarised in Figure 3.19.

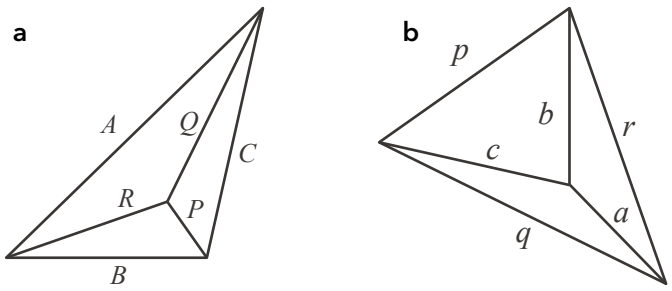

Figure 3.18: (a) Simple force polygon and (b) one possible reciprocal figure (retrieved from: Maxwell, 1870)

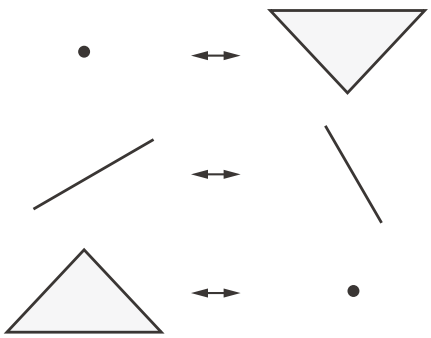

Figure 3.19: Poncelet projective geometry duality (retrieved from: Konstantatou & McRobie, 2016)

If we consider the polygon from Figure 3.18a to be a force polygon that is in equilibrium, we could draw its forces acting on the points as vectors and form closed head-to-tail diagrams (Figure 3.20). Now, since there are only three forces acting on the point, the system is statically determinate; only one possible shape for the form diagram is possible. If we scale one vector, then all vectors must be scaled with equal magnitude to form a closed polygon.

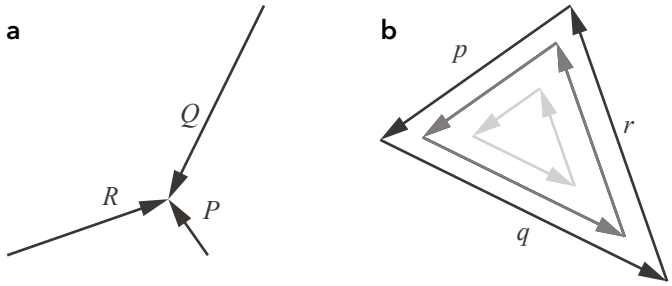

Figure 3.20: Forces acting on a point (a) and its reciprocal head-to-tail diagram in equilibrium (b)

Let us consider a force polygon in self-stress as in Figure 3.21. From each vertex we can create a reciprocal closed force polygon. These force polygons can then be fit together to form the reciprocal polyhedron (Figure 3.22). When these polygons are fitted together, each force has an overlapping force in the other direction. We call these pairs of forces, and they are equal in magnitude but opposite in direction (Crapo & Whiteley, 1993). The forces in each bar are governed by [3.34]. The scalars are given by ω, and are in compression if $\omega \leq 0$ and in tension if $\omega \geq 0$, and p is the point that is assessed.

$$\omega_{ij}(p_j - p_i) \quad at\ p_i \qquad\qquad \omega_{ij}(p_i - p_j) \quad at\ p_j \tag{3.34}$$

Equilibrium in a point is reached if [3.35]:

$$\sum_j \omega_{ij}(p_j - p_i) = 0 \tag{3.35}$$

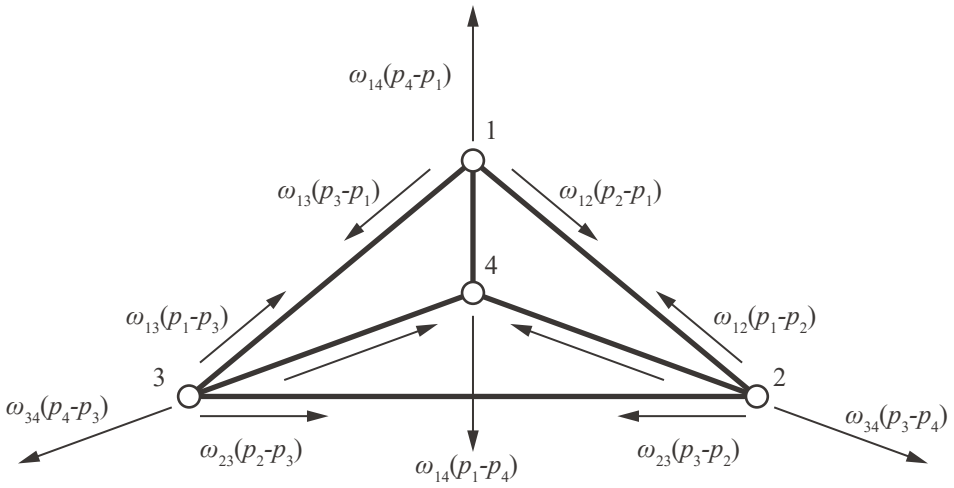

Figure 3.21: Equilibrium of forces in a polyhedron of self stress for each vertex (retrieved from: Crapo & Whiteley, 1993)

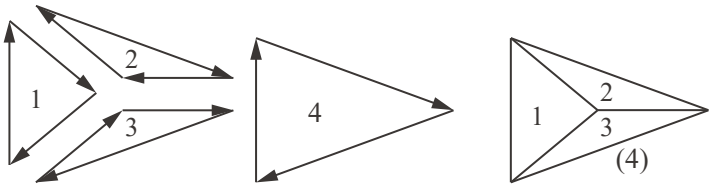

Figure 3.22: Force polygon of each vertex together form the drawing of the dual polyhedron (retrieved from: Crapo & Whiteley, 1993)

3.5.2 THREE-DIMENSIONAL RECIPROCAL FIGURE

Until now we have reviewed reciprocal diagrams in projection and in free space, i.e. we talked about two-dimensional systems without notion of their location in a given space. Now, for a three-dimensional system that is in self-stress, the same properties apply. Again, if we consider a polyhedron (which is the three-dimensional version of a polygon), we know that all points are in equilibrium, so that the sum of all force vectors is equal to zero. From this polyhedron we want to construct the three-dimensional reciprocal figure. Now let us first state that from now on we consider a three-dimensional coordinate system xyz. The same relations from Figure 3.19 apply, so a vertex becomes a plane, an edge becomes an edge (and is perpendicular) and a plane becomes a vertex. Since a polyhedron is nothing more than a summation of planar surfaces, each surface is given by [3.36] (Whiteley, Ash, Bolker, & Crapo, 2013).

$$\alpha x + \beta y - z - \gamma = 0$$
$$\alpha' x + \beta' y - z - \gamma' = 0 \quad [3.36]$$

If we consider two surfaces intersecting each other in edge E, we get an image like in Figure 3.23. The edge E separating the faces from each other, is reciprocal to the edge e connecting the reciprocal vertices. Since this is a diagram following Maxwell's theorem, these edges are perpendicular to each other in projection. Multiple edges e in the second figure in turn enclose a face, and these faces together form the reciprocal polyhedron. From the formula for faces in the force diagram from [3.36] we can get vertices of the form diagram and vice versa. This gives us the overview below ([3.37], [3.38], [3.39], [3.40]) (Vansice et al., 2018).

$z = \alpha x + \beta y + \gamma$ *(Face of Polyhedron A)* [3.37]

$(-\beta, \alpha, \gamma)$ *(Vertex of Polyhedron B)* [3.38]

(q, r, s) *(Vertices of Polyhedron A)* [3.39]

$z = rx - qy + s$ *(Face of Polyhedron B)* [3.40]

These formulas, however, describe infinite planes. So in order to determine the intersection edges so that planes become actual trimmed surfaces, we can equate the formulas ([3.41] & [3.42]).

$$\alpha x + \beta y + \gamma = \alpha' x + \beta' y + \gamma' \quad [3.41]$$
$$rx - qy + s = r' x - q' y + s \quad [3.42]$$

Such an exercise can also be done through computing multiple intersecting surfaces, returning trimmed surfaces. This procedure is implemented in the parametric tool, and is explained in *5.1.2*.

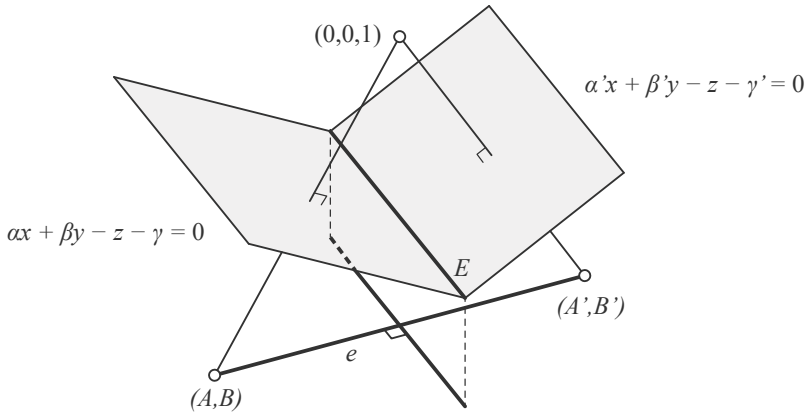

Figure 3.23: Normals to the face planes create an edge e that is reciprocal (and perpendicular) to the separating edge E (retrieved from: Whiteley et al., 2013)

3.5.3 THE AIRY STRESS FUNCTION

A structural system that is in equilibrium, is equally in a state of self-stress. If we then consider the system as the summation of force diagrams, we can imagine its reciprocal figure. We can, however, also consider the Airy stress function as a force diagram. Since the Airy stress function is in most cases of shell structures a gradual sloping surface, it must first be discretised in order to obtain its reciprocal figure. After all, the reciprocity is just a geometrical relation between planes and vertices and edges and other edges. To do so, first the stress resultants acting on the element are converted into single vectors per Cartesian direction by multiplying it by the width that the stress acts on. Then a fold is made on this resulting vector, corresponding to changes of curvature of the surface. We notate this with κ. The double-headed arrows represent this additional folding (Figure 3.24) (Calladine, 1977).

Now, κ is an approximation of the change in curvature, which is called the angular defect (Calladine, 1977). So the stress resultants acting through the fold are given by this angular defect. We can calculate it by taking the angle between two planes, since this is the change of curvature from one plane to another. This occurrence is later applied in the parametric tool.

Now, the stress resultants are determined by [3.43] to [3.46]. A visual interpretation of the Airy stress function of a simply-supported beam subjected to a distributed load is given in Figure 3.25. Here all stress resultants and their differential equations are shown as product of the Airy stress. It should be recognised that the direction of the angular defect κ is perpendicular to that of the stress resultants N, since it is the curvature in the perpendicular direction that determines these stress vectors.

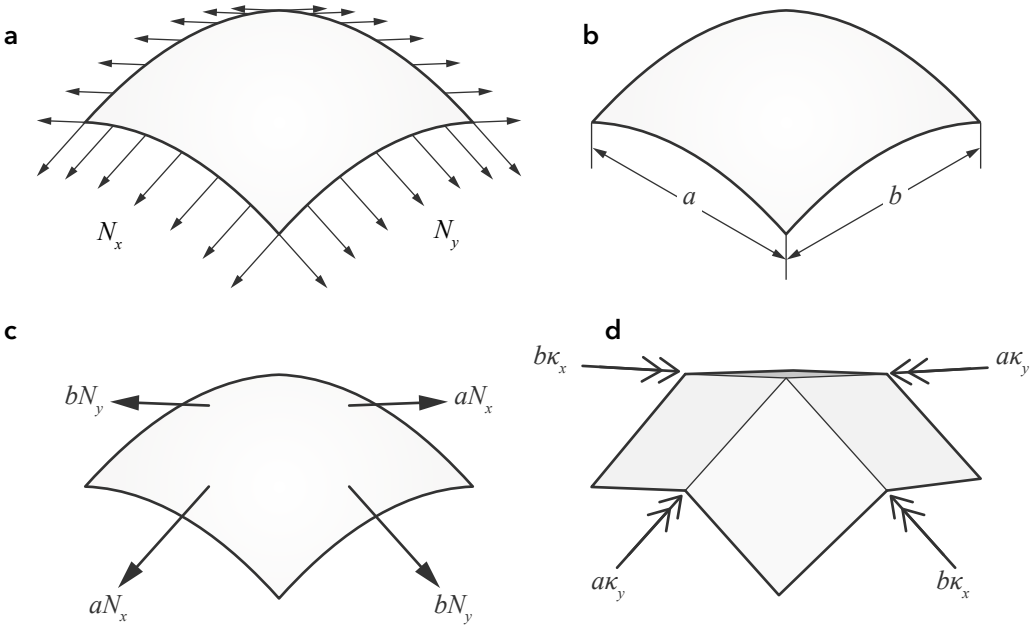

Figure 3.24: In-plane stress resultants in an element (a), dimensions of element (b), stress resultants converted to single vectors (c) and polygonised version of the element (d) (retrieved from: Calladine, 1977)

$$N_x = \left[\frac{\partial \phi}{\partial y}\right]_y \qquad [3.43]$$

$$N_y = \left[\frac{\partial \phi}{\partial x}\right]_x \qquad [3.44]$$

$$N_{xy} = \left[\frac{\partial \phi}{\partial y}\right]_x \qquad [3.45]$$

$$N_{yx} = \left[\frac{\partial \phi}{\partial x}\right]_y \qquad [3.46]$$

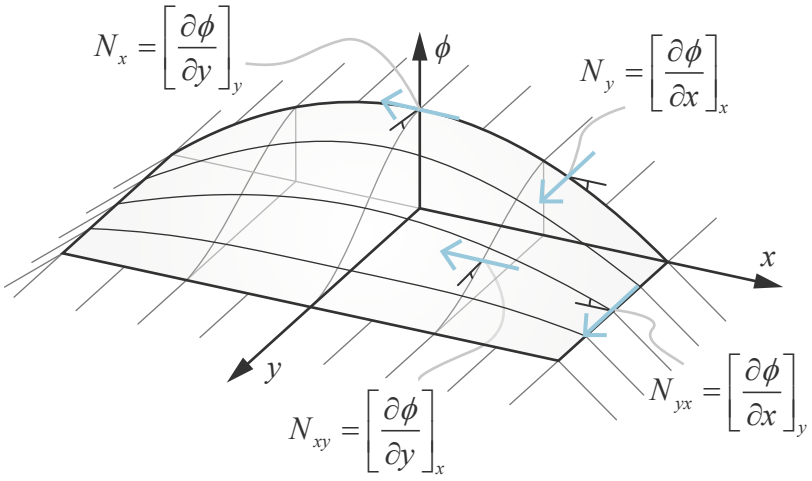

Figure 3.25: Differential equations describing relation between the stress resultants and the Airy stress function (example is of a simply-supported beam subjected to a distributed load

One must, however, be careful in regarding the Airy stress function of a three-dimensional system when creating the reciprocal diagram, since the Airy stress function is just a three-dimensional visualisation of a two-dimensional instance. In order to obtain the actual stress resultants, we must know the angle that the stress resultant operates in. Consider Figure 3.26. An element with the dimensions dx and dy can be projected onto the curved surface to form ds_1 and ds_2. This curved surface can in our case be the thrust surface or the shell structure. From basic angular properties, we can establish [3.47] and [3.48] (Heyman, 1977). Interestingly, the shear stress resultants remain the same so that we get [3.49].

$$\bar{N}_x = \frac{\cos\psi}{\cos\theta} N_x \qquad [3.47]$$

$$\bar{N}_y = \frac{\cos\theta}{\cos\psi} N_y \qquad [3.48]$$

$$\bar{N}_{xy} = N_{xy} = N_{yx} = \bar{N}_{yx} \qquad [3.49]$$

However, in our case $\bar{N}$ is already known, so we must calculate N. In order to do so we can rewrite the equations above into [3.50] and [3.51]. To calculate the angular differences ψ and θ respectively corresponding to the x- and y-axes, we use [3.52] and [3.53].

$$N_x = \frac{\overline{N}_x}{\frac{\cos\psi}{\cos\theta}} = \frac{\overline{N}_x \cos\theta}{\cos\psi} \quad [3.50]$$

$$N_y = \frac{\overline{N}_y}{\frac{\cos\theta}{\cos\psi}} = \frac{\overline{N}_y \cos\psi}{\cos\theta} \quad [3.51]$$

$$\cos\theta = \left[1 + \left(\frac{dz}{dy}\right)^2\right]^{-\frac{1}{2}} \quad [3.52]$$

$$\cos\psi = \left[1 + \left(\frac{dz}{dx}\right)^2\right]^{-\frac{1}{2}} \quad [3.53]$$

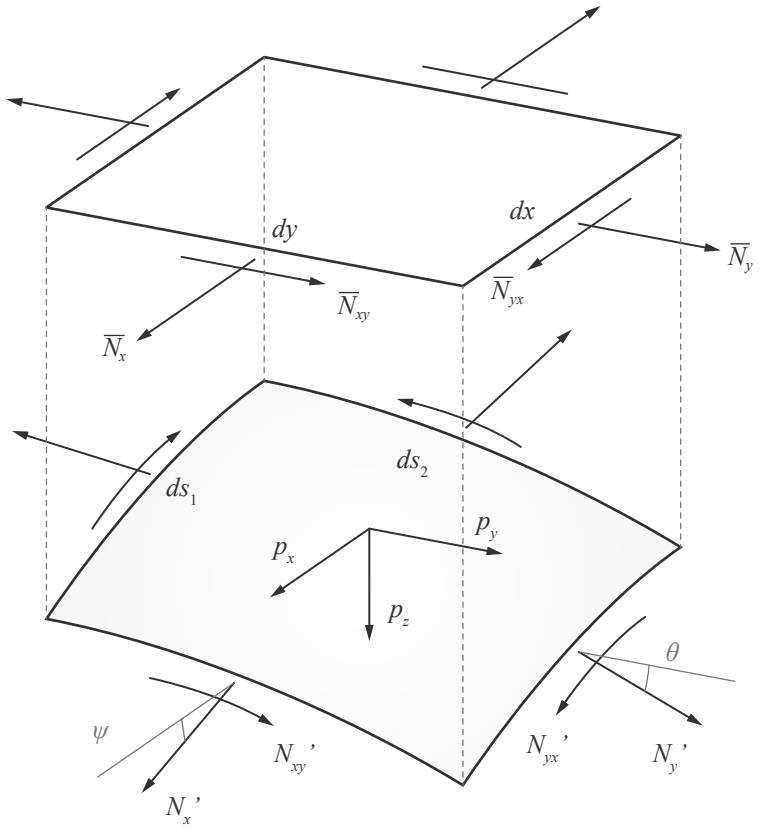

Figure 3.26: Membrane stress resultants N_x, N_y and N_{xy} (= N_{yx}) in the tangent plane to the surface (retrieved from: Heyman, 1977)

4. PLATE AND SHELL ANALOGIES

4 PLATE AND SHELL ANALOGIES

4.1 METHODOLOGY

In *1.4.2*, a hypothesis was stated as follows: *'An analogy is present between (1) the geometry of a moment hill of a plate and (2) the thrust surface of a shell subjected to a distributed load, and their boundary conditions are mutually related.'* In this section, the hypothesis will be further investigated.

In order to do so, two geometrical cases are assessed, being (1) a rectangle and (2) a circle. For these bodies a connection is made between the planar geometry and their three-dimensional funicular counterparts. In other words, we aim to generate a complex shell structure from a simple shape. By reviewing these two different shapes, we expect to have a conclusive description of a shell structure, and its relation with its planar projection.

In this chapter, we first assess a rectangular plate. For this, different boundary conditions are assigned to the analysis cases. We generate the $\bar{M}$-hill of each of the cases, which results in a specific geometry of a shell surface. FEM is used to evaluate shell behaviour, allowing for the comparison between different cases. Subsequently, analytical proof is given to support the findings from the analyses.

The case of the circular plate has a reversed approach. First, a shell-like dome is determined analytically. The result of this process is then analysed and examined on the occurring bending moments.

The chapter ends with a conclusion, in which the above approach in generating shell-like structures is evaluated. The results from this will be used in **Chapter 5** for the development of a parametric tool.

4.2 RECTANGULAR

4.2.1 SIMPLY-SUPPORTED FLAT RECTANGULAR PLATE

Consider a rectangular plate that is simply-supported at the corners. Each support is fixed in x- y- and z-direction, but allows for free rotation. The plate is subjected to an evenly distributed load p, causing out-of-plane mechanical behaviour i.e. bending moments m_{xx} and m_{yy}. The case is visualised in Figure 4.1.

In his thesis, Liang (2012) proposed a parametric design tool in Grasshopper with which the mechanical behaviour of certain input geometries could be assessed using the Force Density Method (FDM). This tool is employed to analyse the structural behaviour of the plate. Like FEA, FDM requires meshing of the geometry prior to analysing. A mesh size λ is therefore indicated below.

One of the outputs of the tool is the sum of bending moments $\bar{M}$. The tool will be used to generate the $\bar{M}$-hill of this analysis case. Given its analytical character, the tool does not allow for input of material properties. Poisson's ratio v is therefore considered zero, meaning that $\bar{M} = m_{xx} + m_{yy}$. Also, the magnitude of $\bar{M}$ is arbitrary, so the vertical scale of the shell can be adjusted. For the analysis, the following properties for the plate are assumed:

$a = b =$	$20\ m$
$p =$	$-1\ kN/m^2$
$\lambda =$	$0.5\ m$
$v =$	0

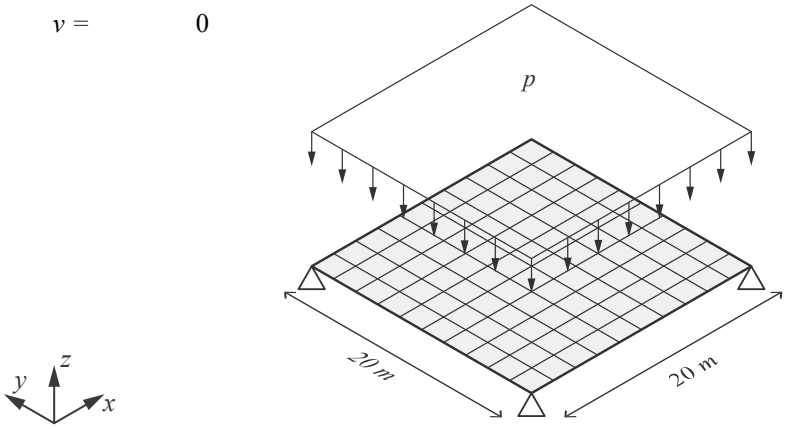

Figure 4.1: Simply-supported flat rectangular plate subjected to a distributed load q

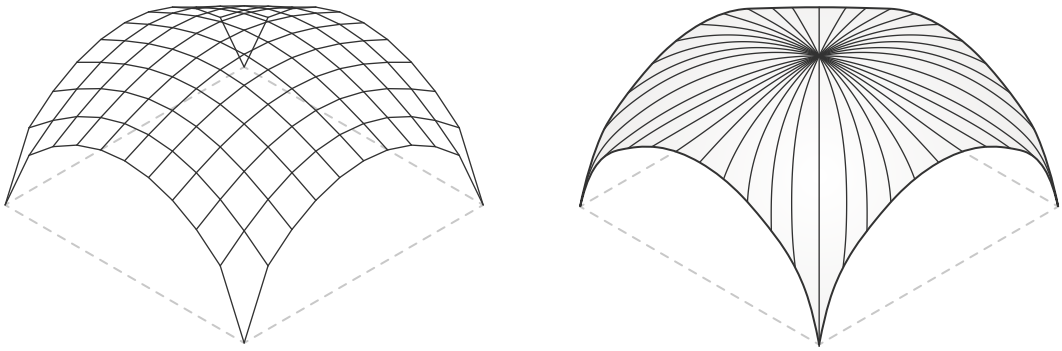

Figure 4.2: (a) $\bar{M}$-hill of a plate on four supports generated with the FDM-tool of Liang (2012) and (b) its rainflow diagram

Figure 4.2a shows the $\bar{M}$-hill of the rectangular plate generated by the design tool of Liang. It can clearly be observed that the $\bar{M}$-hill resembles a shell-like structure. Generating its rainflow analogy gives Figure 4.2b. The shear force trajectories are drawn towards the supports to a certain extent, but primarily end at the edges. This indicates that shear forces in the perpendicular direction act at the edges to direct the load towards the supports. A complete rainflow diagram is illustrated in Figure 4.3, an image similar to one earlier introduced by Beranek (1976).

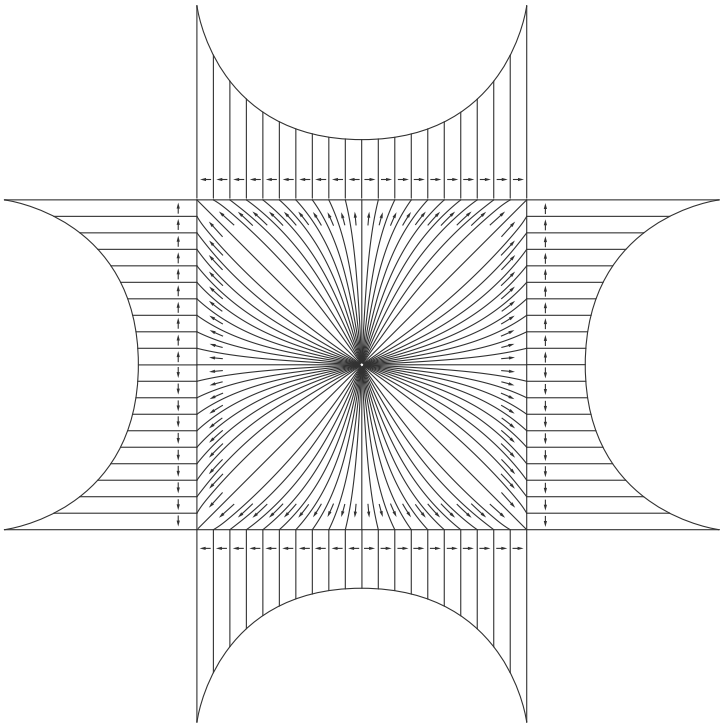

Figure 4.3: Rainflow analogy of flat plate supported on four corners (with load transfer along free edges) (retrieved from: Beranek, 1976, adapted to this load case)

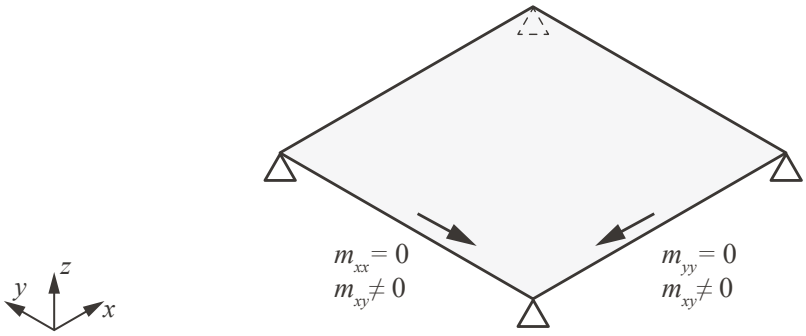

Figure 4.4: m_{xx} equals zero along the y-edges and m_{yy} equal zero along the x-edges

It can be concluded that m_{xx} equals zero along the edges parallel to the y-axis, and m_{yy} equals zero along the edges parallel to the x-axis (Figure 4.4). This knowledge will later be used in explaining the analogy between the plate and its shell equivalent.

In search of the shell equivalent for the rectangular plate from *4.2.1*, we must define its boundary conditions. Where the rectangular plate was simply-supported on four corners, it is likely that its reciprocal shell figure requires different support conditions. In the following chapter, we look for a case in which the duality can better be exploited. The rainflow diagram from Figure 4.3 shows shear force trajectories running towards the edges. These forces must not be absorbed by the material, since this would cause bending moments to occur along the edges.

4.2.2 SHELL EQUIVALENT

We take the $\bar{M}$-hill from *4.2.1* as our analysis geometry. From the rainflow diagram we can expect that the shell must be supported at the edges in order to absorb the projected load. A shell will be assessed of which the edges are assumed to be semi-rigid and hinged ($w_z = 0$ and $\varphi \neq 0$). The shell is then subjected to a projected load (Figure 4.5). The following properties for the shell are assumed:

$l_x = l_y =$ 20 m
$q =$ -10 kN/m^2
$\lambda =$ 0.5 m
$v =$ 0

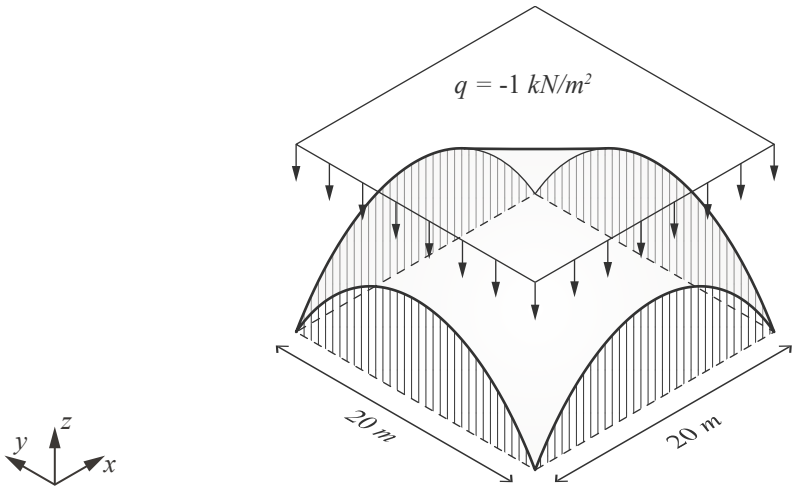

Figure 4.5: $\bar{M}$-hill rectangular plate supported along semi-rigid edges

The rainflow analogy in a flat plate illustrates the $\bar{M}$-hill of a plate as such, and gives insight in the load paths of the plate. In the case of a plate on four supports (Figure 4.4), bending moments at the edges can clearly be observed. The following analogies exist: between the bending moment m_{xx} and m_{yy} in a plate and membrane forces n_{xx} and n_{yy} in a shell. At the edges of a plate on four supports, a bending moment occurs, meaning that normal forces occur in its shell equivalent. Hence, the shell equivalent is supported at the edges, with the ability to transfer membrane forces along its axis, but not perpendicular to it (Figure 4.7).

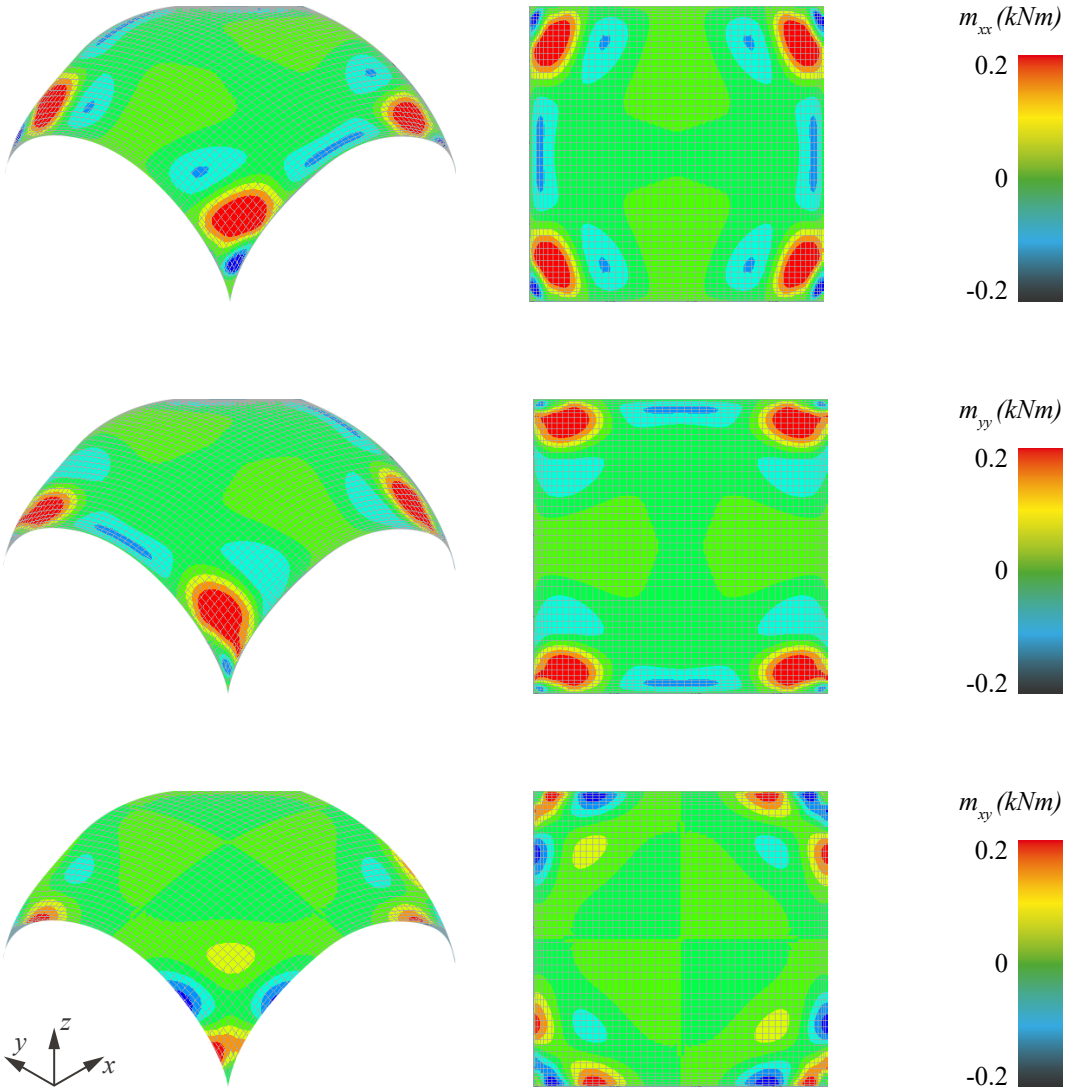

Figure 4.6: m_{xx} (top), m_{yy} (middle) and m_{xy} (bottom) of analysed shell from DIANA FEA

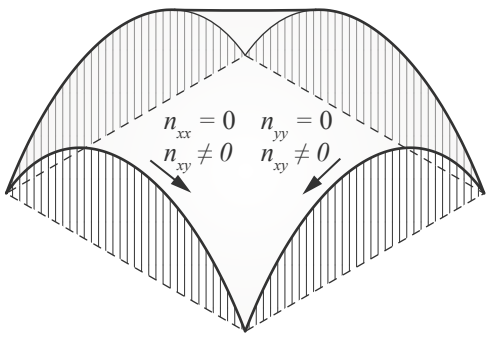

Figure 4.7: n_{xx} equals zero along the y-edges and n_{yy} equals zero along the x-edges

4.2.3 TWISTLESS RECTANGULAR PLATE (SIMPLY-SUPPORTED)

To obtain an $\bar{M}$-hill that matches the thrust surface better, we must minimise the torsional moments m_{xy} that occur in the initial plate; we must create a 'twistless' plate. The twistless case was first introduced by Beranek & Hobbelman (1984). In a twistless plate, bending moments in the x-direction are only caused by the deflections in x-direction, and equally bending moments in the y-direction are only caused by deflections in y-direction. This is allowed by the absence of torsional moments; the plate can be regarded as two individual systems of beams in x- and y-direction.

In order to create a twistless case, we take a plate of $l_x \times l_y$ with a thickness t, and an orthotropic rim with a height b_x and b_y. The ratio between the dimensions of the orthotropic rim and those of the isotropic plate is hereby essential, since it gives us the ability to control the stress distribution. Beranek and Hobbelman proposed a formula to calculate this ratio, given in [4.1] (Beranek & Hobbelman, 1984). Here, B is the beam stiffness and P is the field stiffness.

$$B_x \cdot B_y = P_x \cdot P_y \qquad [4.1]$$

In order to solve this equation, it is given that:

$$P_x = \frac{1}{12} \cdot l_y t^3 \quad and \quad P_y = \frac{1}{12} \cdot l_x t^3 \qquad [4.2]$$

and:

$$B_x = \frac{1}{12} b_x t_x^{\,3} \quad and \quad B_y = \frac{1}{12} b_y t_y^{\,3} \qquad [4.3]$$

where:

load intensity $= f$

load transfer in x-direction $= f_x \quad = f\alpha$

load transfer in y-direction $= f_y \quad = (1-\alpha)f$

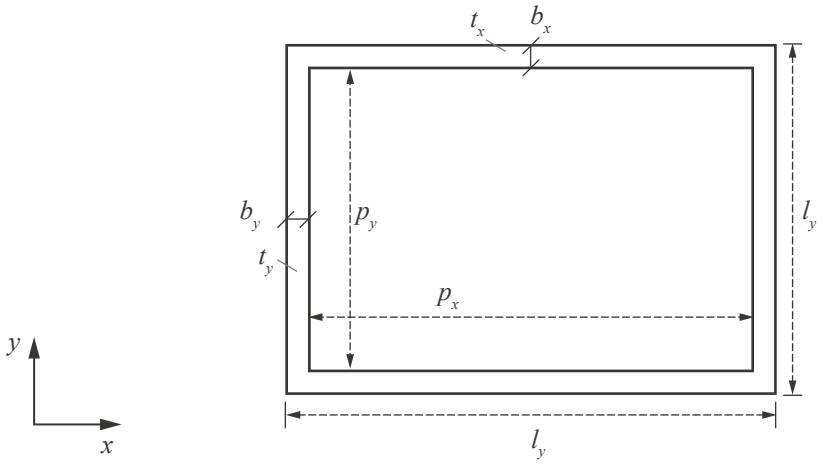

Figure 4.9: Overview of signs Twistless case

In Figure 4.9, an overview is given of all signs related to the formulas of the Twistless case. We must calculate t_x and t_y in order to generate an element with minimal torsional moments. To allow for comparison with *4.2.1*, the same dimensions are assumed, giving the following properties:

$$
\begin{aligned}
l_x = l_y &= 20\ m \\
b_x = b_y &= 0.5\ m \\
t &= 0.2\ m \\
t_x = t_y &
\end{aligned}
$$

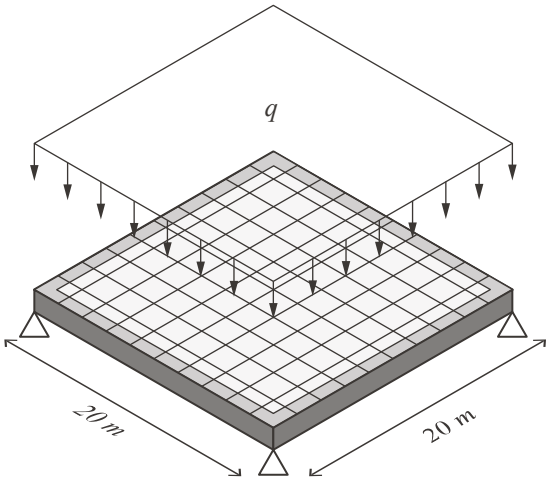

Figure 4.8: Tiwstless plate subjected to a load q

Now, for the given properties we must calculate the ratio between the thickness t of the plate and the thicknesses t_x and t_y of the rim. We do so using the formulas from [4.1], [4.2] and [4.3]. Since each half of the loads in x- and y-direction is directed to each support, we divide the field stiffnesses P_x and P_y by two. t_x and t_y are equal due to the symmetrical character of the analysis case. For the given thickness, we calculate a thickness of each rim by [4.4].

$$
\begin{aligned}
B_x B_y &= P_x P_y \\
\left(\frac{1}{12} b_x {t_x}^3\right)\left(\frac{1}{12} b_y {t_y}^3\right) &= \left(\frac{1}{12}\cdot\frac{1}{2} l_y t^3\right)\left(\frac{1}{12}\cdot\frac{1}{2} l_x t^3\right) \\
\left(\frac{1}{12}\cdot 0{,}5\cdot {t_x}^3\right)\left(\frac{1}{12}\cdot 0{,}5\cdot {t_y}^3\right) &= \left(\frac{1}{12}\cdot\frac{1}{2}\cdot 20\cdot 0{,}2^3\right)\left(\frac{1}{12}\cdot\frac{1}{2}\cdot 20\cdot 0{,}2^3\right) \\
\left(\frac{1}{24} {t_x}^3\right)\left(\frac{1}{24} {t_y}^3\right) &= \left(\frac{1}{150}\right)\left(\frac{1}{150}\right) \\
\frac{1}{576} {t_{x;y}}^6 &= \frac{1}{22500} \\
22500 {t_{x;y}}^6 &= 576 \\
{t_{x;y}}^6 &= \frac{576}{22500} \\
t_{x;y} &= \sqrt[6]{\frac{576}{22500}} \\
t_{x;y} &\approx 0{,}543
\end{aligned}
\qquad [4.4]
$$

The thickness of the rim is calculated to be approximately $0{,}543m$. This gives us all properties to make and analyse a twistless case. To execute this analysis we use DIANA FEA. First, we validate whether the case is indeed twistless. Now, some local torsional moments always occur. Most importantly, however, the system should work as two independent systems of beams in x- and y-direction. This can be evaluated by checking if the bending moments in one direction are linear across its axis, and the displacements forming a translation surface. When we consider the results of m_{xx} and m_{yy} in Figure 4.10, it can be observed that they behave independent from each other. It can also be noticed

that m_{xy} is almost zero across the entire field, apart from some local torsional moments where the rim and the plate meet. In Figure 4.11, a side-view of the displacements w is given. Here it becomes clear that ∂w is equal from left to right.

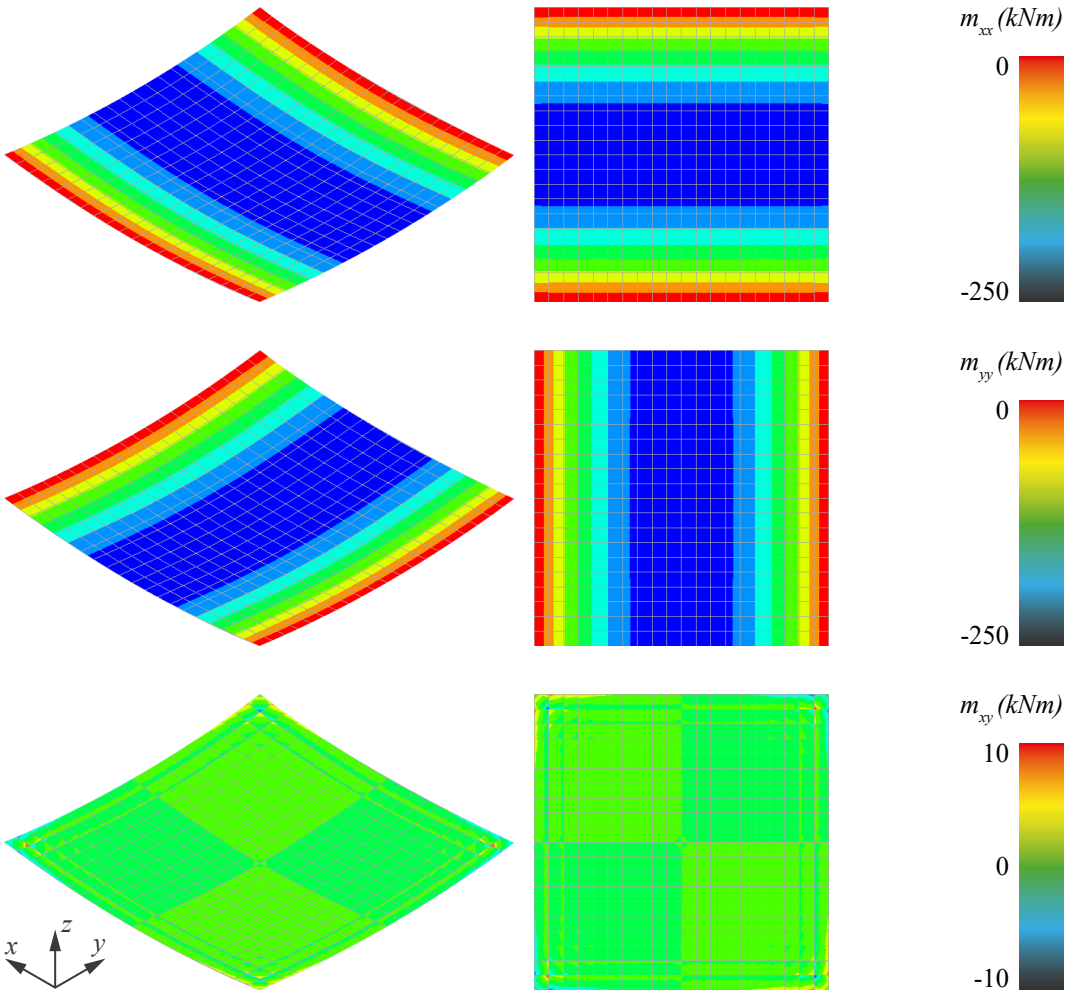

Figure 4.10: m_{xx} (a), m_{yy} (b) and m_{xy} (c) of twistless rectangular plate

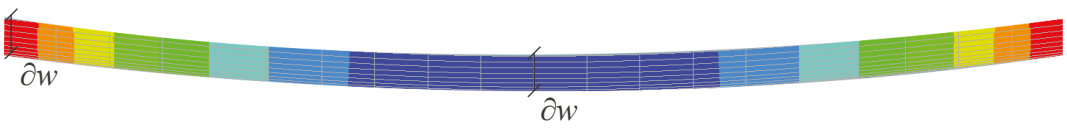

Figure 4.11: ∂w is constant across both axes

4.2.4 SHELL EQUIVALENT

Now, the hypothesis was stated that the $\bar{M}$-hill of a plate on four supports was related to a shell with semi-rigid edges. The results in *4.2.2* showed that indeed little bending moments occurred, but *4.2.2* also proved this geometry not to be completely funicular. Therefore, we now analyse the $\bar{M}$-hill of the twistless plate, again supported on semi-rigid edges.

The values of m_{xx} and m_{yy} from 4.2.3 can be used to generate the $\bar{M}$-hill. Poisson's ratio of 0 is assumed, so that $M = m_{xx} + m_{yy}$. The values of each coordinate are exported to Rhinoceros, where they are used to generate a point cloud (Figure 4.12a). This point cloud is then interpolated three-dimensionally, computing an average surface through all points (Figure 4.12b). It should be noted that this is just an approximation of the actual $\bar{M}$-hill, and that many factors, for instance the meshing size, can influence the results. The $\bar{M}$-hill is also scaled in z-direction, so that it is neither too shallow nor to steep to analyse. Adjusting the load case in *4.2.3* would have a similar effect. We now consider the case as visualised in Figure 4.14, supported on semi-rigid edges so that $w = 0$ and $\frac{\partial w}{\partial n}$. The following properties are assigned to the analysis:

$l_x = l_y =$ = $20\ m$
t = $0.1\ m$
λ = $0.5\ m$
v = 0

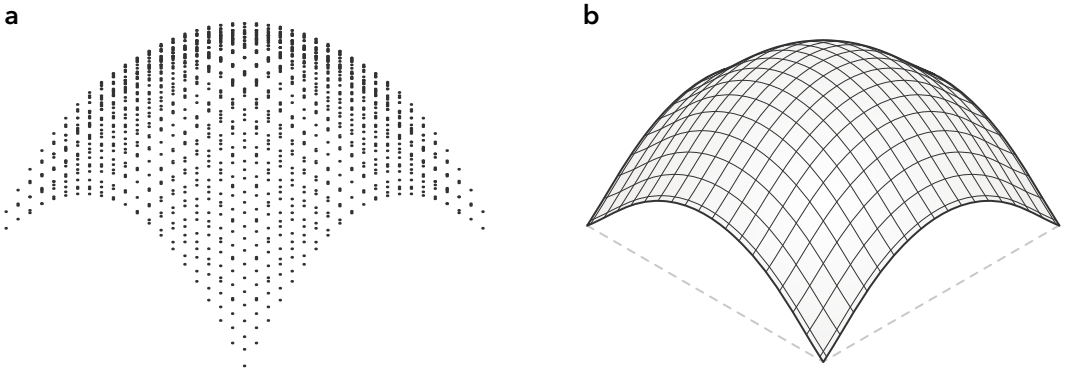

Figure 4.12: (a) Point cloud of sum of m_{xx} and m_{yy} generated from values from DIANA FEA, (b) resulting shell surface modelled in Rhinoceros

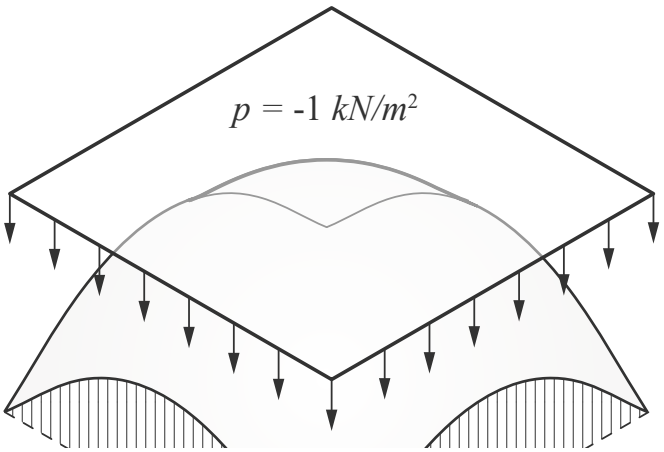

Figure 4.13: Analysis setup of shell from rectangular twistless plate

The results from DIANA FEA are given in Figure 4.14. When we first evaluate m_{xx}, we notice that negative bending moments occur at the corners. These areas are indicated by the blue colour. Now, regarding how the geometry was generated, this could well be a result of the interpolation. The deviation in the z-direction between vertices here is much larger than in the centre. It is likely that with a more accurately formed $\bar{M}$-hill, these localised bending moments would decrease. Correspondingly, the same occurrence takes place for m_{yy}. The fact that these images are not exactly identical shows that the geometry is slightly unsymmetrical.

If we evaluate the results further, we notice that the bending moments are very low from the centre outwards. Once again it is likely that since the accuracy is higher in the middle, the geometry shows better shell behaviour there. Once we compare this shell surface with the shell from Figure 4.6, we observe a slight improvement in shell behaviour.

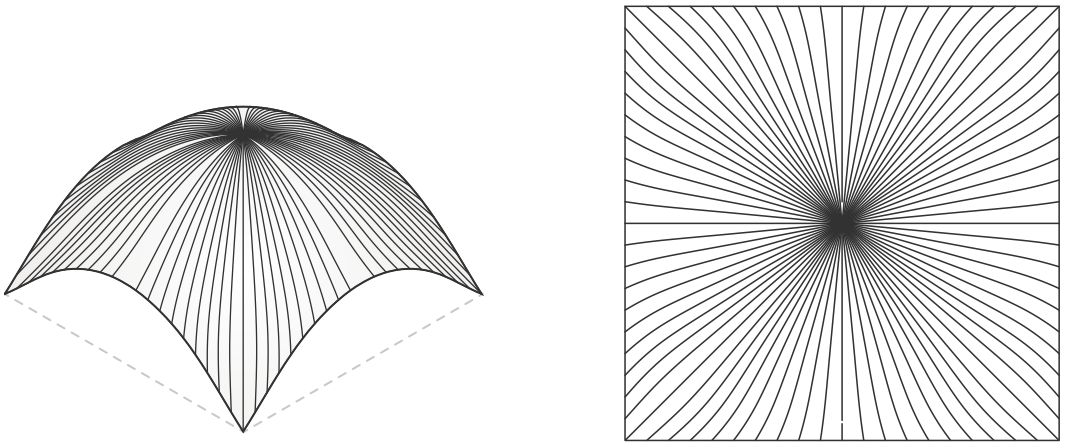

Figure 4.15: Rainflow analogy of shell from twistless rectangular plate (a) and the same diagram projected

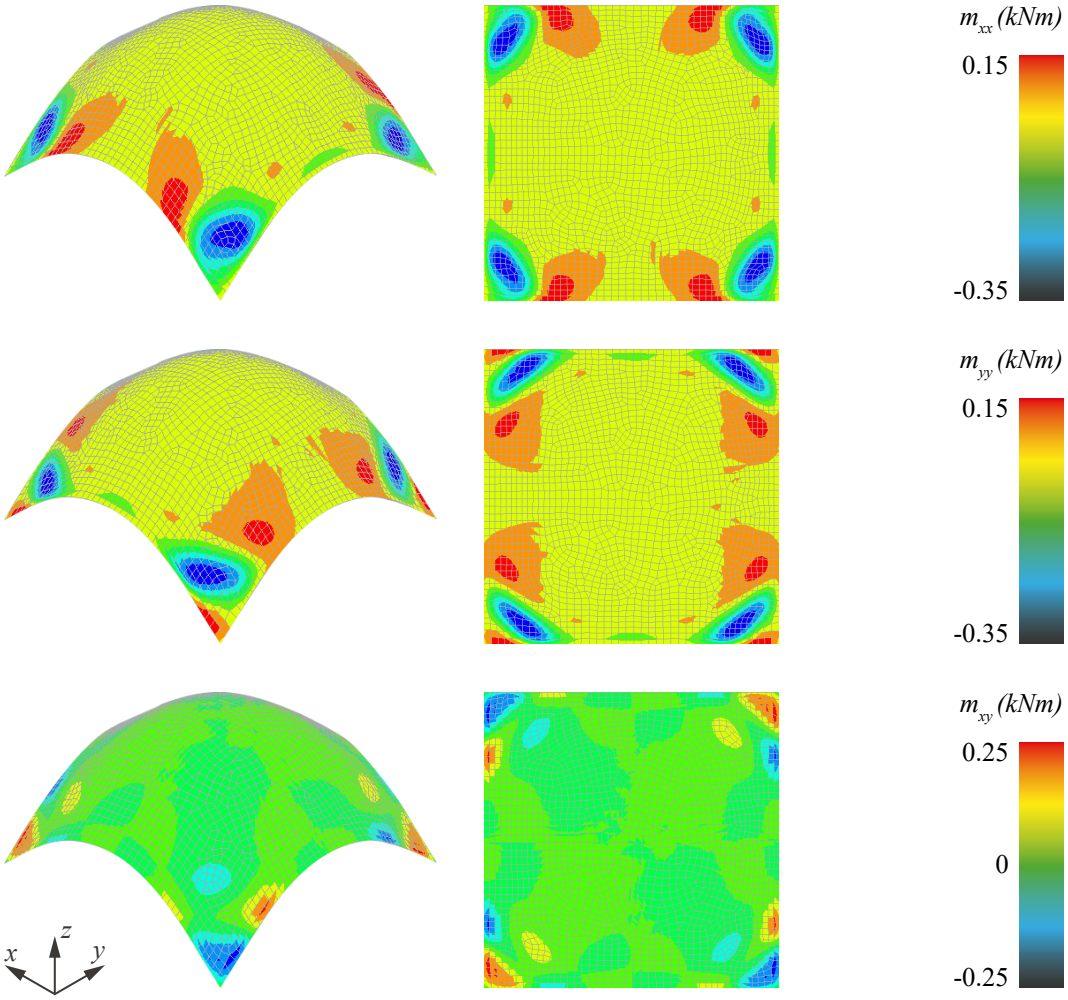

Figure 4.14: m_{xx} (a), m_{yy} (b) and m_{xy} (c) of shell from $\bar{M}$-hill twistless rectangular plate

4.2.5 CONCEPTUAL RECTANGULAR PLATE

The case of *4.2.3* gives valuable information in the understanding of shell geometry. To obtain full understanding, however, more cases should be analysed. Now consider a shell supported on four corners. Imagining its analogous flat plate is not as straightforward as the one in the previous chapter. Therefore, we need to introduce a conceptual plate; a plate with no bending moments at the edges. All forces should be directed towards the point supports. If we imagine the rainflow analogy of this, we would possibly get something like Figure 4.16.

A similar drawing was already introduced by Beranek (Figure 4.18). This image does not show the rainflow of a shell, but that of four equal flat plates on columns supported in the centres. Theoretically, the four parts can be considered one continuous plate supported on four columns (Figure 4.17). By drawing a rectangle through the four column supports, we get an interesting rainflow diagram in the centre. We observe shear trajectories starting at the centre point flowing towards the columns exclusively. The bounding edge acts hereby as an asymptote; the closer each trajectory approaches the boundary edge, the more parallel it runs. If we imagine the shape of the $\bar{M}$-hill, we can expect the rotation φ perpendicular to the edges to equal 0. After all, the plates and the distributed load are both symmetrical, and at these edges a maximum value of w_z is reached.

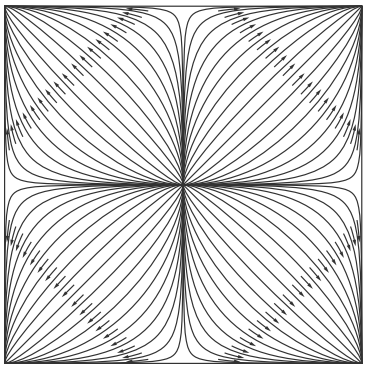

Figure 4.16: Expected rainflow diagram of hypothetical plate without out-of-plane mechanical behaviour

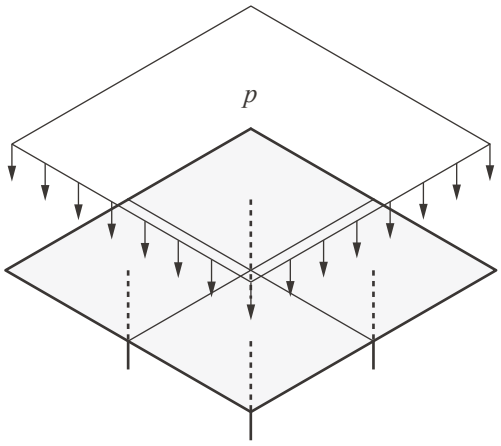

Figure 4.17: Continuous floor supported on four columns, subjected to a distributed load q

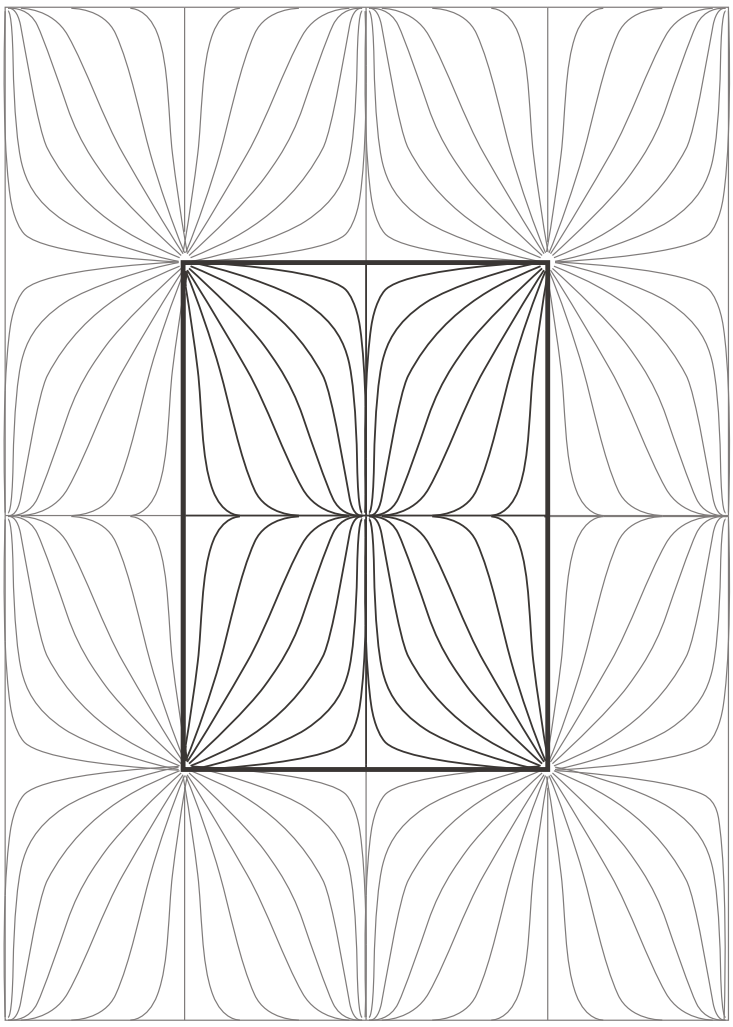

Figure 4.18: Rainflow diagram of continuous floor on four columns

To simulate this case, a rectangular plate is taken that is simply-supported on the four corners. Other than the plate from *4.2.1*, we consider additional boundary conditions for the edges; $\varphi_x = 0$ for the edges parallel to the x-axis, and $\varphi_y = 0$ for the edges parallel to the y-axis. All edges should still allow for vertical deformation w_z. The plate is subjected to an evenly distributed load q, causing out-of-plane mechanical behaviour i.e. bending moments m_{xx} and m_{yy}.

The analysis tool created by Liang does not support these desired boundary conditions. Therefore, to calculate this plate, DIANA FEA is now used.

The following properties are assigned to the surface:

$l_x = l_y =$	$20\ m$
$q =$	$-1\ kN/m^2$
$\lambda =$	$0.5\ m$
$\nu =$	0

Calculating this plate results in values for m_{xx}, m_{yy} and m_{xy}, which are visualised in Figure 4.20. The deflection can clearly be observed on the left-side images. A Poisson's ratio of 0 is used, so $\bar{M} = m_{xx} + m_{yy}$. The calculated values for m_{xx} and m_{yy} will further be used to generate the $\bar{M}$-hill of this plate.

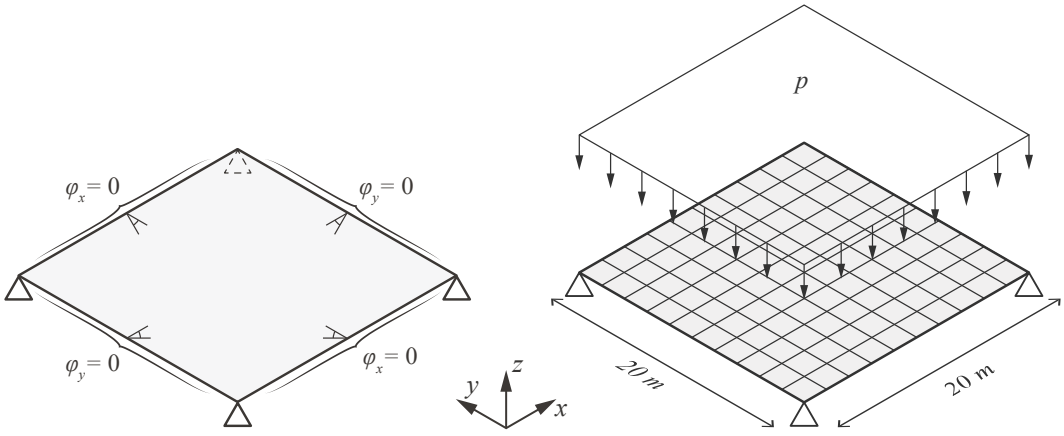

Figure 4.19: Boundary conditions plate on four supports with no rotation around the edges (left), same plate subjected to a load q (right)

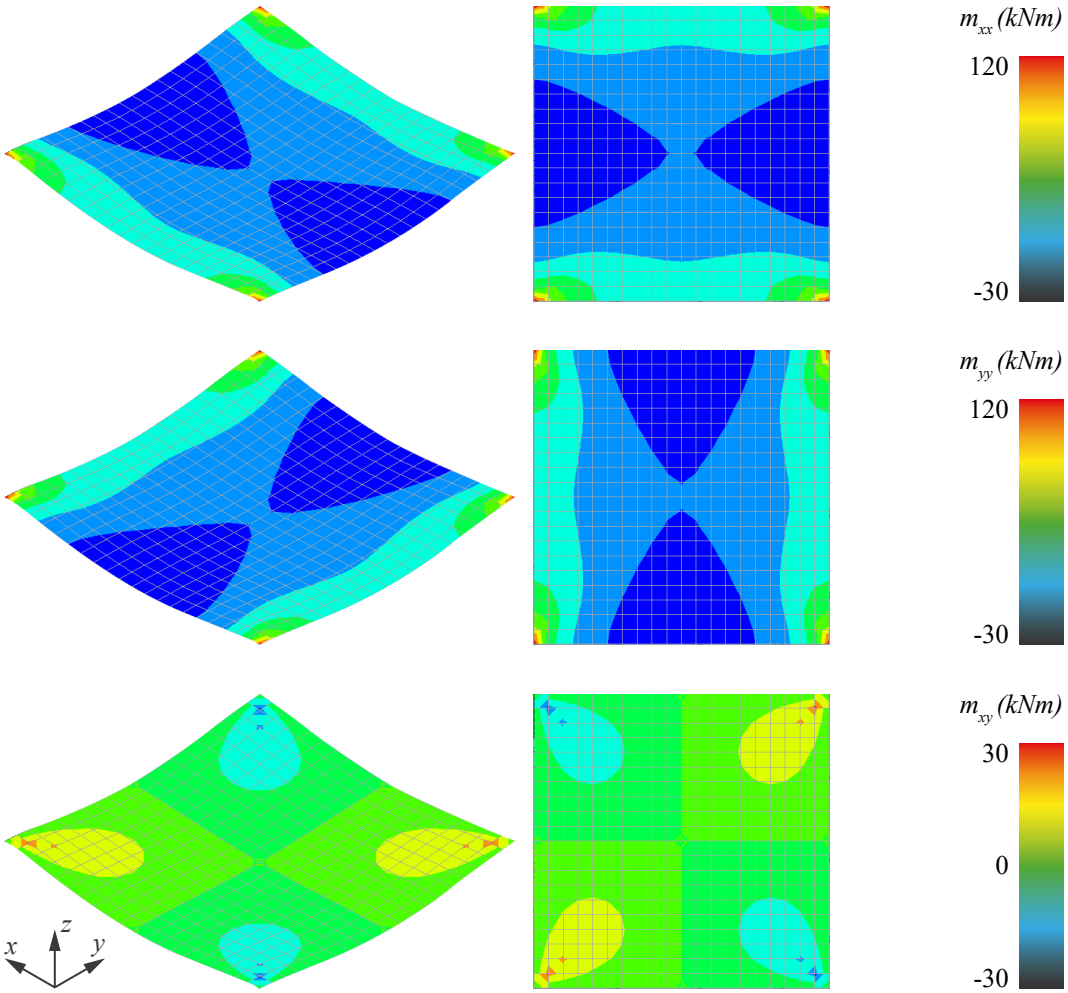

Figure 4.20: m_{xx} (a), m_{yy} (b) and m_{xy} (c) of flat plate with no rotation around the edges, deformation is shown in the left images

4.2.6 SHELL EQUIVALENT

From the sum of the values for m_{xx} and m_{yy}, a point cloud is generated in Rhinoceros (Figure 4.21a). Each x- and y-coordinate in DIANA FEA comprises four nodes (since four mesh planes meet here), so correspondingly there are four values for $\bar{M}$ per coordinate. Hence, the point cloud is merely an approximation of what the $\bar{M}$-hill looks like.

A NURBS-surface is created by taking the average z-coordinate of each point, and then interpolating these averages. The resulting surface is an approximation of the actual $\bar{M}$-hill (Figure 4.21b). We can then use this surface as input for the parametric tool of Liang, with which the rainflow diagram can be generated (Figure 4.21b).

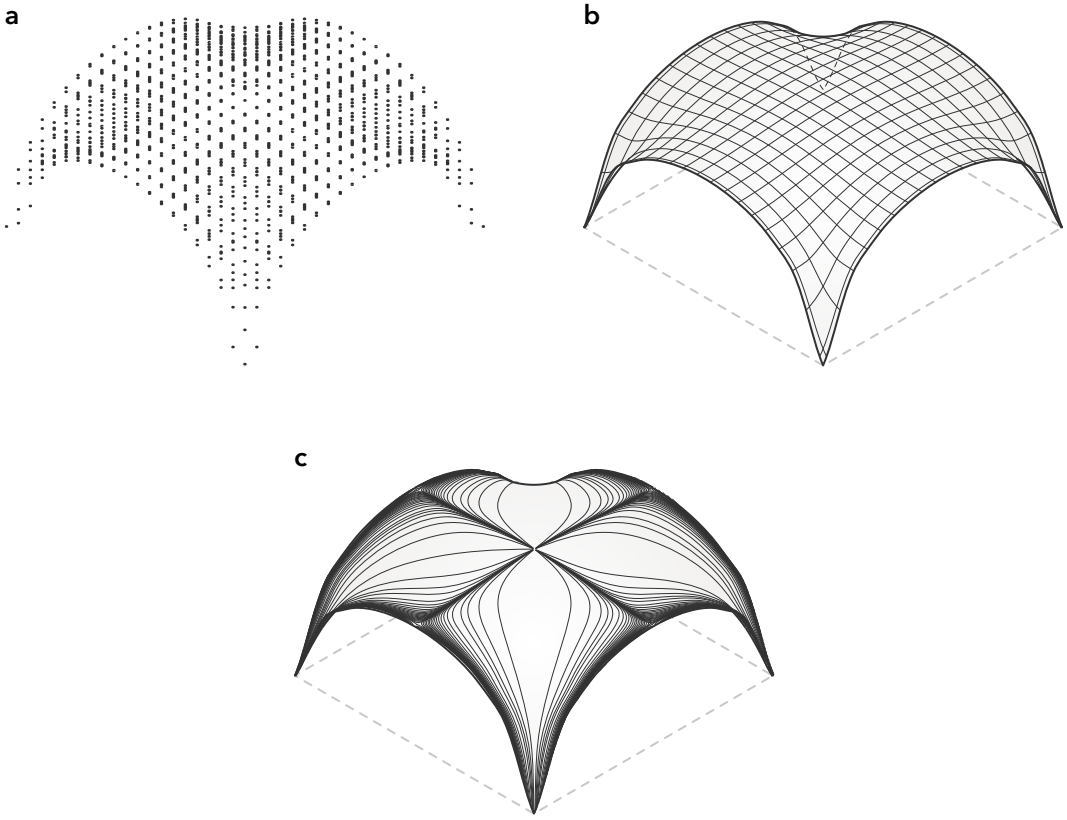

Figure 4.21: (a) Point cloud of sum of m_{xx} and m_{yy} generated from values from DIANA FEA, (b) resulting shell surface modelled in Rhinoceros and (c) rainflow diagram of the shell surface

To determine its shell-like behaviour, the surface created before must be assessed in DIANA FEA. The following properties are assigned to the surface:

$l_x = l_y =$ 20 m
$q =$ -1 kN/m^2
$\lambda =$ 0.5 m
$v =$ 0

The results of the analysis are visualised in Figure 4.22. First of all, localised bending moments occur at the supports. The surface turns concave, which likely does not follow the thrust surface. It can also be noticed that the shell is steep at the supports and very flat in the centre. It will therefore act more like a plate there. Since a two-dimensional thrust line has a parabolic shape (just like the moment line), the edges must have a parabolic shape too. After all, the forces acting along this line must be directed towards the support along the same line. We can then consider that edge a two-dimensional arch. When we look at Figure 4.22, we can observe this edge not to be shaped fully parabolic, and can expect both negative and positive moments here. It can be concluded that the surface is not a translation of two two-dimensional moment lines, and that the torsional moments m_{xy} affect m_{xx} and m_{yy}. In order to create a 'pure' $\bar{M}$-hill, we must eliminate m_{xy}.

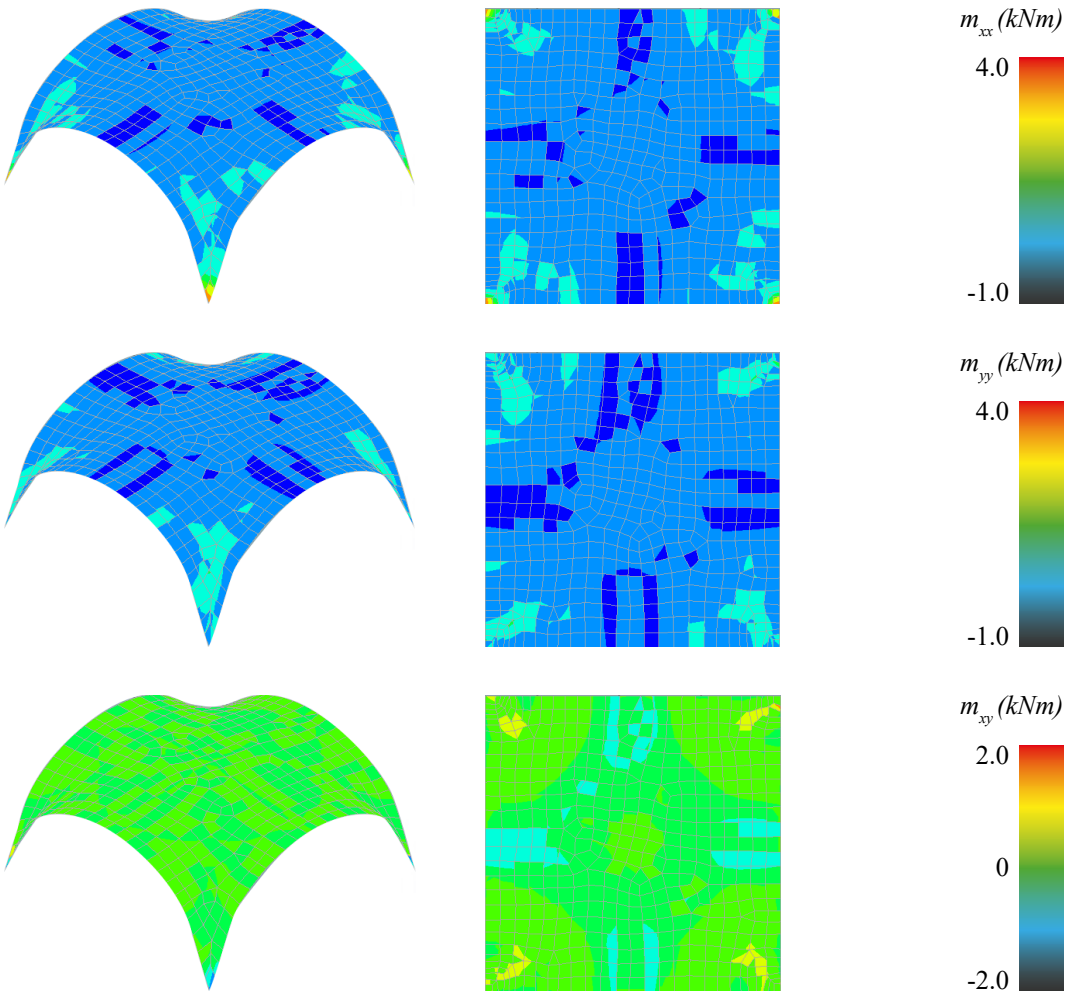

Figure 4.22: m_{xx} (a), m_{yy} (b) and m_{xy} (c) of shell surface from $\bar{M}$-hill flat plate with no rotation around the edges

4.2.7 TWISTLESS RECTANGULAR PLATE (NO ROTATION)

From *4.2.6*, it was concluded that m_{xx} and m_{yy} are affected by m_{xy}, resulting in an unsatisfactory $\bar{M}$-hill. In order to eliminate this effect, we must eliminate the torsional moments m_{xy} in the plate. To do so, we will create a twistless case again. This is done with help from the formulas [4.1], [4.2] and [4.3], where:

load intensity $= f$
load transfer in x-direction $= f_x = f\alpha$
load transfer in y-direction $= f_y = (1-\alpha)f$

In Figure 4.9, an overview is given of all signs related to the formulas of the Twistless case. We must calculate t_x and t_y in order to generate an element with minimal torsional moments. To allow for comparison with *4.2.5*, the same dimensions are assumed, giving the following properties:

$l_x = l_y = 20\ m$
$b_x = b_y = 0.5\ m$
$t = 0.2\ m$
$t_x = t_y$

Since this is a symmetrical case, we know that t_x and t_y will have the same value. We calculate these values for the given case as in [4.5].

To validate the twistless behaviour of the plate with the calculated t_x and t_y, the case is loaded into DIANA FEA. Again, no rotation at the edges is allowed so that $\varphi_x = 0$ around the x-axis and $\varphi_y = 0$ around the y-axis (equal to the case in Figure 4.19). Since the plate should now work as two independent systems in x- and y-direction, the displacement should form a translation surface; the displacements as a result of m_{xx} are translated across those of m_{yy} (or vice versa). Equally, the contour lines of m_{xx} and m_{yy} are linear; they work as two individual two-dimensional systems. The results are shown in Figure 4.23. The values of m_{xy} are of a completely different magnitude than those of m_{xx} and m_{yy}, showing that the torsional moments are practically negligible. Even more so, it can be observed that both m_{xx} and m_{yy} behave uniformly along their axes, indicating

that the structure acts as two individual systems in x- and y-direction. When the results are compared to those of a plate without an orthotropic rim (such as Figure 4.20), the difference can clearly be observed.

$$
\begin{aligned}
B_x B_y &= P_x P_y \\
\left(\frac{1}{12} b_x {t_x}^3\right)\left(\frac{1}{12} b_y {t_y}^3\right) &= \left(\frac{1}{12} l_y t^3\right)\left(\frac{1}{12} l_x t^3\right) \\
\left(\frac{1}{12} \cdot 0{,}5 \cdot {t_x}^3\right)\left(\frac{1}{12} \cdot 0{,}5 \cdot {t_y}^3\right) &= \left(\frac{1}{12} \cdot 20 \cdot 0{,}2^3\right)\left(\frac{1}{12} \cdot 20 \cdot 0{,}2^3\right) \\
\left(\frac{1}{24} {t_x}^3\right)\left(\frac{1}{24} {t_y}^3\right) &= \left(\frac{1}{75}\right)\left(\frac{1}{75}\right) \\
\frac{1}{576} {t_{x;y}}^6 &= \frac{1}{5625} \\
5625 {t_{x;y}}^6 &= 576 \\
{t_{x;y}}^6 &= \frac{576}{5625} \\
t_{x;y} &= \sqrt[6]{\frac{576}{5625}} \\
t_{x;y} &\approx 0{,}863
\end{aligned}
\qquad [4.5]
$$

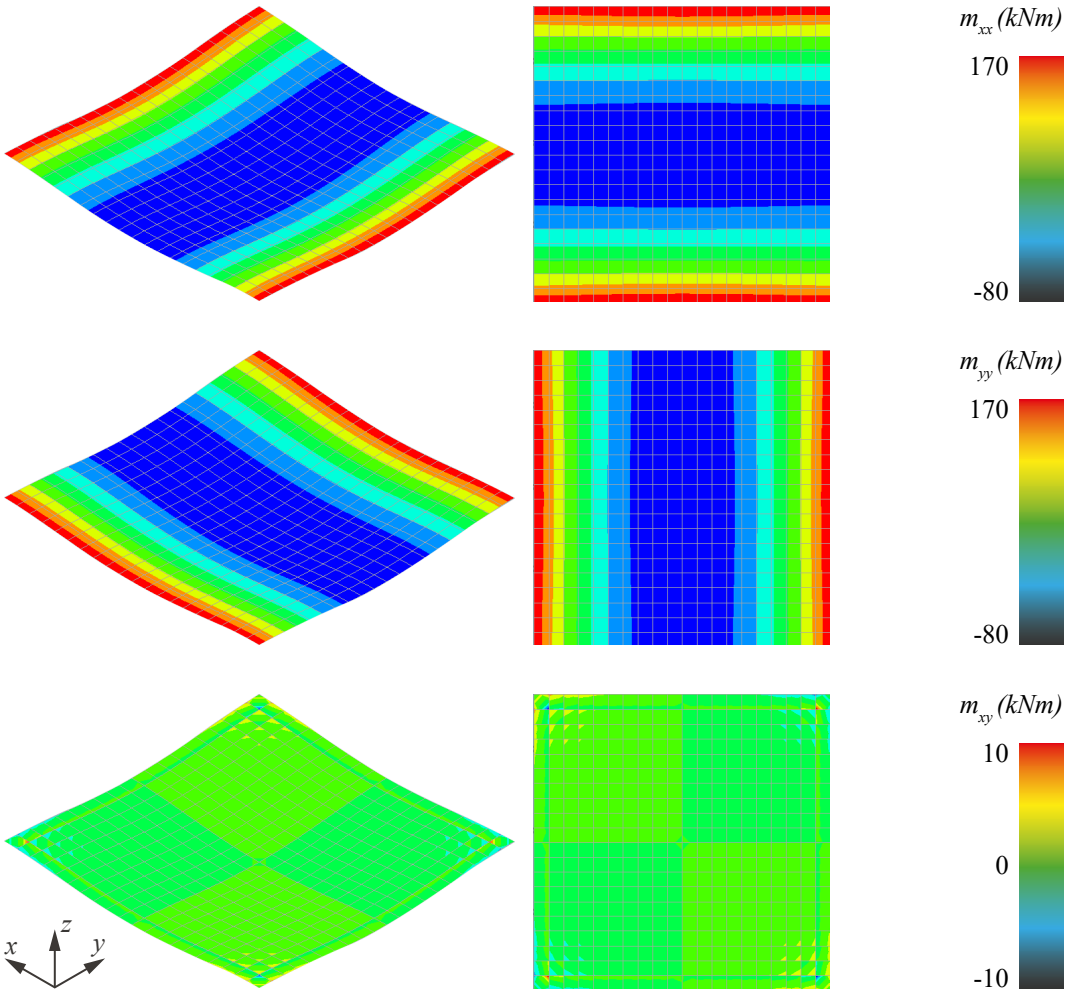

Figure 4.23: m_{xx} (a), m_{yy} (b) and m_{xy} (c) of twistless plate with no rotation around the edges

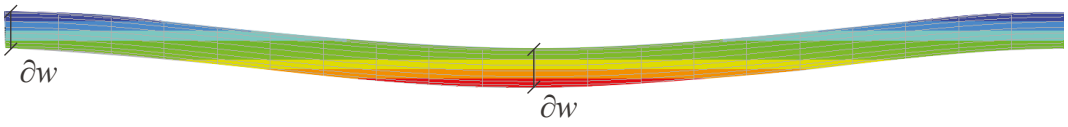

Figure 4.24: ∂w is constant across both axes

4.2.8 SHELL EQUIVALENT

From the sum of the values for m_{xx} and m_{yy} generated in DIANA FEA, a point cloud is generated in Rhinoceros. A NURBS-surface is created by taking the average z-coordinate of each point, and then interpolating these averages. The resulting surface is an approximation of the actual $\bar{M}$-hill (Figure 4.25a). The rainflow diagram is given in Figure 4.25b.

To determine its shell-like behaviour, the surface must be assessed in DIANA FEA. The following properties are assigned to the surface:

$l_x = l_y =$	$20\ m$
$q =$	$-1\ kN/m^2$
$\lambda =$	$0.5\ m$
$v =$	0

The structure is subjected to a projected load q, and is simply-supported on its four corners. Calculating in DIANA FEA gives the images in Figure 4.26a-c. It can clearly be observed that peak bending moments in all directions occur at the supports. When we look closer at the shape of the shell in these areas, we find that the geometry turns concave there, possibly causing tension in the structure. This geometrical defect can likely be explained by the generation process of the $\bar{M}$-hill using DIANA FEA. It is possible that the point cloud generated is not completely accurate, especially at the

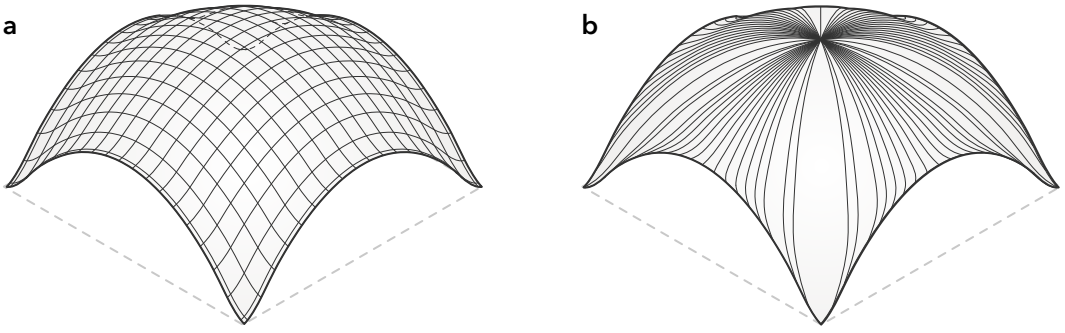

Figure 4.25: (a) $\bar{M}$-hill modelled in Rhinoceros with point cloud from DIANA FEA and (b) rainflow diagram of the shell surface

supports. As previously discussed, at each x,y-coordinate four points are generated (except at the edges, here only two points). Generally, the values for the bending moments per coordinate lie close to each other. But at the supports, the deviation is much higher, likely indicating a decrease in accuracy. Should we construct such a shell structure, however, the supports would need more attention anyway, since high amounts of localised stresses would occur.

The colour scale of Figure 4.26 is set to the lowest and highest values occurring throughout the entire shell. Therefore, little insight in the bending moments away from the supports is given. In order to obtain a better ability to analyse the results, a

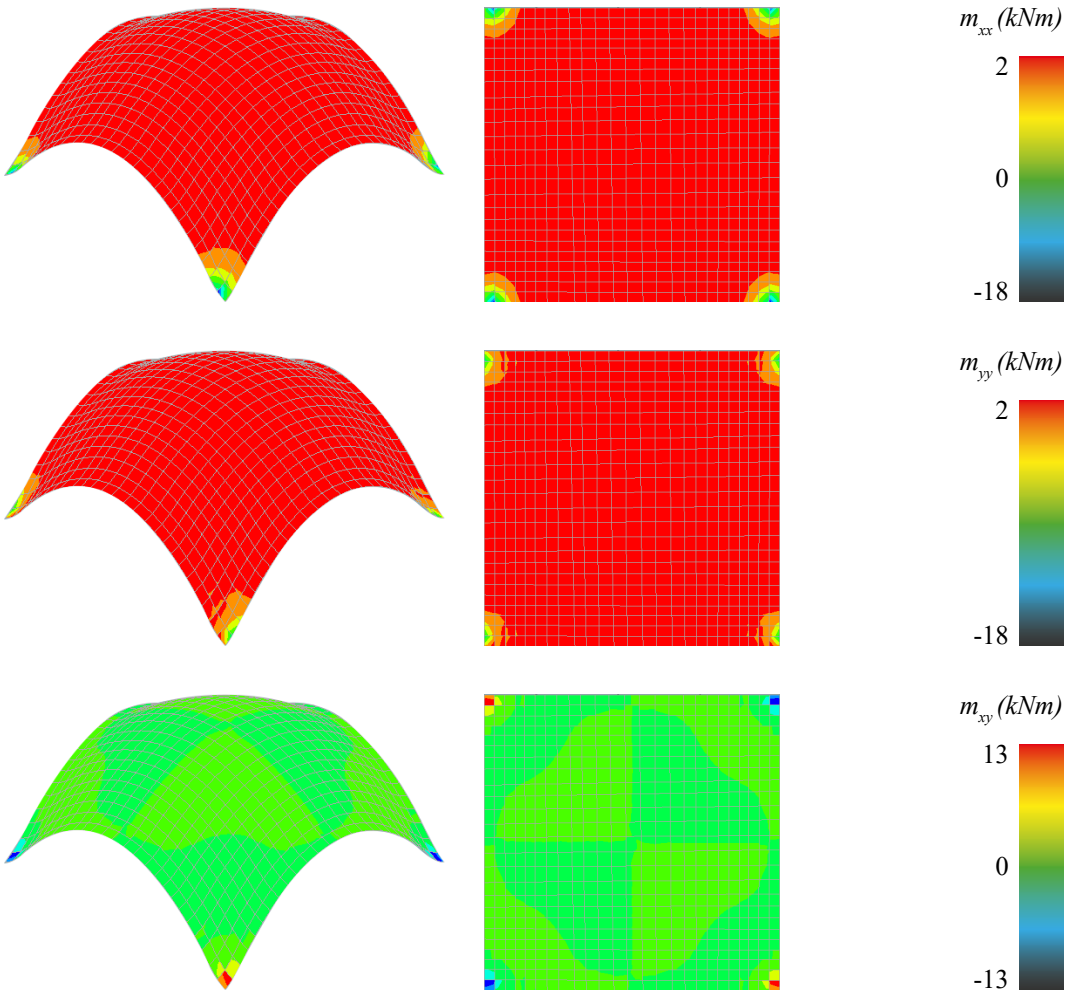

Figure 4.26: m_{xx} (a), m_{yy} (b) and m_{xy} (c) of a shell surface from $\bar{M}$-hill flat twistless plate with no rotation around the edges

narrower colour scale is given in Figure 4.27. Evaluation of the results lets us conclude that bending moments do occur, especially towards the supports. At the same time, however, it can be observed that the middle part of the surface is nearly free of bending moments. This part poses almost maximal shell-like behaviour. Apart from the localised peaks at the supports, it can be concluded that this shape behaves highly as a shell structure, under the given boundary conditions. If we changed any of these boundary conditions, clearly, the results could be entirely different. In search of any shell surface it is therefore essential to determine the boundary conditions, and establish which conditions form analogies with their projected counterparts. In order to adjust the shape of the shell for the localised bending moments to decrease, we should study how to further improve its shape.

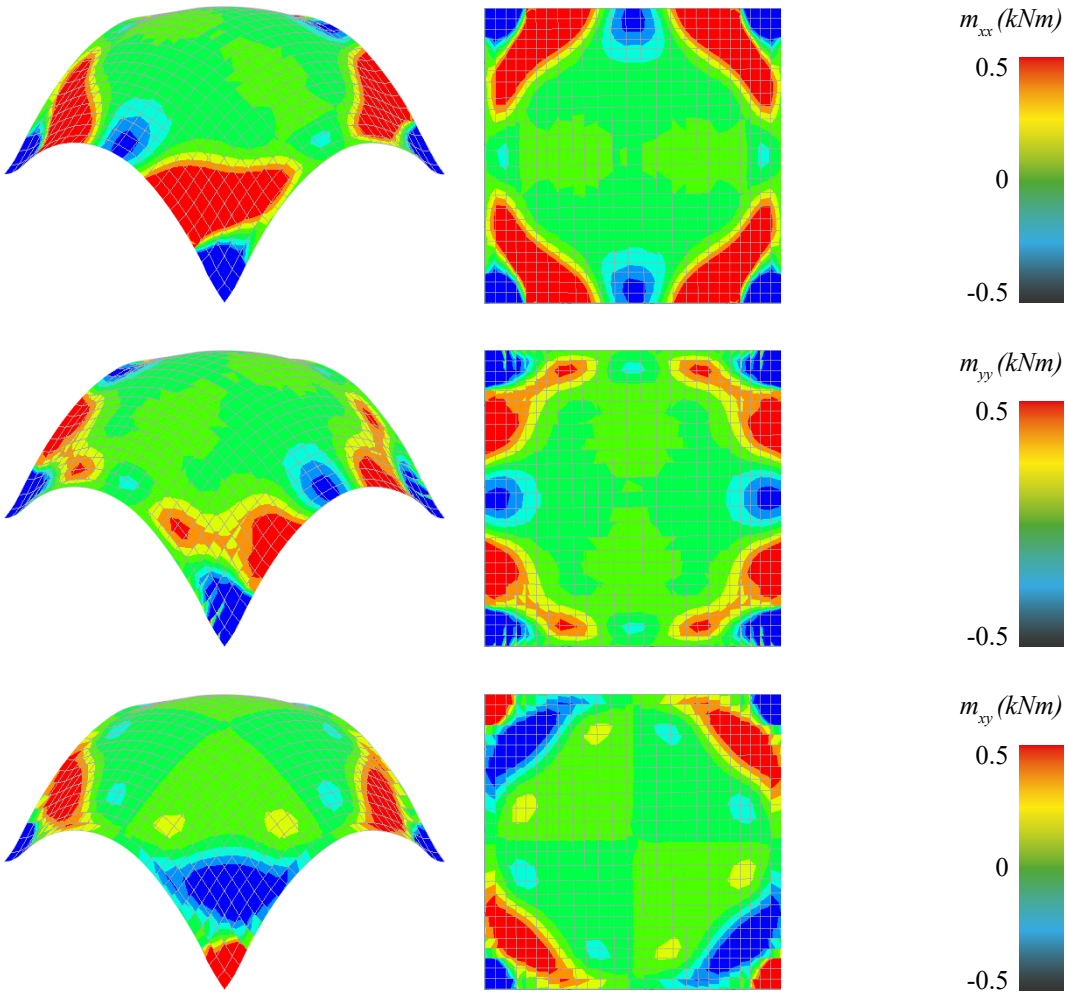

Figure 4.27: m_{xx} (a), m_{yy} (b) and m_{xy} (c) of a shell surface from $\bar{M}$-hill flat twistless plate with no rotation around the edges, with narrower colour scale

4.3 CIRCULAR

4.3.1 SIMPLY-SUPPORTED CIRCULAR PLATE

A circular isotropic plate with constant thickness is taken and subjected to an axial symmetric load. In this plate, all pie slices are identical, so all units are a function of the radial distance r $[m]$ and not of the angle φ $[rad]$. The sum of moments $\bar{M}$ is governed by the radial m_{rr} and tangential bending moments $m_{\theta\theta}$ ([4.6]). No shear stress $n_{r\theta}$ can occur (Blaauwendraad, 2010), and therefore no shear moments $m_{r\theta}$, since they cancel each other out.

$$\bar{M} = m_{rr} + m_{\theta\theta} \qquad [4.6]$$

Bending moments m_{rr} and $m_{\theta\theta}$ are calculated through respectively [4.7] and [4.8] (Hoogenboom, 2008).

$$m_{rr} = \frac{p}{16}(3+v)(a^2 - r^2) \qquad [4.7]$$

$$m_{\theta\theta} = \frac{p}{16}\left(a^2(3+v) - v^2(1+3v)\right) \qquad [4.8]$$

However, we assume a plate with Poisson's ratio $v = 0$, so that bending moments m_{rr} and $m_{\theta\theta}$ are calculated through [4.8] and [4.9].

$$m_{rr} = \frac{3p}{16}(a^2 - r^2) \qquad [4.9]$$

$$m_{\theta\theta} = \frac{p}{16}(3a^2 - r^2) \qquad [4.10]$$

Substituting [4.8] and [4.9] into [4.7] gives us the formula for the $\bar{M}$-hill ([4.11]).

$$z = \frac{p}{4}(a^2 - r^2) \qquad [4.11]$$

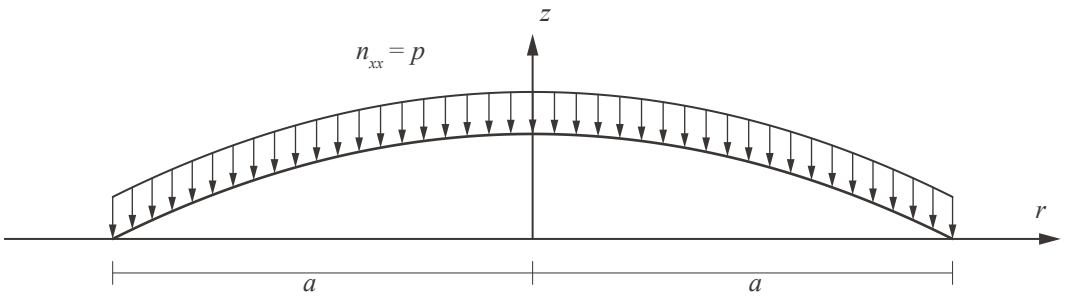

Figure 4.28: Section of $\bar{M}$-hill across circular plate

Plotting [4.11] with axes r and z results in Figure 4.28. The height of the arc is determined by the magnitude of the load p. We distinguish normal forces n_{xx} and n_{yy} as the forces acting in respectively the radial and tangential direction (Figure 4.29). Both values can be calculated through the equations in [4.12]. For $r = 0$ we can easily calculate that $n_{xx} = n_{yy} = -p$. From the equations it can also easily be observed that n_{xx} and n_{yy} share an inversely proportional relation, meaning that an increase in r results in an increase in n_{xx} and a decrease in n_{yy}, and vice versa. This is logical since n_{xx} and n_{yy} are always perpendicular to each other.

When we draw a section across the centre of the distributed force, we get an image like Figure 4.32. The normal forces n_{xx} acting through the rings are taken up at the support by $n_{yy;h}$. The magnitude of $n_{yy;h}$ in each point along the edge is given by decomposing the force vector perpendicular to that edge into a vector for $n_{yy;h}$ in the direction of n_{xx} and one perpendicular. Thus a distribution of $n_{yy;h}$ as given in Figure 4.30 is the result.

$$n_{xx} = -p\frac{\sqrt{r^2+4}}{2}$$

$$n_{yy} = -p\frac{2}{\sqrt{r^2+4}} \qquad [4.12]$$

$$\lim_{r\to 0}\left(\sqrt{r^2+4}\right) = 2$$

$$n_{xx} = -p \qquad for\ r = 0$$

$$n_{yy} = -p \qquad for\ r = 0$$

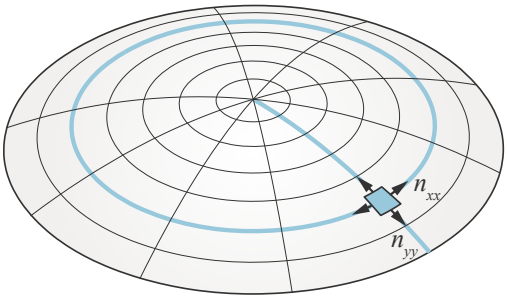

Figure 4.29: Normal forces in local xx- and yy-direction

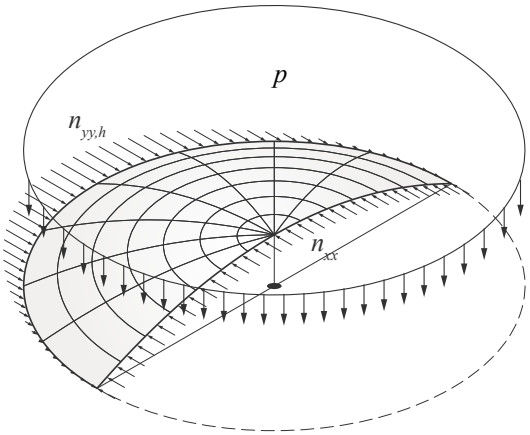

Figure 4.30: Section through the distributed force p

Do note that if we were to create a section perpendicular to this one, we would get a similar image but with the vectors rotated 90 degrees.

Now, when we take that same section, and imagine it in a two-dimensional diagram, it should be noted that the distributed force acting on the section edge is basically two pie parts. This ultimately results in the formula for a dome, which is a function to the power of three [4.13].

$$z = -\frac{1}{6a}x^3 + \frac{1}{6}a^2 \qquad [4.13]$$

4.3.2 SHELL EQUIVALENT

Using the formula from [4.12], we can generate the section curve of a dome. This is done in modelling software Rhinoceros using the plug-in Grasshopper. The section curve is then revolved around its symmetry axis, so that an axially symmetric dome is created (Figure 4.31). Again, it is important that we verify the shell behaviour of the structure, and observe if the bending moments are minimised.

Consider the shell-like dome in Figure 4.31. The dome is subjected to a projected load p. For the analysis, the following properties are assigned. An analysis is executed in DIANA FEA.

$a = r =$	$5\ m$
$p =$	$-1\ kN/m2$
$t =$	$0.1\ m$
$\lambda =$	$0.5\ m$
$v =$	0

The results of the analysis are visualised in Figure 4.32. From the evenly coloured ring it looks like the shell shows very shell-like behaviour. Judging from the lower and upper bounds of the bending moments, it can be concluded that nearly no bending moments occur. We do, however, observe higher bending moments in the centre of the dome.

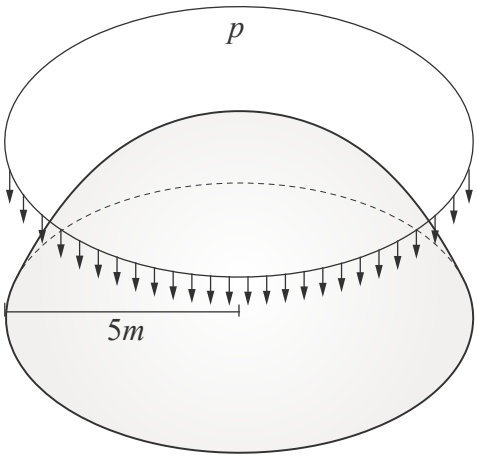

Figure 4.31: Analysis case dome

This can be a result of the highly analytical character of the equations used for the creation of the dome shape.

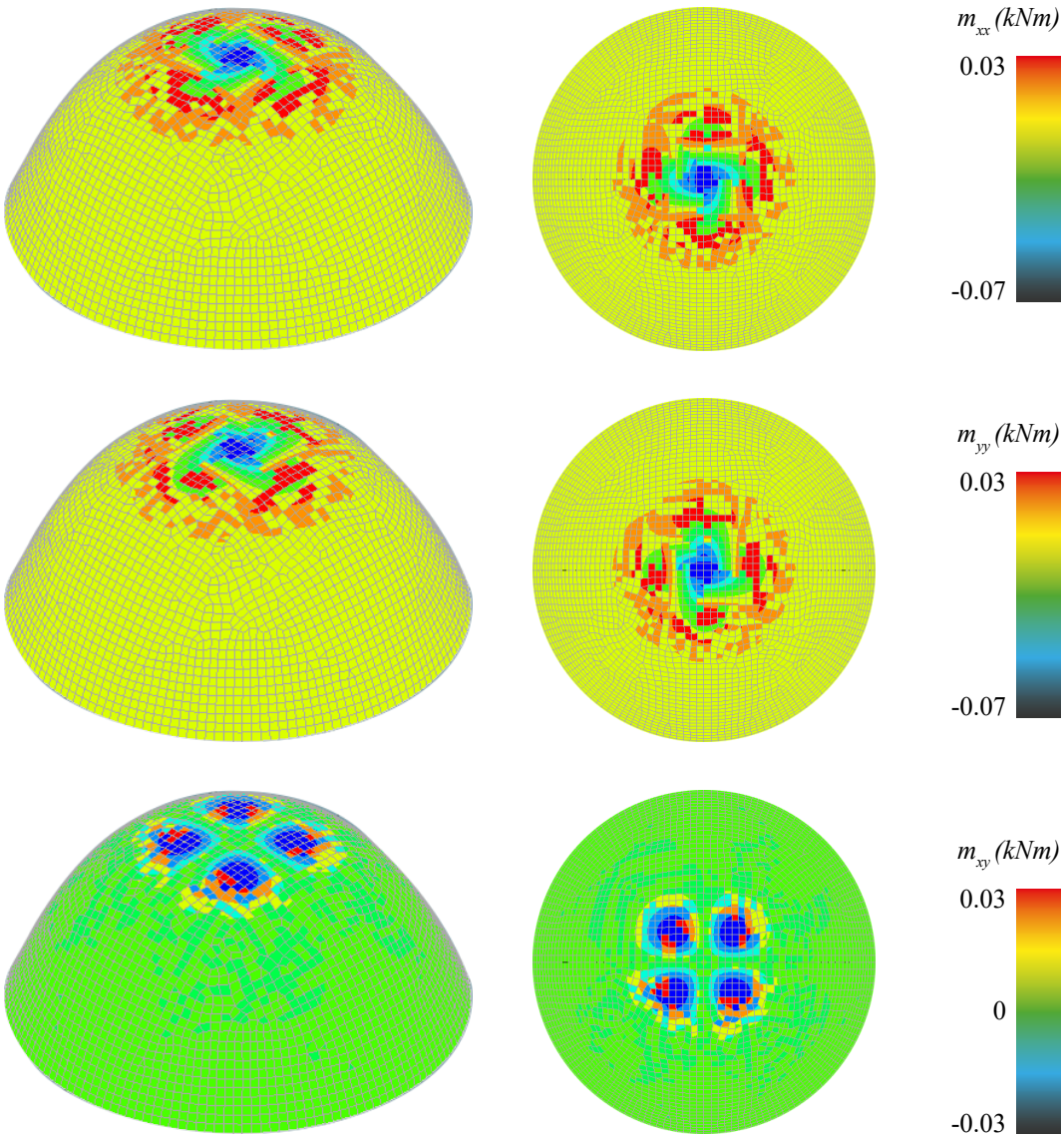

Figure 4.32: m_{xx} (a), m_{yy} (b) and m_{xy} (c) of a shell surface from $\bar{M}$-hill flat circular plate

4.4 CONCLUSIONS

In *1.4.2*, a hypothesis was stated as follows: *'An analogy is present between (1) the geometry of a moment hill of a plate and (2) the thrust surface of a shell subjected to a distributed load, and their boundary conditions are mutually related.'*. In this chapter, this hypothesis was extensively assessed. We looked at different plate geometries and different boundary conditions, continuously evaluating their potential shell behaviour. In this process, an attempt was made to connect two-dimensional cases to three-dimensional shell equivalents, also with respect to their edge properties and presence (or absence) of torsional moments.

First, a square plate on four supports was used to generate the $\bar{M}$-hill. Its $\bar{M}$-hill proved not to show optimal shell-like behaviour when supported on four corners. Drawing its rainflow diagram helped in understanding the force flows through the structure, and directed towards a review of the edge conditions. Changing the support case from corner supports to semi-rigid edge supports resulted in better shell behaviour. An analogy between the bending moments m in a flat plate and the normal forces n in its shell equivalent was proposed. It was, however, identified that the torsional moments m_{xy} in the plate influenced the reduced sum of bending moments $\bar{M}$. In order to create an $\bar{M}$-hill in which m_{xx} and m_{yy} operated as separate systems, the twistless case was introduced. The $\bar{M}$-hill created from a twistless plate, supported on semi-rigid edges, proved to behave most shell-like of the analysed cases.

These findings provided the foundation for the subsequent research. Here, it was attempted to create a square shell structure on four supports. Developing its plate equivalent was initiated again with help of the rainflow analogy. Since the normal forces were to be directed to the four supports, this should be reflected in the rainflow diagram. Such a diagram was found in the case of a continuous floor on four columns, giving a rotation φ of zero, but allowing for displacement in the z-direction. By setting these properties and making the plate twistless, a moment hill was created that showed almost no bending moments when subjected to a projected load.

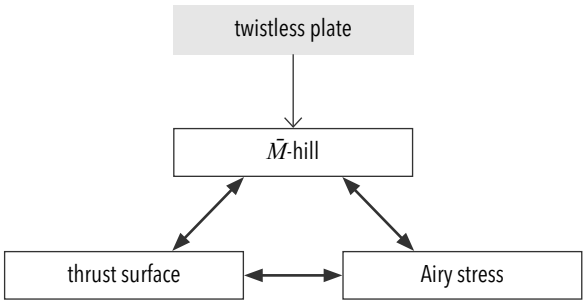

Figure 4.33: Relationship between the $\tilde{M}$-hill, Airy stress function, and thrust surface of a twistless plate

Finally, the shape of a funicular dome was analytically described. This shape appeared not to be the $\tilde{M}$-hill directly, but could be described by a function to the power of three. Again, the analogy with the horizontal projection was given.

A number of analogies between two-dimensional geometries and their three-dimensional equivalents have been proposed. Additionally, the reciprocal relation between the Airy stress function and the force diagram (thrust surface) has been explained earlier. Since the thrust surface is considered the optimal geometry for force transfer, we could use this relation to assess shell behaviour of a surface. We can then generate a shell from its analogous plate, and generate its force diagram. By comparing the force diagram and the shell surface, we can give insight in shape defects of the shell and thus help the designer improve the shape (Figure 4.34). In **Chapter 5**, a proposal for a parametric tool is given that exploits this relationship.

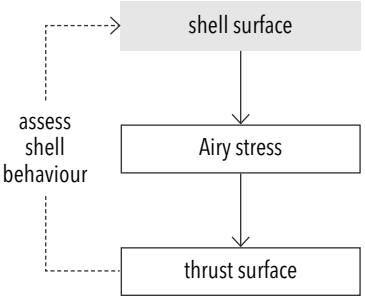

Figure 4.34: Process of assessing shell behaviour in a shell-like surface

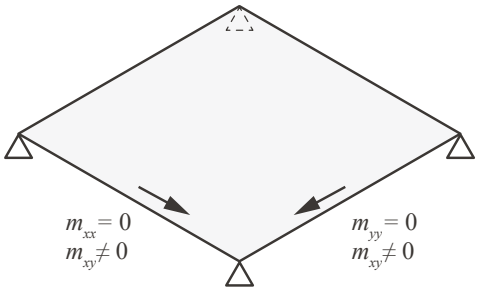

Simply-supported plate (twistless)

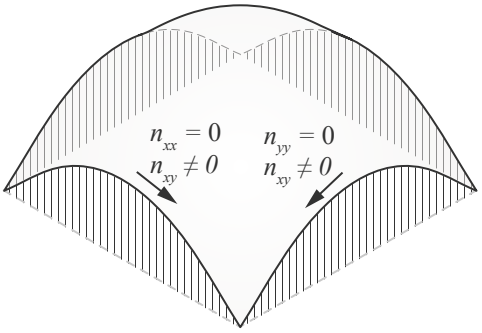

Shell on semi-rigid edge supports

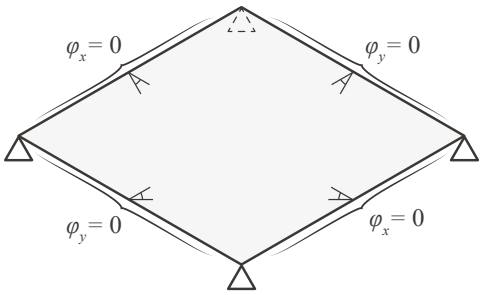

Simply-supported plate (twistless & no rotation)

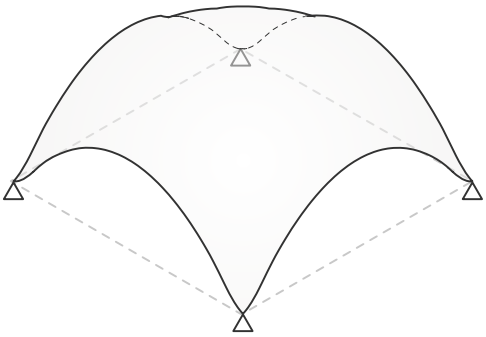

Simply-supported shell

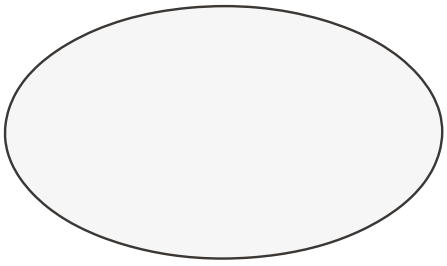

Simply-supported circular plate

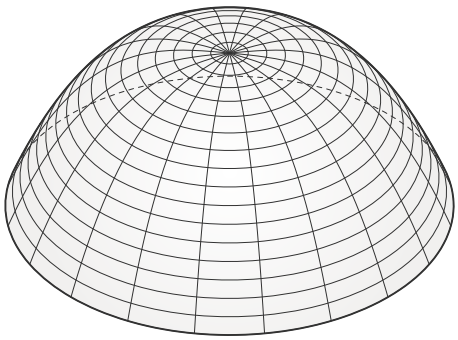

Funicular dome

Figure 4.35: Suggested analogies between flat plate geometries and their shell equivalents

5. PARAMETRIC DESIGN TOOL

5 PARAMETRIC DESIGN TOOL

5.1 TOOL RECIPROCAL FIGURES

4.4 proposes two diagrams relating shell surface, thrust plane and $\bar{M}$-hill with each other. The first diagram describes a shell surface generated from a planar surface, which in theory acts solely in compression and only takes up in-plane membrane forces. This shell geometry is therefore expected to have a thrust surface of which the geometry is the same. We can consider this geometry to behave as an S-surface from Calladine as described in *3.2*.

The second diagram describes how a shell can be assessed for its shell behaviour by calculating the volumetric difference between the shell geometry and its thrust surface. Here the ratio between the S-surface and the B-surface gives us an indication of the degree of shell-like behaviour.

To prove the analogy above, we can make use of the Airy stress function as described in *3.5.3*. After all, the Airy stress polyhedron is explained to be the reciprocal figure of the diagram of forces as early as 1870 (Maxwell). The diagram of forces can be considered a thrust polyhedron in the sense that each line only shows in-plane mechanical behaviour.

A previous graduate of the University of Technology Delft, Riemens (2015), was able to compute the Airy stress function, with which a surface could be created by populating their values on their x- and y-coordinates. The tool he developed will be used to generate the input Airy stress function for the parametric tools.

In this chapter, three parametric tools are proposed, each of which make use of the reciprocal figure. The tools allow for both design and structural analysis of shell structures.

5.1.1 PARAMETERS

In *4.4*, two uses of the reciprocal figure were proposed. Either we take a shell body of which we know that it presents in-plane mechanical behaviour exclusively. By generating its Airy stress function, we get a polyhedron to build the diagram of forces from. This diagram of forces then gives us insight into the load paths of the geometry. Or, we take a shell body of which we know that it presents out-of-plane behaviour as well as in-plane behaviour. With the help of the reciprocal diagram, we can build its diagram of forces (thrust surface). This not only gives insight in the funicular form, but also shows where deficiencies occur in the initial shape. After all, if the shell geometry and the S-component are known, the B-component can be determined.

In both cases a three-dimensional surface, the shell geometry, serves as input for the parametric tool. The tool of Riemens (2015) allows us to generate an Airy stress point cloud that will be used further.

Additionally, a meshing size can be input, determining the size of the force density mesh and ultimately the accuracy of the reciprocal figure.

5.1.2 METHODOLOGY

The tool can be divided into five parts, structured as follows:

1. **Meshing and sorting:** Creating planar mesh from point cloud
2. **Creating reciprocal planes:** Creating dual planes from new mesh vertices
3. **Intersecting planes:** Intersecting planes for each ring
4. **Intersecting rings:** Intersecting across levels and joining new polyhedron
5. **Calculating force values:** Calculating normal force values from dual angles

1. Meshing and sorting

The tool uses a point cloud of the Airy stress values as input. In order to consider this a polyhedron, the points must be adjusted in such a way that they form planar faces. To achieve this, the points are used as vertices for a triangulated mesh. The edges of this mesh will later form a dual relation with the edges of the reciprocal polyhedron. The mesh size must be equal to the mesh size of the starting surface. The mesh size should be chosen carefully; an overly coarse mesh results in an inaccurate reciprocal figure, an overly fine mesh results in high computing times.

The valency of the mesh vertices corresponds with the number of edges of the reciprocal diagram. It is therefore essential to use an axially symmetric triangular mesh if we are building an axially symmetric reciprocal diagram. The central vertex in this mesh has a valency of eight, since all surrounding branches meet there. Its reciprocal surface therefore is an octagon. All surrounding vertices have a valency of six, of which the reciprocal surfaces are hexagons. The vertices on the edges have a valency of four (Figure 5.1a). The corner vertices have a valency of three. Let us call the Airy stress mesh *Polyhedron A* from here, and its reciprocal diagram *Polyhedron B*.

In order to create Polyhedron B correctly, all vertices of Polyhedron A need to be sorted. The central vertex must be located where the x- and y-axes meet ($\alpha = \beta = \gamma = 0$). That vertex will have a horizontal dual surface in Polyhedron B. The adjacent ring of vertices will be reciprocal to the ring of surfaces around the middle surface, and should therefore be considered next. In essence, we work from the centre outwards, so the vertices A (V_A) should be sorted like this (Figure 5.6b).

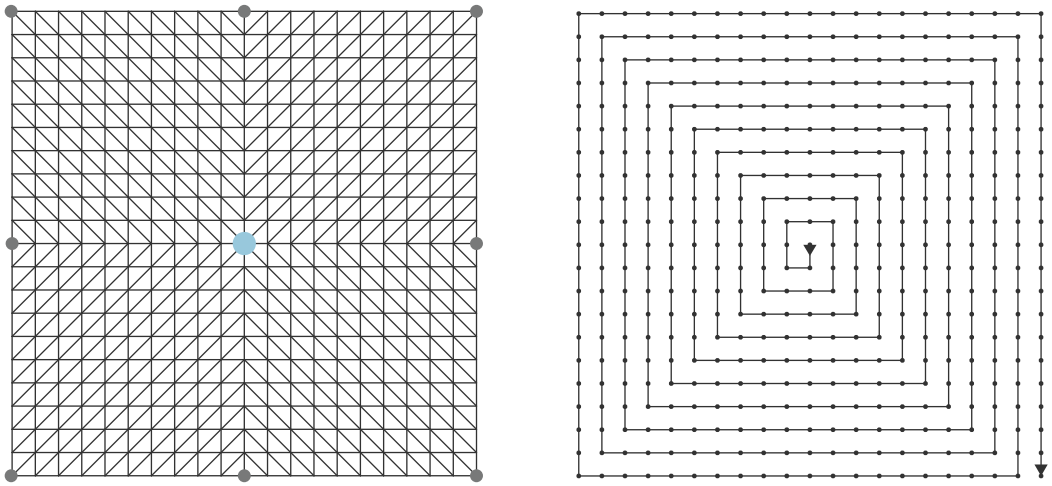

Figure 5.1: Meshing principle and corresponding vertex valencies (left), and vertices V_A sorting order (right)

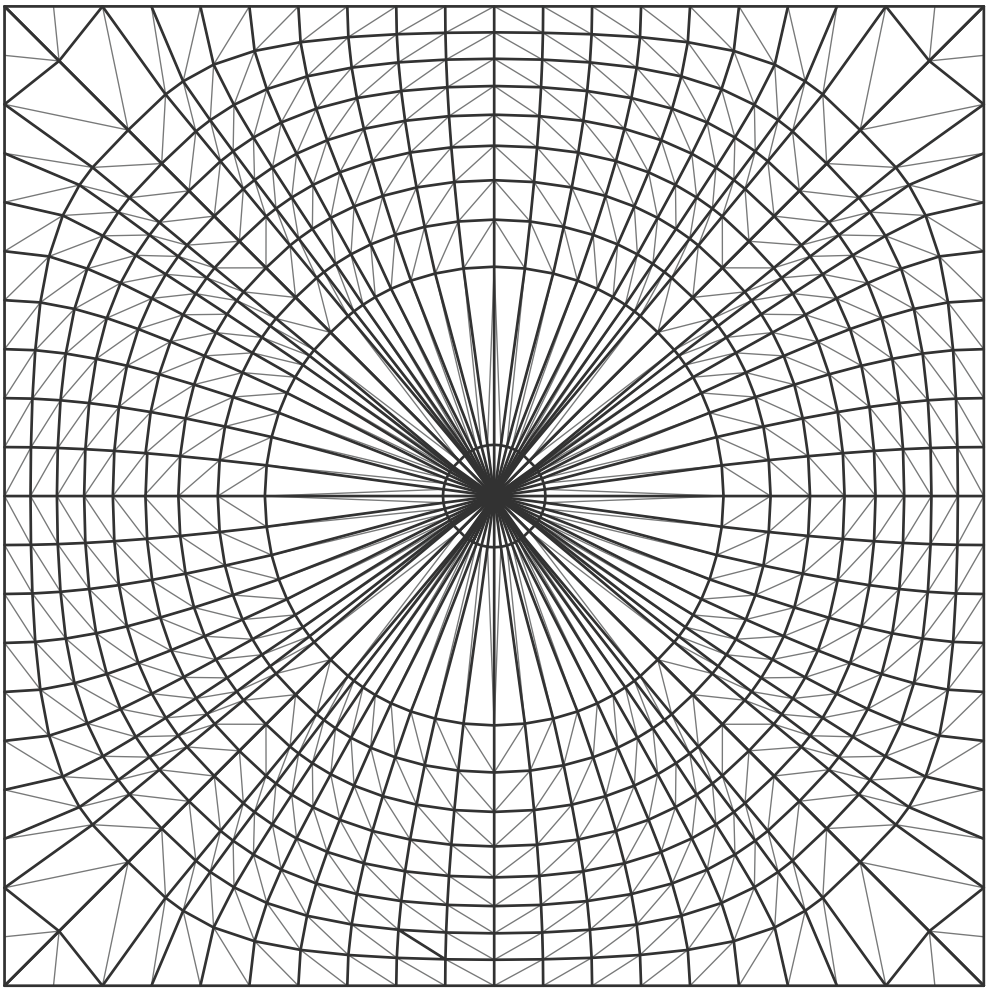

Figure 5.2: Meshing principle following rainflow trajectories and contours

In the example, a rectangular meshing grid is assumed. Since the Airy stress mesh is a discretisation of the actual Airy stress surface, this could lead to inaccuracies later on. So in many cases the possibility to alter the mesh size is desired. This poses the ability to manipulate the edges of the thrust network through which the normal forces are directed.

Considering that, many different types of meshes could be desired. For instance, it could be sensible to create a mesh from the rainflow trajectories i.e. the steepest lines, and contour trajectories i.e. the horizontal lines, so that the normal forces in the reciprocal force diagram are parallel to the minimum and maximum shear force lines. The only requirement of the Airy stress mesh is that all surfaces are planar. Figure 5.2 shows this meshing principle executed for this example.

2. Creating reciprocal planes:

Each vertex from the starting mesh contains three values: the x-, y-, and z-coordinates. The x- and y-coordinates are based on the dimensions of the surface and its meshing size. The z-coordinates are values calculated by the shell calculation component of Riemens (2015). Naturally, a different source for these Airy stress values can be used equally. It should be noted that the magnitude of the z-values is arbitrary; the optimal magnitude for the thrust surface is determined at a later stage.

As explained in *3.5*, the vertices from Polyhedron A correspond to the faces of Polyhedron B, and vice versa. The intersection edges of the B-faces in turn correspond with the connection lines of the A-vertices, and vice versa. These dual edges are always perpendicular to one another. The dual relations follow the principles of a three-dimensional Poncelet duality (Konstantatou & McRobie, 2016) (Figure 3.19).

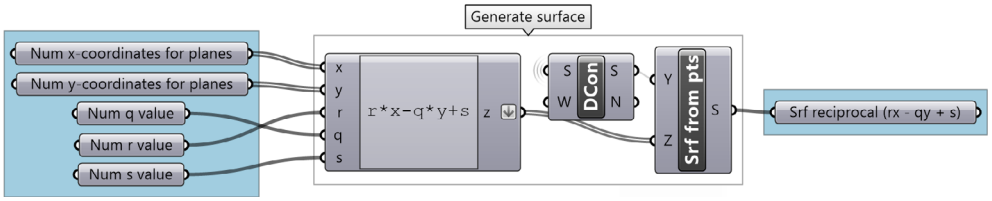

Figure 5.3: Grasshopper workflow of generating faces F_B from vertices V_A

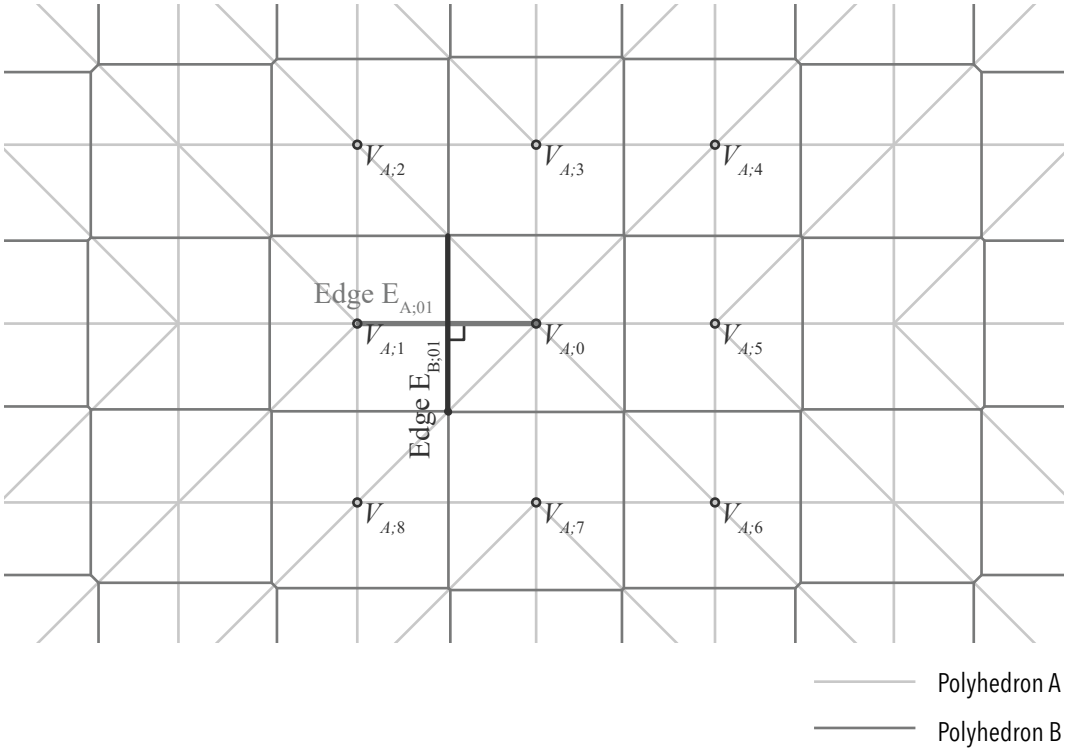

Figure 5.4: Duality between Polyhedron A and Polyhedron B

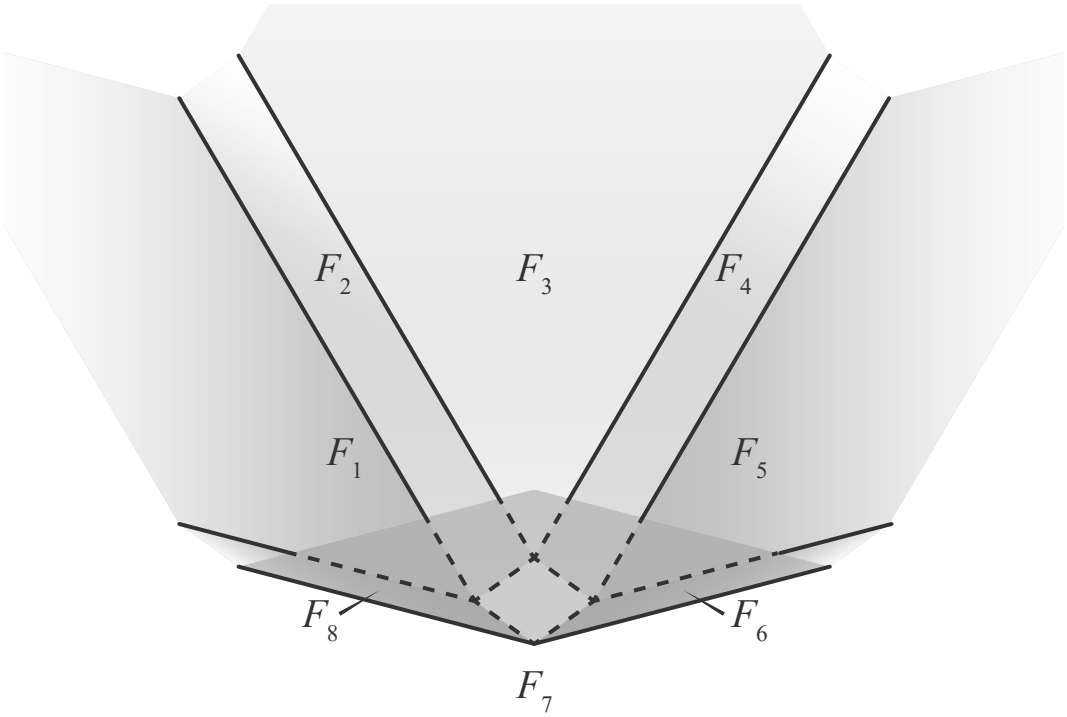

Figure 5.5: First ring of reciprocal faces and each intersection edge

This knowledge will be useful in a later stage, when we calculate the force values in Polyhedron B.

The coordinates of the vertices A (q, r, s) are used to generate planes of polyhedron B through [3.40]: $rx - qy + s$. Since a 3D-environment such as Rhinoceros cannot calculate intersection events of infinite planes, these planes are conceived as surface geometries. To achieve this, four corner points are created with the formula from [3.40], through which a rectangular planar surface is drawn (Figure 5.3). See *Appendix B1* for the complete component.

3. Intersecting planes

As a result, there are now as many faces F_B as there are vertices V_A. Initially, we search for intersecting events between faces from adjacent vertices V_A. Doing so enables us to create individual reciprocal polyhedrons for each ring. To draw a polyhedron of ring 1 for instance, we are looking for intersection events between V_1 and V_2, V_2 and V_3, and so forth up until V_8 and V_1. This results in a polyhedron such as Figure 5.5, yet its shape naturally depends on the values of the Airy stress function.

The duality between the polyhedrons becomes more insightful once they are visualised as a planar projection. The relationships from the Poncelet projective geometry can then all be identified. From Figure 5.4 it can easily be recognised that the valency of eight

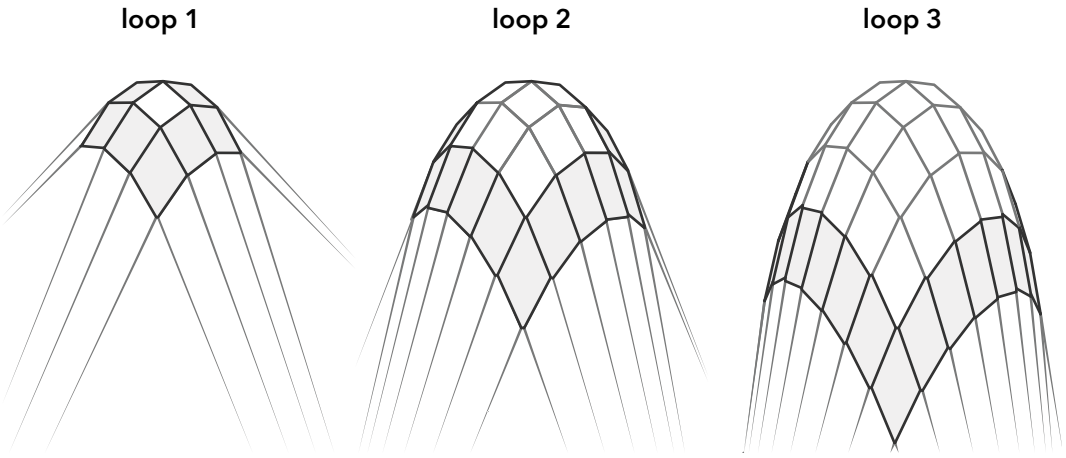

Figure 5.6: Looping operation to build reciprocal figure from the top downwards

of the middle vertex of Polyhedron A poses a dual face with eight bounding edges; it becomes an octagon. Equally, the surrounding vertices with a valency of six have dual faces with six bounding edges.

Polyhedron B is scaled to clarify the dual relations between the edges of Polyhedron A and the edges of Polyhedron B. Figure 5.4 shows edge $E_{A;01}$, drawn between vertices $V_{A;0}$ and $V_{A;1}$ and its dual edge $E_{B;01}$, drawn on the intersection of faces $F_{B;0}$ and $F_{B;1}$. Both edges are perpendicular to each other.

The feasibility of the process described above is highly dependent on the values of the input Airy stress. The difference in z-value between adjacent vertices is generally minimal at the centre for an Airy stress function of a shell structure. Intersection edges can therefore be identified easily here. However, with larger differences in Airy stress between adjacent vertices, distortions occur in the geometry of a ring. In some cases faces from non-adjacent vertices are being intersected, so that still a homogeneous polyhedron is created. Further elaboration on this will follow in *5.1.4*.

4. Intersecting rings

After successfully creating each polyhedron ring, we can look for intersection edges in the outward direction. Each ring is now considered a sum of intersecting faces, and is a *joined polysurface* in the three-dimensional environment Rhinoceros. The cross-level

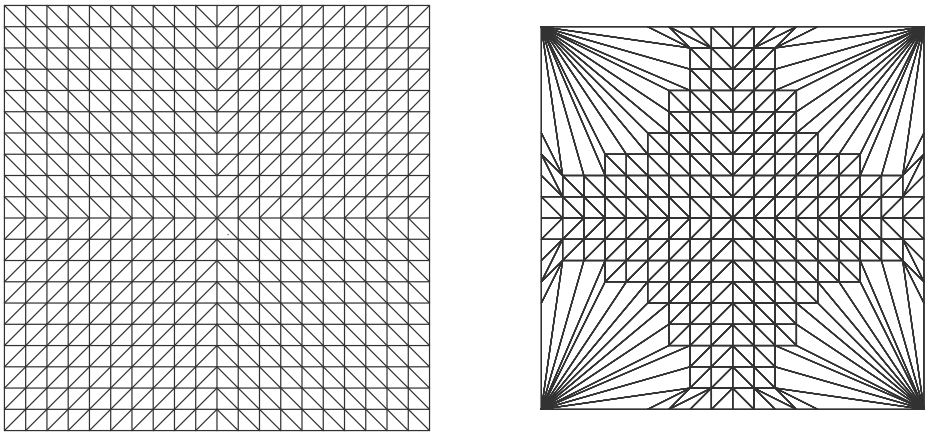

Figure 5.7: Difference in adjacencies between surfaces of Polyhedron A (left) and those of Polyhedron B (right) of the example

intersection is a process similar to that of two faces. The sum of faces of each ring is intersected with the sum of faces of the subsequent ring and then joined together. The polysurface is thus built up from the top to the bottom, adding a ring to the polysurface each cycle (Figure 5.6). Since Grasshopper does not allow for looping operations, plug-in Anemone was used. See *Appendix C* for the looping component in the script.

5. Calculating force values

The duality between the Airy stress diagram and the force diagram means that all corresponding properties are reciprocal. As a result, we can calculate the normal forces $n_{BE;i}$ in the force diagram (Polyhedron B) by determining the angle $\varphi_{AE;i}$ on the intersection edge between two surfaces in Polyhedron A. After all, the stress resultants equal the angular defect: $N_{BE;i} = \varphi_{AE;i}$ (*3.5.2*). From these stress resultants we can calculate the normal forces in the force diagram.

In order to calculate the angle between two surfaces in Polyhedron A, we must first determine each adjacency relationship of Polyhedron B. The intersection edges in Polyhedron B are namely reciprocal to $\varphi_{AE;i}$. in Polyhedron A. The trimmed surfaces of Polyhedron B, however, are no longer sorted, since they are a result of intersection events in two directions, as well as joining operations. It is therefore needed that the trimmed surfaces are again related to their dual vertices. In order to do so, each trimmed surface is compared to the planes built from the Airy stress vertices by their normal

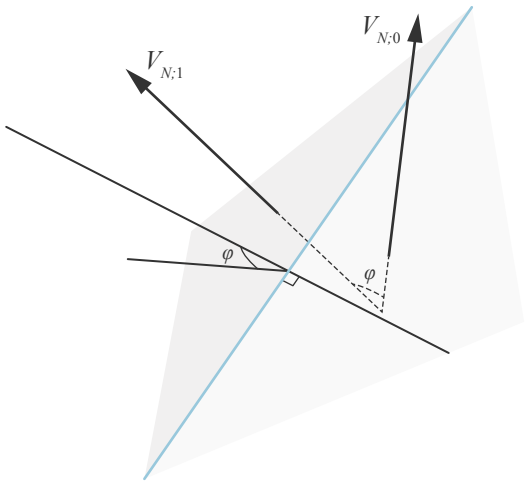

Figure 5.8: Angle between normal vectors of surfaces equals angle between surface at mutual edge

directions. If the angle between the normal of the trimmed surface and the starting plane is zero, then the related surface is found. The Grasshopper component governing this operation is attached in *Appendix C*.

Before the angles between surfaces can be calculated, we need to look at the adjacency between them. There are two ways to approach this exercise; (1) either we start with the vertices from Polyhedron A, and determine for each vertex their adjacent vertices, or (2) we start with the trimmed surfaces of Polyhedron B and determine intersection events with other surfaces. Figure 5.7 shows what this difference means for the results. In *5.1.4* the source of this difference is explained. The Grasshopper component governing this operation is attached in *Appendix D*.

Now that the relationships between surfaces are known, we can calculate their corresponding angles. We are looking for the angle perpendicular to the edge shared by both surfaces (see *3.5.3*). Determining this angle is straightforward, since it is equal to the angle between the normal vectors of the surfaces (Figure 5.8). Figure 5.8 also shows that the direction of the force is now perpendicular to the edge of Polyhedron B. This is a property of the Maxwell duality, and needs to be addressed once we process the results later. The angular defects φ from Polyhedron A equal the stress resultants N (Figure 5.9), which become normal forces n in Polyhedron B.

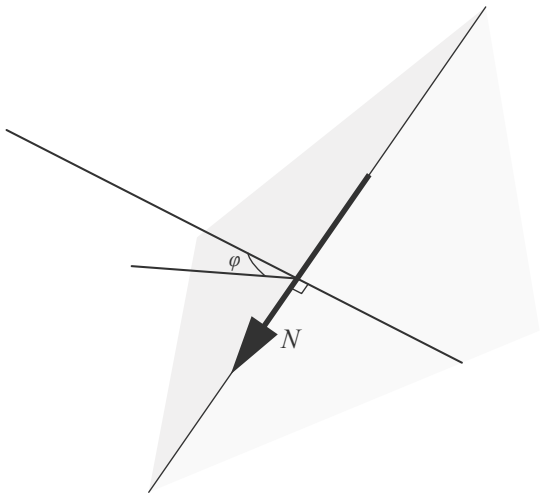

Figure 5.9: Angular defect equals the stress resultant N in Polyhedron A

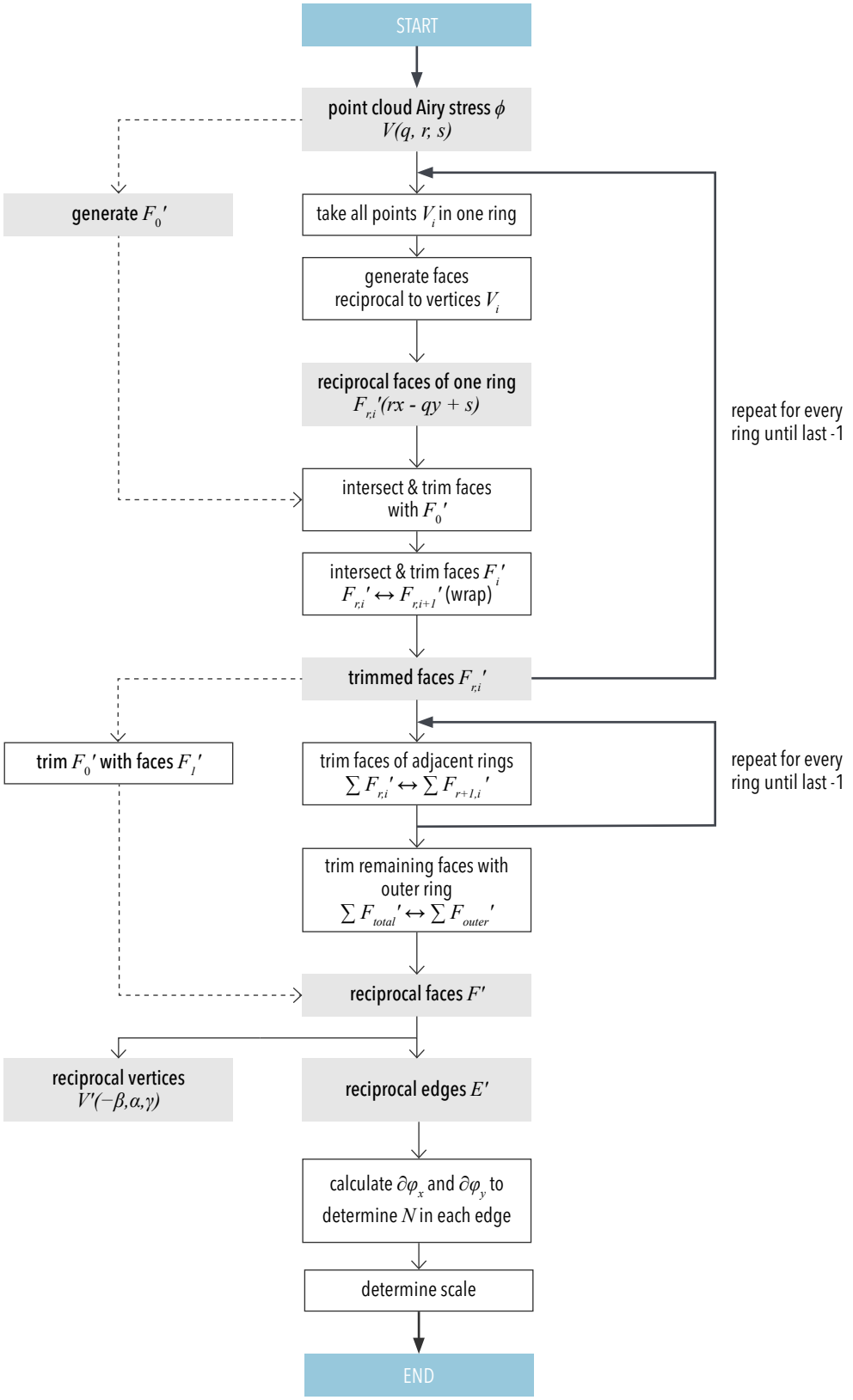

Figure 5.10: Process diagram of parametric tool to generate reciprocal polyhedron

5.1.3 RESULTS

In *5.1.2*, a parametric tool was proposed to generate the reciprocal figure (Polyhedron B) of the Airy stress mesh (Polyhedron A). This process exploits the relationship between the diagrams of form and force, already introduced by Maxwell in 1870 (Maxwell, 1870). To measure the performance of the tool, a number of different cases are now analysed and evaluated. For this, three of the $\bar{M}$-hills from **Chapter 4** are used as input. These surfaces have been analysed in terms of shell behaviour, which could help in understanding the results.

$\bar{M}$-hill square flat plate

In *4.2.2*, the $\bar{M}$-hill of a square flat plate was generated using the tool of Liang (Figure 5.11a). From this surface, we will create a force network. In order to do so, first the Airy stress surface is computed using the tool of Riemens (Figure 5.11b). The surface is converted to a triangulated mesh polyhedron. This polyhedron is then loaded into the parametric tool to generate the reciprocal polyhedron (force diagram) (Figure 5.12). The image shows the unscaled polyhedron; a steep shell-like network of lines.

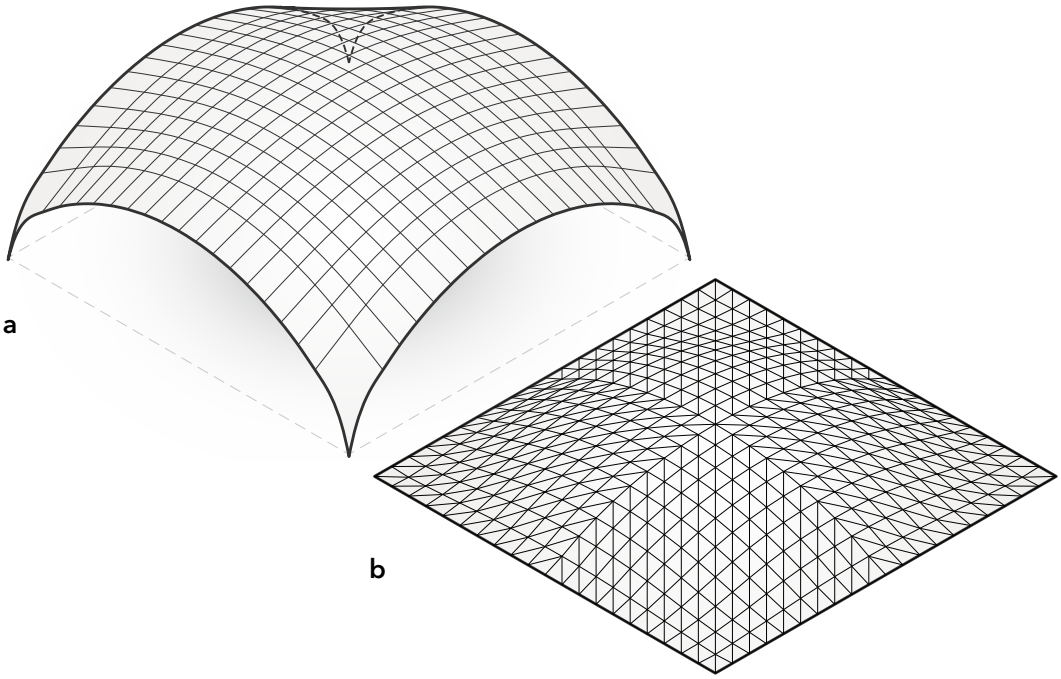

Figure 5.11: $\bar{M}$-hill square plate (a), and corresponding Airy stress mesh (b)

Evidently, the scale of the force polyhedron does not correspond with the scale of the shell surface. The scaling factor is still to be determined when calculating the force values in the edges. Interestingly, we do observe the edges of the polyhedron to form a parabola. When we project the edges onto a horizontal plane as in Figure 5.12, then we find the edges not to form straight lines. Seemingly, no compression forces occur in this area. This occurrence is explained in *5.1.4*.

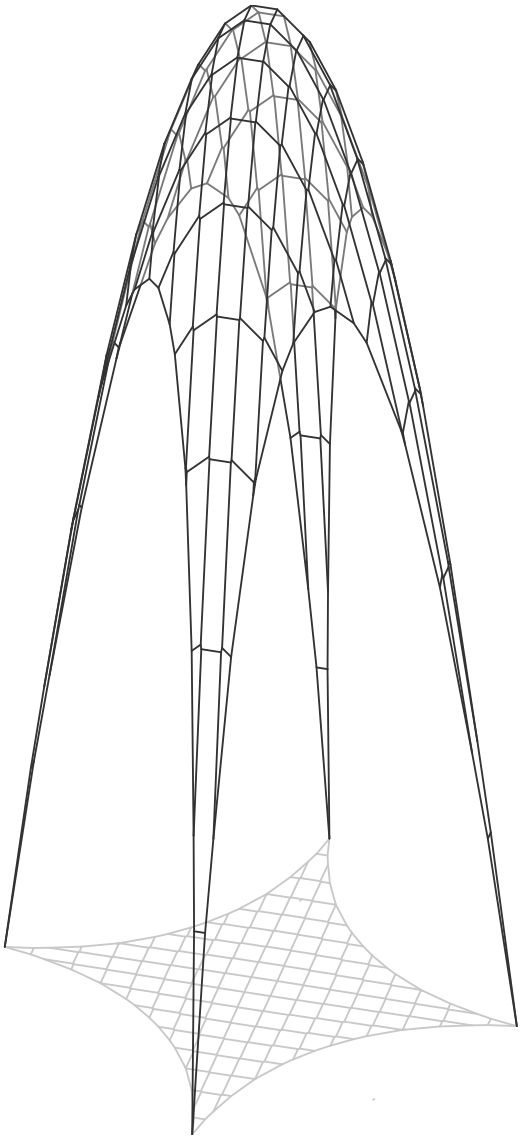

Figure 5.12: Unscaled force polyhedron from $\bar{M}$-hill square plate

$\bar{M}$-hill square flat continuous plate

A force network is created of the $\bar{M}$-hill of the continuous plate from *4.2.5*. The $\bar{M}$-hill surface is given in Figure 5.13a, and its corresponding Airy stress polyhedron is visualised in Figure 5.13b. It can clearly be observed that the Airy stress function is relatively steep compared to the previous one.

In Figure 5.14, the force polygon is shown. Since the shell was created using DIANA FEA, it is not completely symmetrical. Therefore two of the supports in the force polygon do not reach ground level. Also, only a limited number of polygons are created, meaning that the rest of the polygons would result in an uncontinuous surface. This could be the result of tension, but that should be further analysed. We can again clearly observe a parabolic shape on each side of the force polygon going towards the supports. This is different from the initial shell surface and gives input for possible improvement of the geometry.

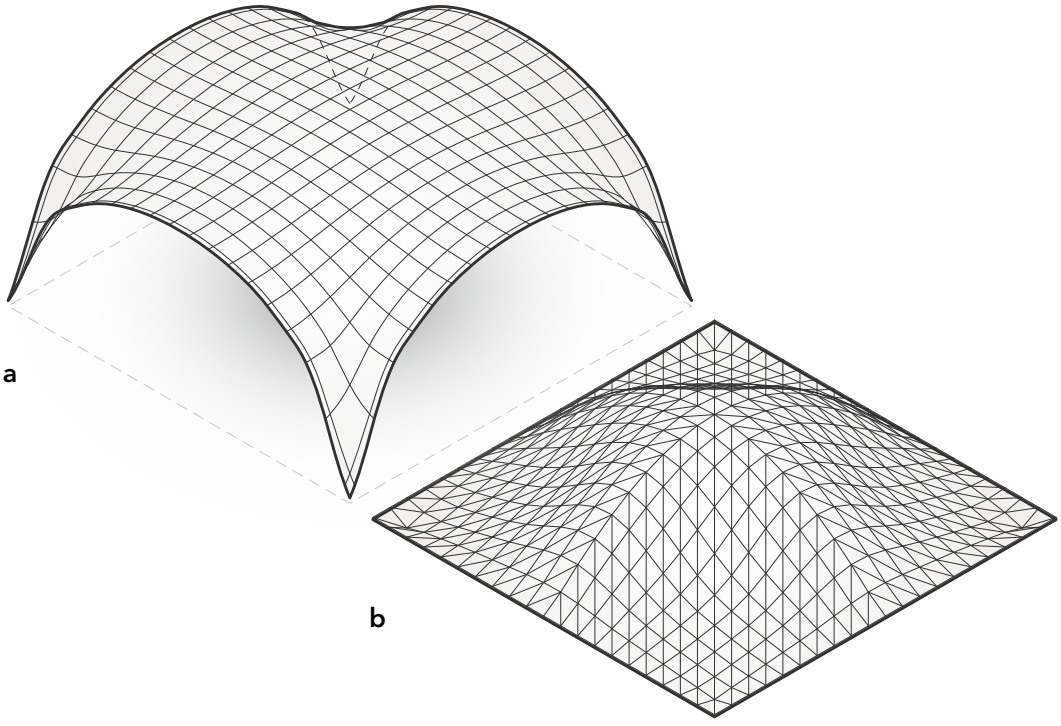

Figure 5.13: $\bar{M}$-hill square continuous plate (a), and corresponding Airy stress mesh (b)

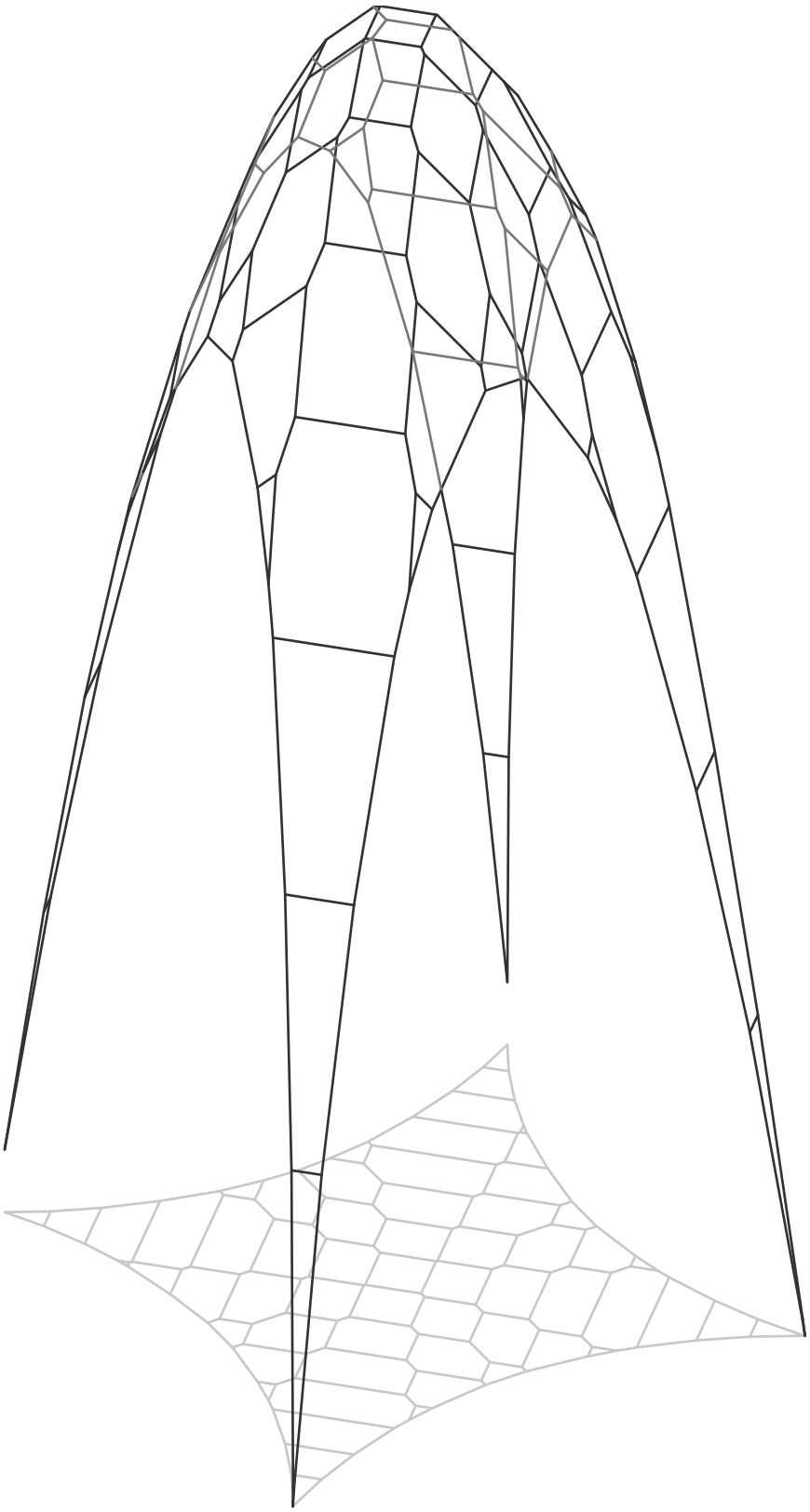

Figure 5.14: Unscaled force polyhedron from $\bar{M}$-hill square continuous plate

$\bar{M}$-hill square continuous twistless flat plate

The $\bar{M}$-hill from a square continuous twistless plate showed most shell-like behaviour of all cases analysed in **Chapter 4**. Expectedly, the geometry of this force diagram is highly similar to that of the shell surface. The reciprocal figure is generated and visualised in Figure 5.16. If we compare this image to the previous reciprocal figures, we can clearly observe the higher density of edges here. It appears that more points were converted into surfaces than in the other cases (or less surfaces were omitted).

When we look at the edges of the shell surface in Figure 5.15, the curvature is slightly anti-clastic. This is not reflected in the reciprocal figure. This could be the result of tension occuring at these edges, but could also have a different cause.

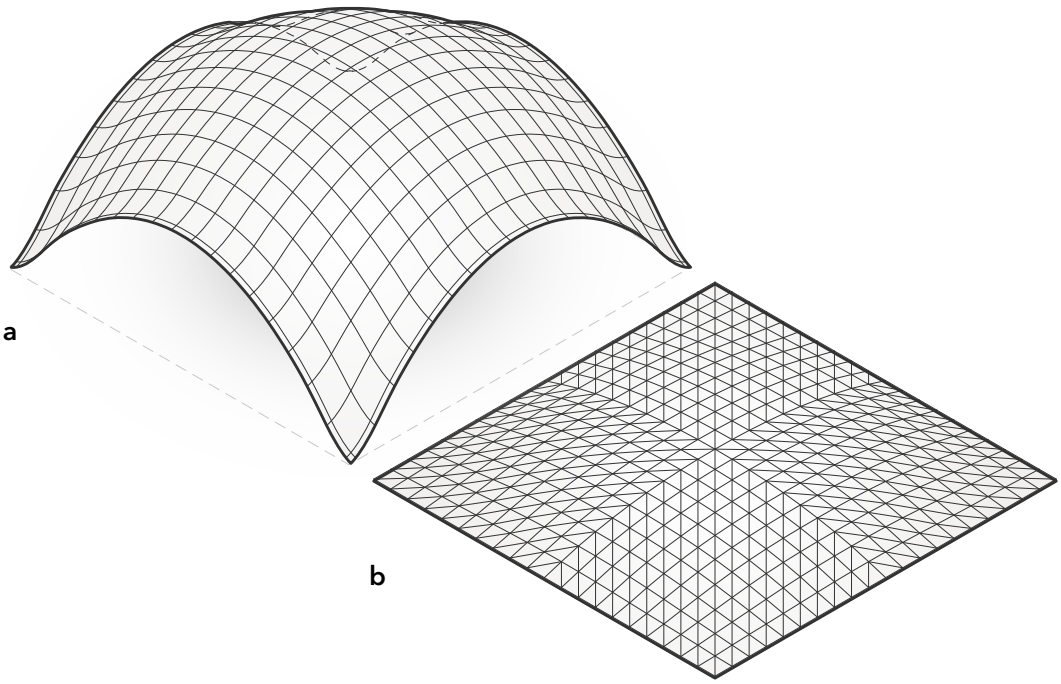

Figure 5.15: $\bar{M}$-hill square continuous twistless plate (a), and corresponding Airy stress mesh (b)

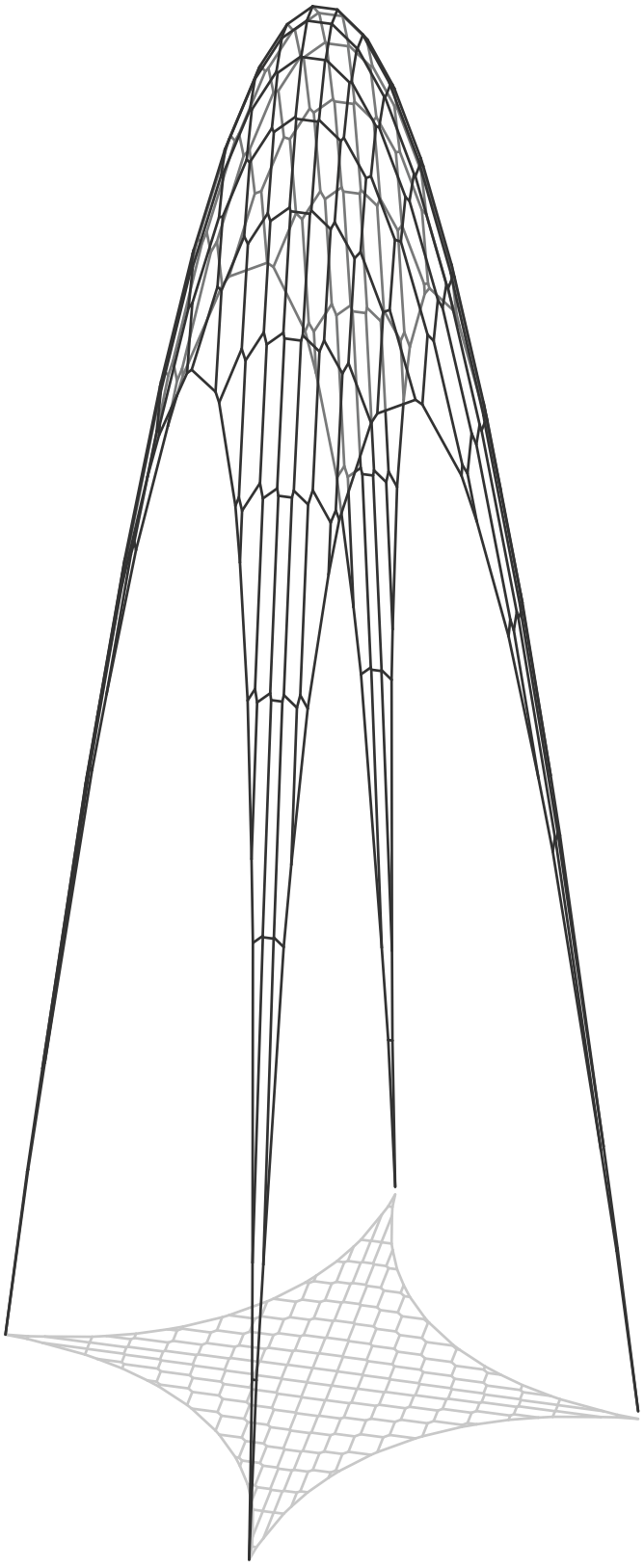

Figure 5.16: Unscaled force polygon from $\bar{M}$-hill twistless 'continuous' plate with horizontal projection

5.1.4 LIMITATIONS

Three force diagrams were created of different shell diagrams. A number of challenges became apparent in the process.

First of all, we can observe that the reciprocal figures do not have the same footprint as the initial shells. A number of the surfaces created from nodes in the Airy stress function were eliminated in the process of generating the reciprocal figure. This is a result of the loading capacity going from membrane forces (in-plane) to plate forces (out-of-plane) (Figure 5.17). Here, tension occurs, which is not supported by the reciprocal figure. In *5.2*, a different approach is taken in order to get a more comprehensive image of the thrust surface.

Secondly, the scale of the reciprocal figure is still arbitrary. If we scale it by hand, part of the geometry is really similar to the initial shell, but we cannot draw definite conclusions from this. Since this is an indeterminate structure, it is necessary to calculate the horizontal forces at the supports, and then calculate the minimum complementary energy.

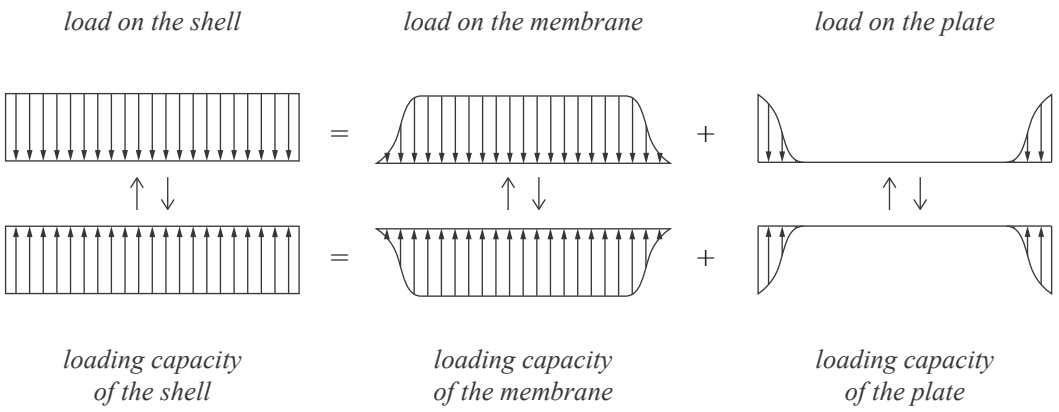

Figure 5.17: Division of loading capacity of a shell into loading capacity of the membrane and that of the plate

5.2 TOOL FORCE DIAGRAMS

In *5.1*, it was explained how the reciprocal figure of the discretised Airy stress function could be created. That reciprocal figure was then the force diagram, constructed of edges in which only compression occurred. The force diagram gave insight into the thrust surface of the initial shell structure, but was by default limited to the display of compression. In order to make the forces occurring in the structure - compression and tension - we should further analyse the results. Now, since the reciprocal figure of the Airy stress polyhedron (which is the network of stress resultants) is the force diagram, every node of the Airy stress polyhedron can be evaluated individually.

The Airy stress function is assumed to be in equilibrium (since the initial structure is also in equilibrium), so in every node of the stress function an equilibrium is also accomplished. Therefore, if we construct the force diagram (head-to-tail diagram) of every node of the Airy stress polyhedron, they should form a closed loop.

5.2.1 METHODOLOGY

To construct the head-to-tail diagram of each node of the Airy stress polyhedron, we have a vector direction i.e. the projected edge pointing towards the vertex, and a vector magnitude i.e. the angular defect. An example is given in Figure 5.18.

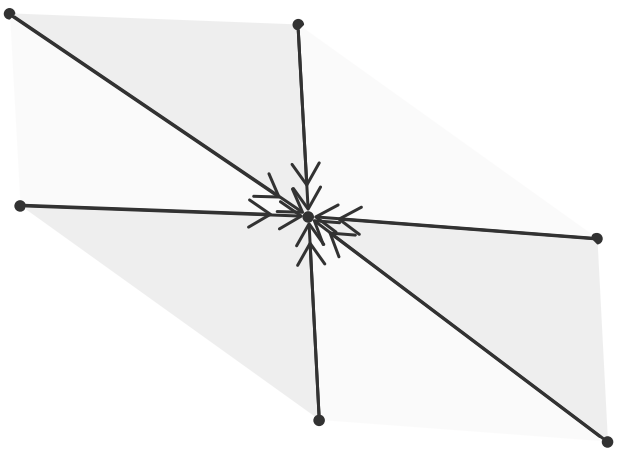

Figure 5.18: Stress resultants in the Airy stress polyhedron acting on a vertex

Angular defect

In order to construct each force polygon, we use the triangulated Airy stress polyhedron. This is a discretised version of the Airy stress function, so that the curvature is converted to an angular defect. This angular defect between two corresponding surfaces can be calculated again by calculating the angle between their normal vectors. It is essential to distinguish convex and concave angles, since the sign of the angular defect corresponds with the sign of the stress resultant. A negative (concave) angle is therefore considered a member in tension, which is a negative stress resultant (Van Mele, Lachauer, Rippman, & Block, 2012).

For every pair of surfaces between which an angle is calculated, we must first determine if it is convex or concave. This is done by drawing a line between the centre points of the surfaces, and then evaluating its position relative to the Airy stress polyhedron. Is it underneath the stress polyhedron, then the surfaces form a 'bowl', indicating that it is convex. Is it above the stress polyhedron, then the surfaces form a 'valley', indicating that it is concave. The concave angles are then multiplied by -1, so that their vector direction is flipped.

Creating the force polygon

For every vertex in the Airy stress polyhedron, there is an i amount of edges connected to it, depending on its location in the mesh. By selecting a point, each of these edges is identified, and sorted counter-clockwise. By sorting it, it is ascertained that the force polygons are drawn in the right order. Each force line consists of a front and a back (or a head and a tail), and by drawing each next force from the head of the previous one, we get a closed force polygon as a result. The angular defect in radians gives the length of the vectors, so their length corresponds with the force as it does in graphic statics.

5.2.2 RESULTS

Three examples of head-to-tail diagrams created with the parametric tool are given in Figure 5.19. They were all created from the Airy stress function from the $\bar{M}$-hill of the simply-supported rectangular plate 4.2.2. This case is known to have tension. The first example was created from a vertex near the centre of the Airy stress function. We

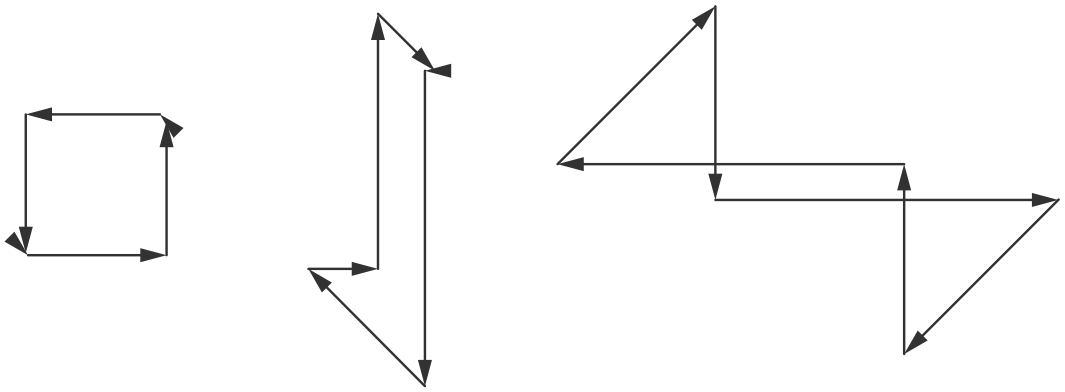

Figure 5.19: Three examples of head-to-tail diagrams created with the tool

can observe that only compression occurs in this system, since all angles are obtuse (between 90 and 180 degrees). This means that none of the vectors were flipped, so no tension is present. Later in this chapter we see that this shape is almost equal to that of the reciprocal figure created by the tool from *5.1.2*. The second example shows a combination of compression and tension. Such shapes could not be formed by the tool for reciprocal figures. This is the same for the third example. The diagram is self-intersecting, which we cannot construct a surface from.

Creating the complete projected dual polyhedron can be done as explained before in *3.5.1* (Figure 3.22). This is easily done for vertices in which only compression takes place. We have done so for the example in Figure 5.20. From this exercise a number of conclusions can be drawn. The centre force polygon is exactly equal in size and shape as the projection of the centre face of the reciprocal figure (Polyhedron B). From the centre outward, a discrepancy in the shape and size between the force polyhedron and Polyhedron becomes visible. This could be a result of the fact that the force polygons are projected onto a horizontal plane, assuming that the 'vertical' stress resultant is actually vertical, and not perpendicular to the Airy stress surface. This occurrence should be studied further in a future research in order to better understand both diagrams. For now, it appears to be a reasonable approximation, and the differences are small.

In each force polygon, there is also a tiny gap between the head of the last vector and the tail of the first (so small that it is not visible in the figure). This means that they do not close completely and are thus not completely in equilibrium. Now, the Airy stress

function is based on a projected load that is evenly distributed across the shell surface. The force polygons, however, assume discretised stress resultants (like the process explained in Figure 3.24). The stress resultants are just an approximation of the real situation, likely causing this defect In *5.2.3*, this issue will further be analysed.

The force polygons of vertices in which tension occurs are indicated with a blue colour. Just one side is displayed, but since this is a symmetrical case, all edges have similar polygon formations. Since tension occurs in these areas, it is difficult to create a coherent force polyhedron here. At these locations, the force polygon is trimmed along a parabola-like shape.

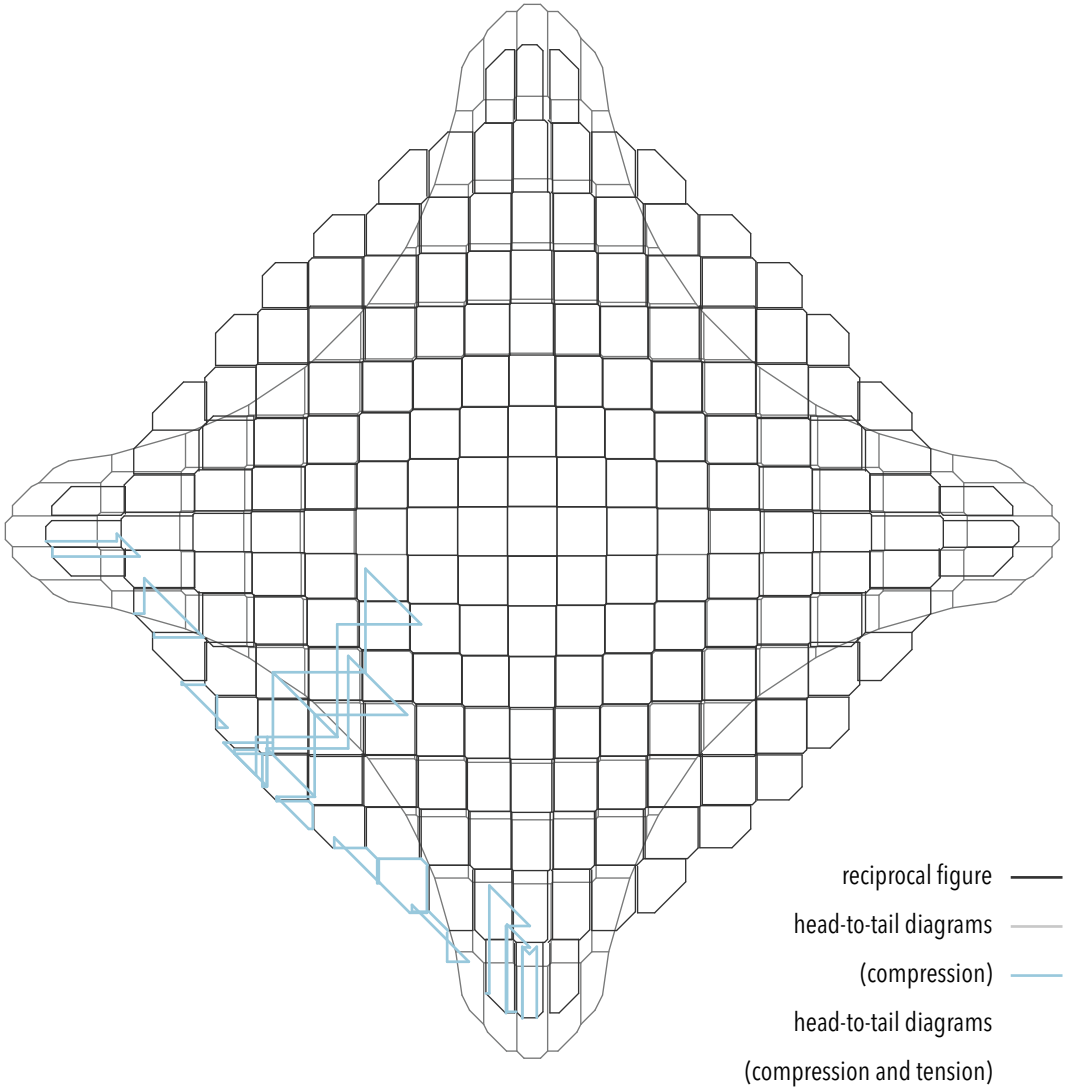

Figure 5.20: Results from the head-to-tail diagrams compared to the reciprocal figure

5.2.3 VALIDATION

In *5.2.2* it was found that the individual force polygons did not form fully closed loops. It was stated that this was possibly a result of the discretisation of the Airy stress function. In this section, a simple known case is analysed with use of the parametric tool, and the results are compared with the theory.

Consider a simply-supported beam as in Figure 5.21. The length l of the beam is $6m$ and the height is $1\ m$. It is subjected to an evenly distributed load $p = 1\ kN/m$. The general formula for the Airy stress function of a simply-supported beam subjected to a distributed load is given in [5.1] (Beranek, 1974). After introducing the values for l, h and p into [5.1], we get [5.2].

$$\phi = \frac{p}{8h^3}(l^2 - 4x^2)(2y^3 - 3hy^2 + h^3) \qquad [5.1]$$

$$\phi = \frac{1}{8}h^3\left(\frac{36 - 4x^2}{36}\right)\left(2y^3 - 3y^2 + 1\right) \qquad [5.2]$$

The Airy stress function can be plotted in an x,y,ϕ-coordinate system, which results in the Airy stress surface (Figure 5.22). The result is a smooth surface, just like the Airy stress surfaces that were generated with the tool of Riemens. We can discretise this surface by imagining a grid of 1 x 1, and triangulating that grid in order to form planar surfaces (Figure 5.23). By discretising the Airy stress surface, the continuous beam is discretised

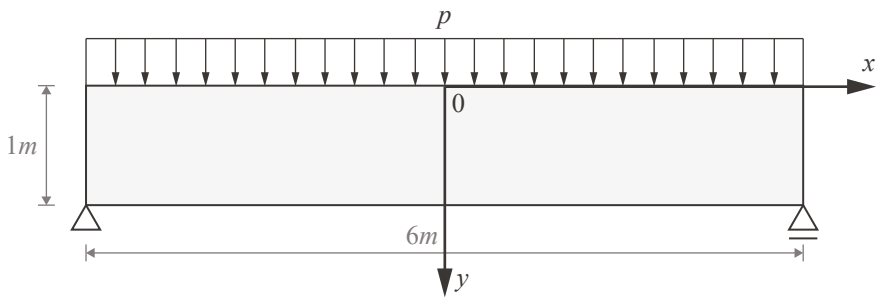

Figure 5.21: Simply supported beam subjected to a distributed load p

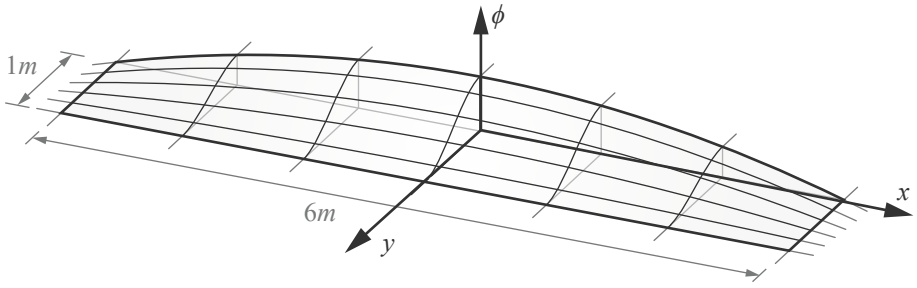

Figure 5.22: Airy stress function of a beam subjected to a distributed load (retrieved from: Beranek, 1974)

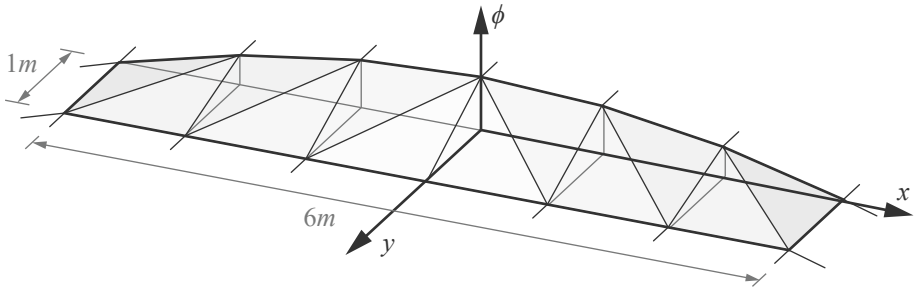

Figure 5.23: Triangulated version of the Airy stress function of a beam subjected to a distributed load

too. The beam can then be considered a lattice girder like in Figure 5.24. The distributed load p is divided into point forces F acting on each vertical bar. The division of forces is given in Figure 5.24, where the forces with a minus sign represent bars in tension, and those with a plus sign represent compression. Following *5.2.1*, the normal forces in a bar can be calculated by measuring the angle between the two corresponding surfaces in the Airy stress function.

In order to validate if the angles in the triangulated Airy stress function return the right forces, they will be calculated with the parametric tool and then compared with the distribution in the lattice girder. The surfaces out of the bounds of the beam are modelled by hand following the tangents of the initial Airy stress function. For each plane in y-direction this gives $\frac{\partial z}{\partial x} = 0$. We are able to calculate each angle corresponding with the bar forces using the tool. The results are shown in Figure 5.25.

Let us compare the results in Table 5.1. We find that for every negative (tensile) force, a positive angle is returned. This effect we shall neglect for now. For every bar, the ratio between the force N and the angle φ is calculated. The results are all similar, with a

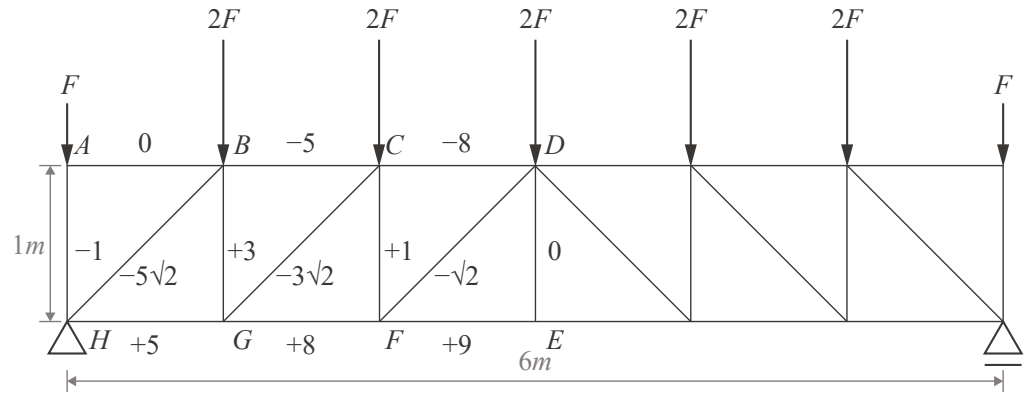

Figure 5.24: Bar forces in a lattice girder (retrieved from: Beranek, 1989)

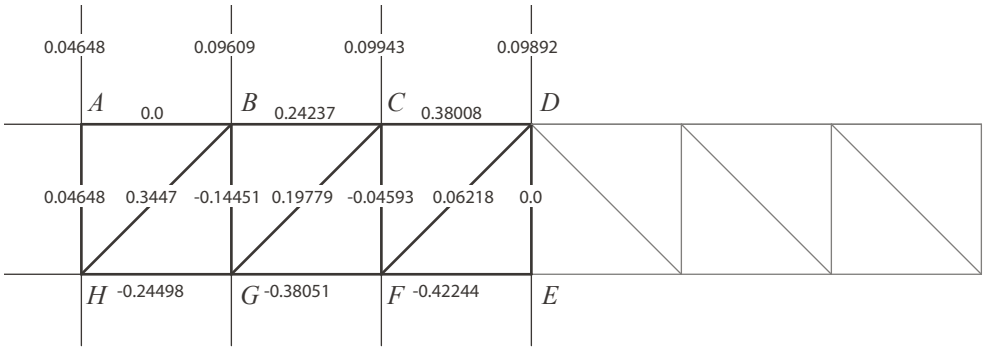

Figure 5.25: Angles between triangulated surfaces calculated with the parametric tool

Bar	***Force N***	***Angle φ***	***Ratio (N/φ)***
AB	0	0.0	N/A
BC	−5	0.2437	−20.52
CD	−8	0.38008	−21.05
EF	+9	−0.42244	−21.30
FG	+8	−0.38051	−21.02
GH	+5	−0.24498	−20.41
AH	−1	0.04648	−21.51
BG	+3	−0.14451	−20.76
CF	+1	−0.04593	−21.77
DE	0	0.0	N/A
BH	−5√2	0.3447	−20.51
CG	−3√2	0.19779	−21.45
DF	−√2	0.06218	−22.74

Table 5.1: Angles between triangulated surfaces calculated with the parametric tool

maximum deviation of approximately 11%. This shows that the discretisation can result in inaccuracies.

With this knowledge, let us use the tool to create a number of head-to-tail diagrams of the lattice girder to evaluate if the inaccuracy is present here too. The diagrams of points B, C and D are given in Figure 5.26. Each of these points returns a head-to-tail diagram that does not form a closed loop. The differences are similar to those of the diagrams created in *5.2.2*. It can therefore be concluded that the discretisation causes this inaccuracy.

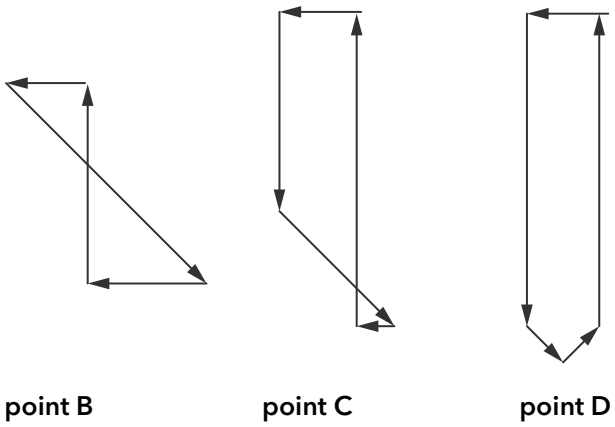

Figure 5.26: Head-to-tail diagrams of lattice girder

5.3 TOOL RECIPROCAL FIGURE BY CONNECTIVITY

In *5.1*, a thrust surface was created by creating polyhedrons from the centre outwards and intersecting and joining these rings together. In order to form a continuous polyhedron, only surfaces that form convex angles are joined. This results in a connectivity in Polyhedron B that is different from that in Polyhedron A, meaning that these are technically not reciprocal to one another. The regenerated mesh in Figure 5.7 shows this occurrence. In Figure 5.20 it is shown that this approach results in a figure with only compression through the edges, and that data about tension in the structure gets neglected. In this section, an alternative approach is taken in order to generate a complete reciprocal figure; the connectivity between vertices in Polyhedron A is used in creating Polyhedron B.

5.3.1 CONNECTIVITY

We already established the three-dimensional geometrical duality between a point and a plane, a line and a line, and a plane and a point in two reciprocal figures. Now, from these dualities we can also derive dual connectivities. In this, a duality exists between the connectivities of again: a point and a plane, a line and a line, and a plane and a point (Konstantatou, D'Acunto, & McRobie, 2018). If two points of one diagram are connected via an edge, then the corresponding faces of the reciprocal figure intersect and share a common edge.

From this it can be concluded that by identifying the connectivity between vertices in Polyhedron A, we can determine which faces intersect in Polyhedron B. If the intersection between two faces from two connected vertices is calculated, we find the corresponding edge in Polyhedron B. Since the edges meeting in a vertex in Polyhedron A form the bounding edges of a face in Polyhedron B, these faces can now be determined. This occurrence is shown in Figure 5.27. When we assess the highlighted triangle for instance, we find that it is created by connecting vertices 1, 3 and 4. The bounding edges of this triangle are clockwise c, l and d, which correspond to edges C, L and D in the reciprocal figure. Naturally, this exercise can also be carried out the other way around; vertex 9 is connected to vertices 2, 1 and 8 clockwise by edges j, a and i. These vertices

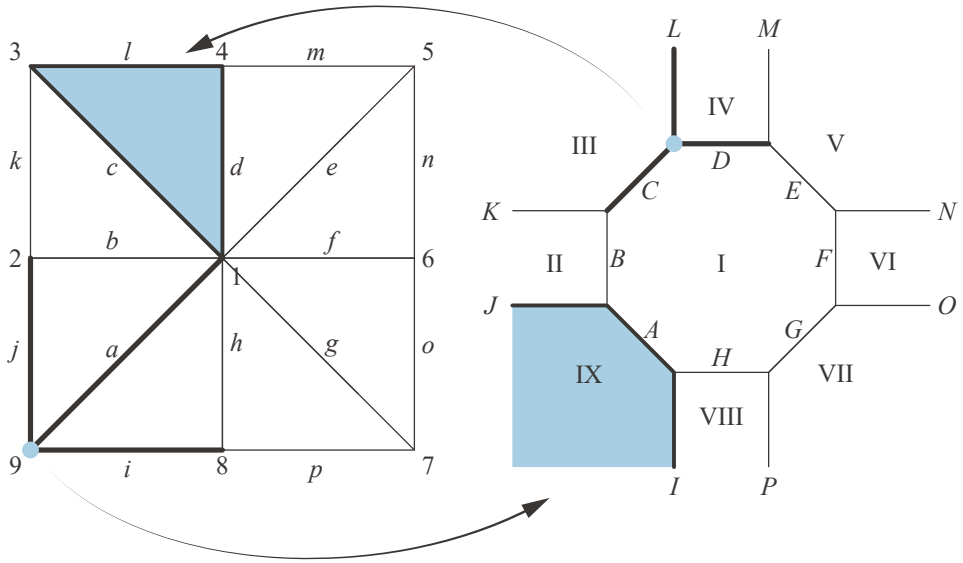

Figure 5.27: Connectivity between reciprocal figures

correspond respectively with faces II, I and VIII. The edges enclosing these faces are reciprocal to the edges connecting the vertices in the initial figure.

5.3.2 PARAMETRIC TOOL

The knowledge from *5.3.1* can now be applied in a parametric tool to construct the complete reciprocal figure of the Airy stress function, taking both tension and compression into account. Equal to the parametric tool from *5.1*, the input data is a point cloud of the Airy stress function. This point cloud can be computed by a tool such as that of Riemens (that was used in most previous examples), but can in simpler cases also be derived from a formula. Any shape can hereby be used, as well as any boundary condition. After all, boundary conditions such as the support cases, load cases and the geometry all influence the outcome of the Airy stress function.

Methodology

The process starts again with creating a triangulated mesh from the vertices of the Airy stress function, making sure that all faces are planar. Equal to the parametric tool from *5.1*, the vertices are mapped to planes through the formula from [3.37]. The result is a list of surfaces F_i'.

In order to create the reciprocal figure based on connectivity, first a connectivity matrix must be established. The Grasshopper cluster governing this process is given in *Appendix E*. The triangulated Airy stress mesh consists of vertices and faces, the faces of which each have three bounding edges. First, all edges of the mesh are identified, and related to each point in the Airy stress point cloud. This results in the corresponding edges for each point, the number of which depends on its valency.

Once it is established which point lies on which edge, it can also be determined which two points lie on a single edge. By doing this for all points, we get a matrix with the connectivity C_V for each vertex in the Airy stress mesh. Subsequently, these points are sorted clockwise, giving us the sorting indices with which the reciprocal planes are later sorted too. Using these sorting indices, the connectivity matrix is sorted accordingly.

Each plane reciprocal to the Airy stress vertices is then intersected with its corresponding planes. The result is a number of 'infinite' edges, intersecting adjacent edges at vertices V_i' reciprocal to the Airy stress faces F_i. Connecting these vertices with edges E_i', gives the reciprocal force polygon (F_i').

In order to obtain a better insight into the structural behaviour of the assessed structure, it is helpful to make a distinction between edges that act in compression and those that act in tension. It was explained in *5.2.1* that a convex angle between two faces in the Airy stress mesh indicates a mutual edge in compression, and a concave angle indicates a mutual edge in tension. In order to determine the convexity of an angle, a line is drawn between the centroids of two corresponding faces. If the line is located underneath the Airy stress mesh, then the angle is convex and the edge thus acts in compression. If the line is located above the mesh, then the angle is concave and thus acts in tension.

A process diagram of the tool is given in Figure 5.28. See *Appendix F* for an image of the full Grasshopper script.

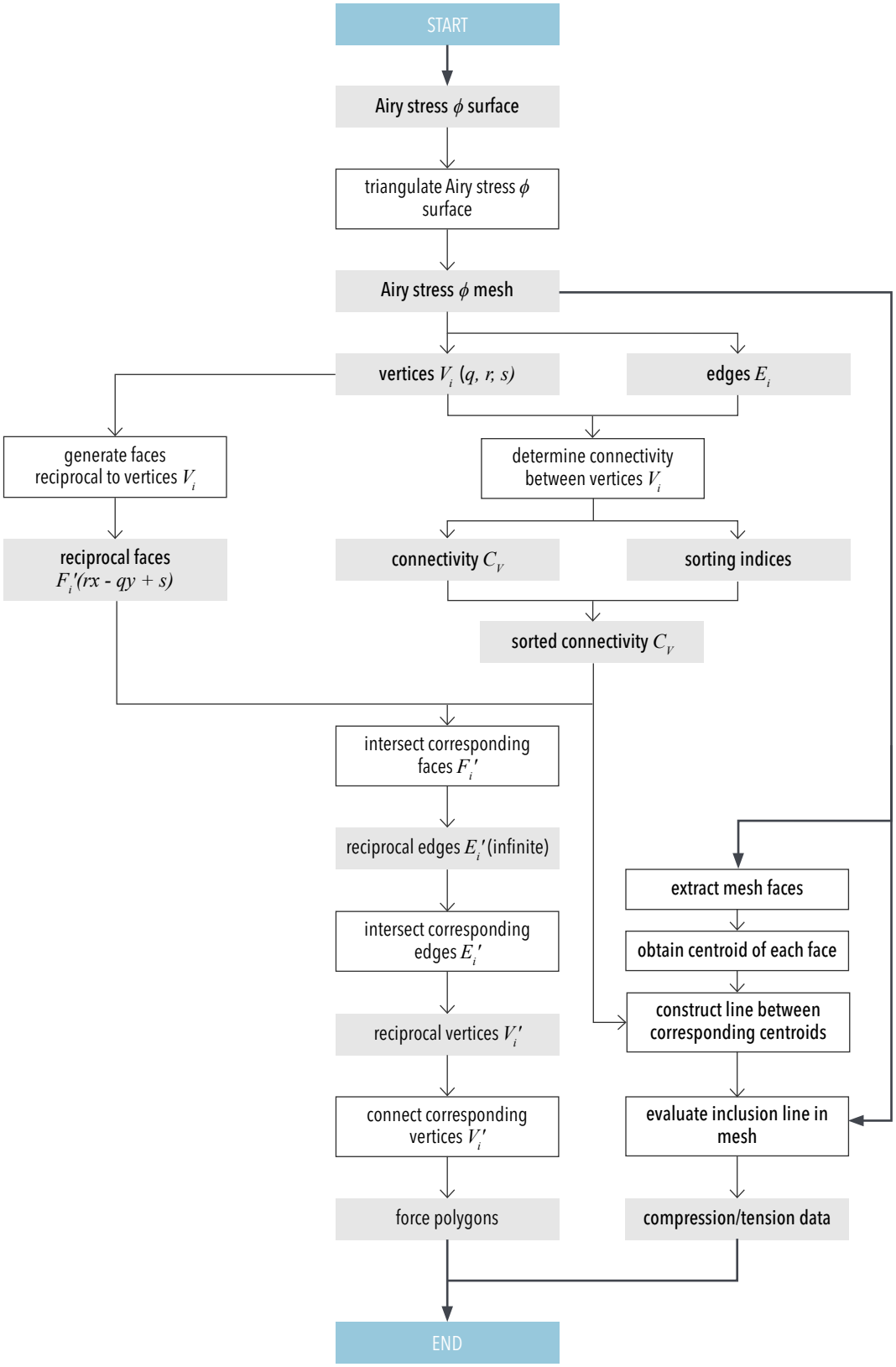

Figure 5.28: Process diagram of parametric tool to generate reciprocal polyhedron via connectivity

5.3.3 RESULTS

In order to validate the performance of the parametric tool, a number of Airy stress functions with various geometrical properties are assessed. From each of these functions, the reciprocal figure is generated. By comparing the individual results, a better understanding is acquired of the process of the tool. The following geometries will respectively be analysed:

– Square shell on semi-rigid edges
– Rectangular shell on four supports on four supports
– Airy stress function from a dome-like structuree

For each case, images are taken from various angles in order to give comprehensive insight into the process of the parametric tool. Polygons that are only in compression are shown separate to polygons consisting of edges in both tension and compression. Again, the angular defect between two faces sharing an edge E_i in the Airy stress mesh determines the force in its reciprocal edge E_i' (as explained earlier in *5.1.2*). So, each force in the form polyhedron can be calculated, where tensile forces are given a negative sign. To provide better insight into the mechanical behaviour of each structure, compressive forces are visualised in blue, and tensile forces in red. The magnitude of each force determines the tint; ranging from white for a force of zero to respectively blue or red for higher forces.

Some additional images of the results generated by the tool are attached in *Appendix G* as well as the reciprocal figure of a three-valent mesh.

Square shell on semi-rigid edges

Consider the $\bar{M}$-hill of a simply-supported square plate that is subjected to a distributed load, of which we compute the Airy stress function (Figure 5.29). The angles between adjacent faces in the Airy stress mesh give the forces in the reciprocal figure. The magnitude of these forces is visualised in Figure 5.30. It should be noted that the edges in the Airy stress mesh are perpendicular to those in the reciprocal figure. It can be observed that only compressive forces occur in the centre of the structure, but that a combination of compression and tension arises towards the supports. At the locations where tensile forces start occurring, the reciprocal figure appears to flip its direction (Figure 5.31). All polygons meet in one point, at an angle of 45 degrees (a result of scaling the figure by 1/10).

Many polygons in which tensile forces occur are self-intersecting. It is difficult to imagine these shapes as actual shell geometry, which appears more logical for the polygons that are in compression only. Figure 5.32 shows this difference in a clear manner. Now, when analysing Figure 5.33, the generated figure is similar to a tensegrity structure, where compressive edges are bars and tensile edges are cables. This assumption should later be verified.

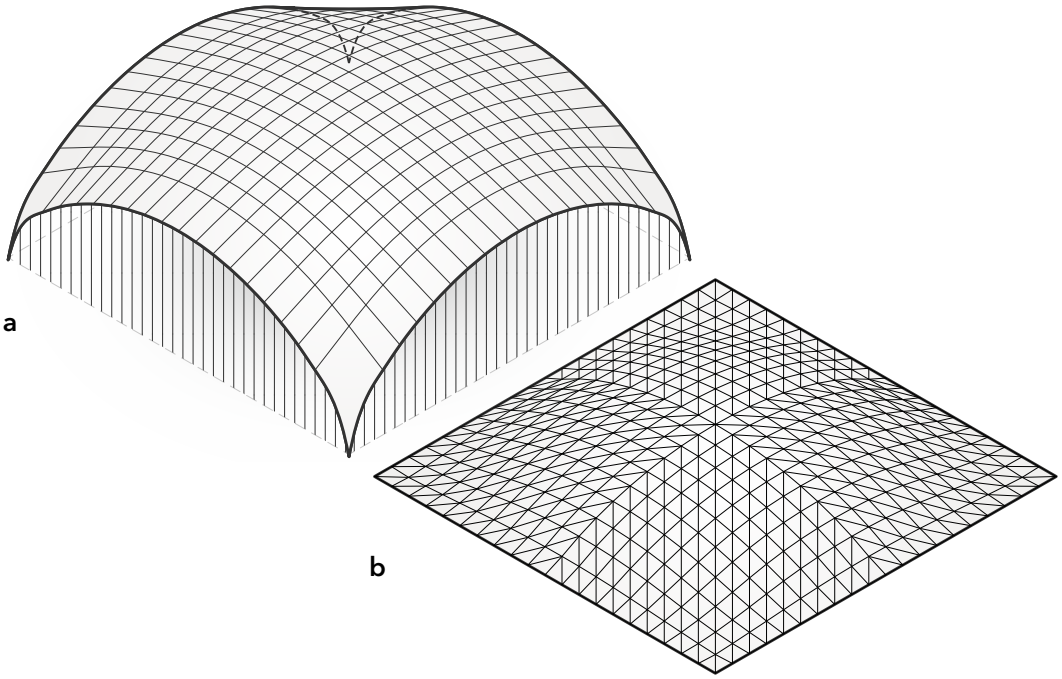

Figure 5.29: $\bar{M}$-hill square plate (a), and corresponding Airy stress mesh (b)

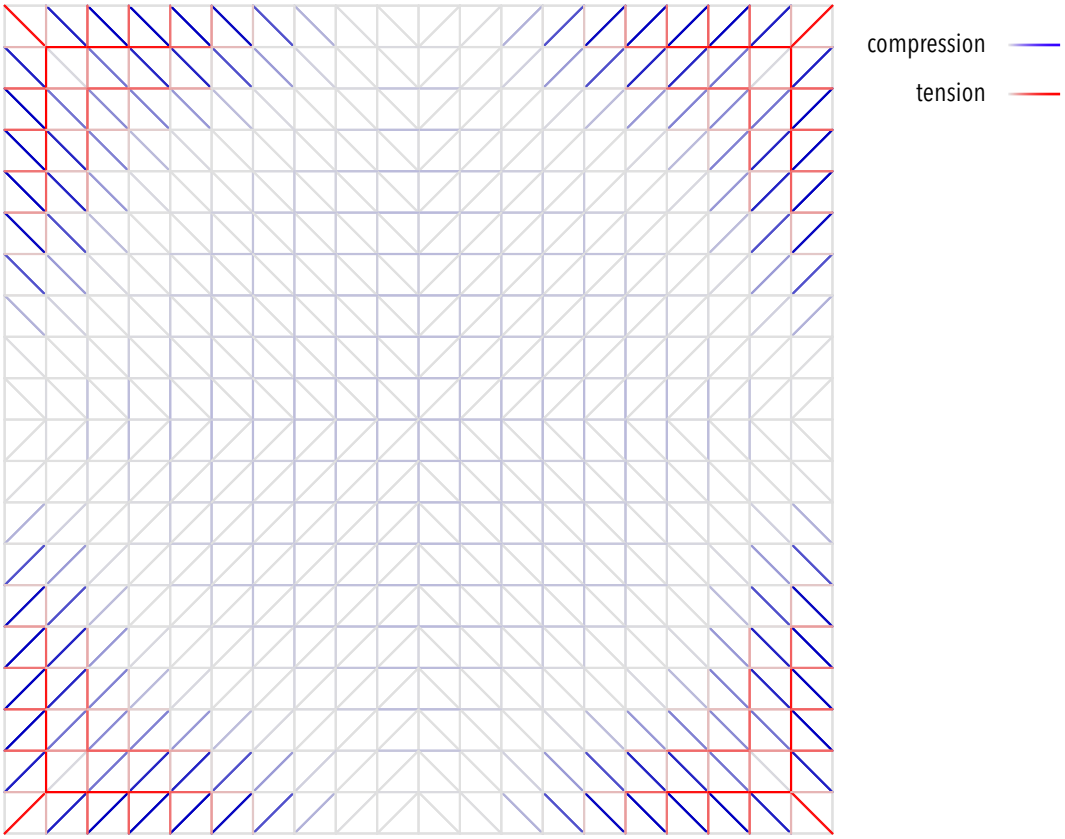

Figure 5.30: Compression (blue lines) and tension (red lines) in Airy stress mesh

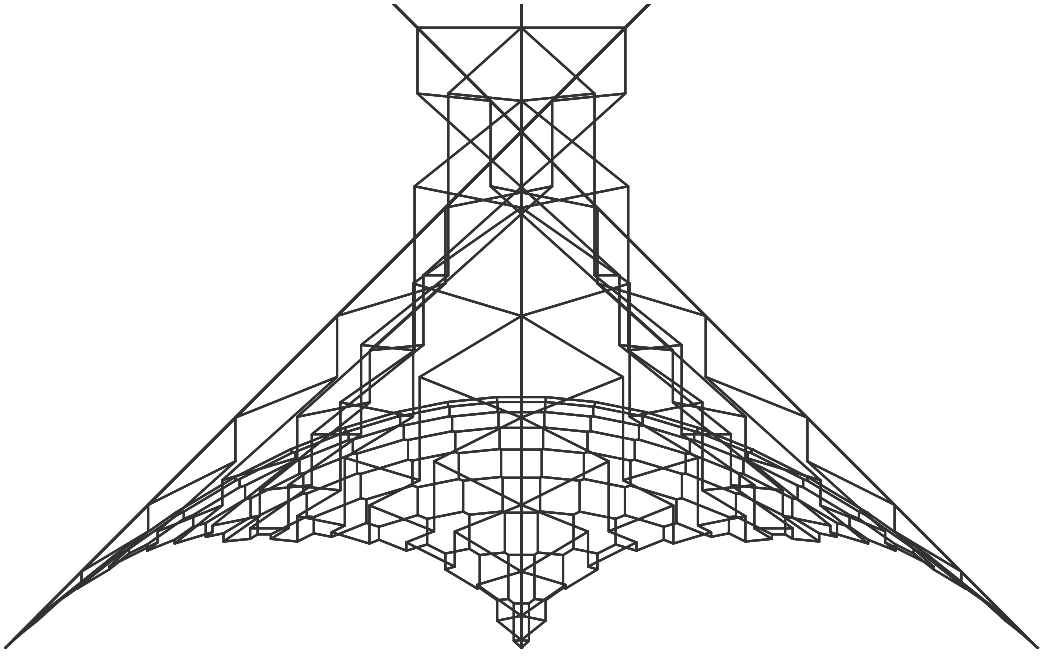

Figure 5.31: Side view of reciprocal figure of Airy stress from square shell on semi-rigid supports

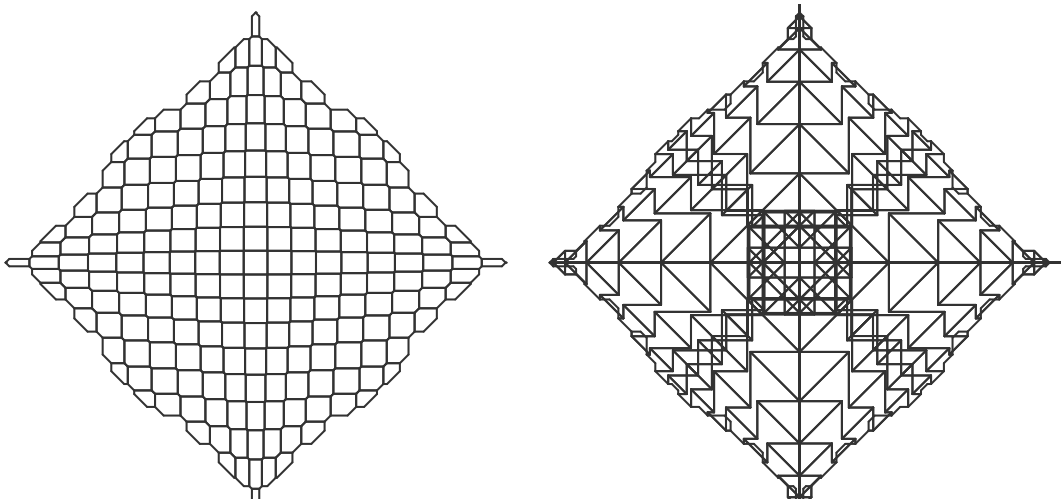

Figure 5.32: Top view reciprocal figure of Airy stress from square shell on semi-rigid supports with compression-only polygons (left) and tension and compression polygons (right)

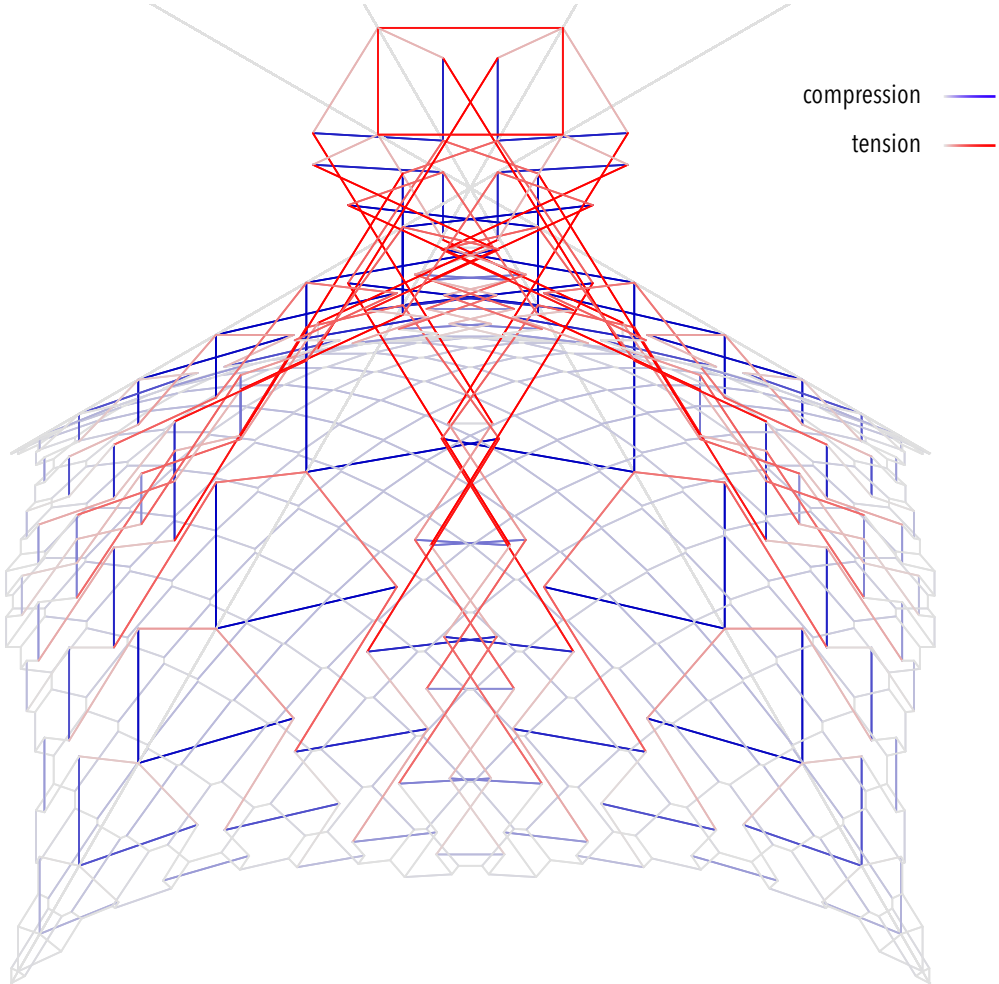

Figure 5.33: Reciprocal figure of Airy stress from square shell on semi-rigid supports

Rectangular shell on four supports

A simple rectangular elpar shell is created by means of the parabolic function from [5.3] with dimensions of 20 x 30 m (Figure 5.34a). It is simply-supported on four corners and subjected to a projected load. Computing the Airy stress function of this case gives Figure 5.34b.

Computing the reciprocal figure of this Airy stress mesh gives Figure 5.35. The grey colour in the centre indicates very low compressive forces, so here the structure shows shell-like behaviour. However, towards the supports corners, large tensile forces occur. Considering that it is supported on four corners, as opposed to the semi-rigid edges from the previous example, these higher tensile forces can be explained.

$$z = \frac{x^2 + y^2}{50} \qquad [5.3]$$

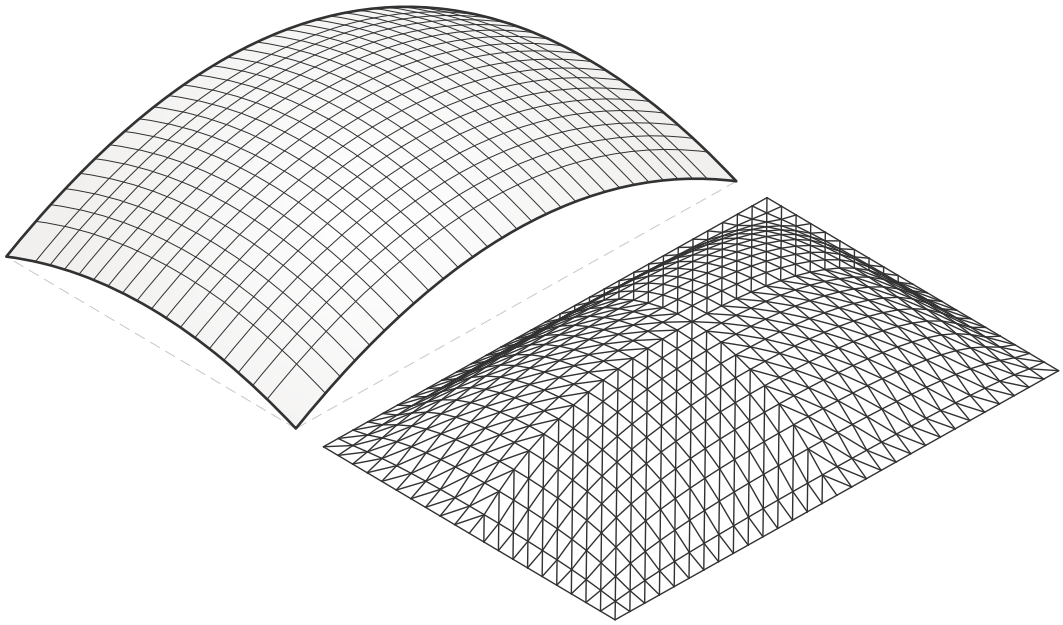

Figure 5.34: Rectangular elpar shell (left) and its corresponding Airy stress mesh

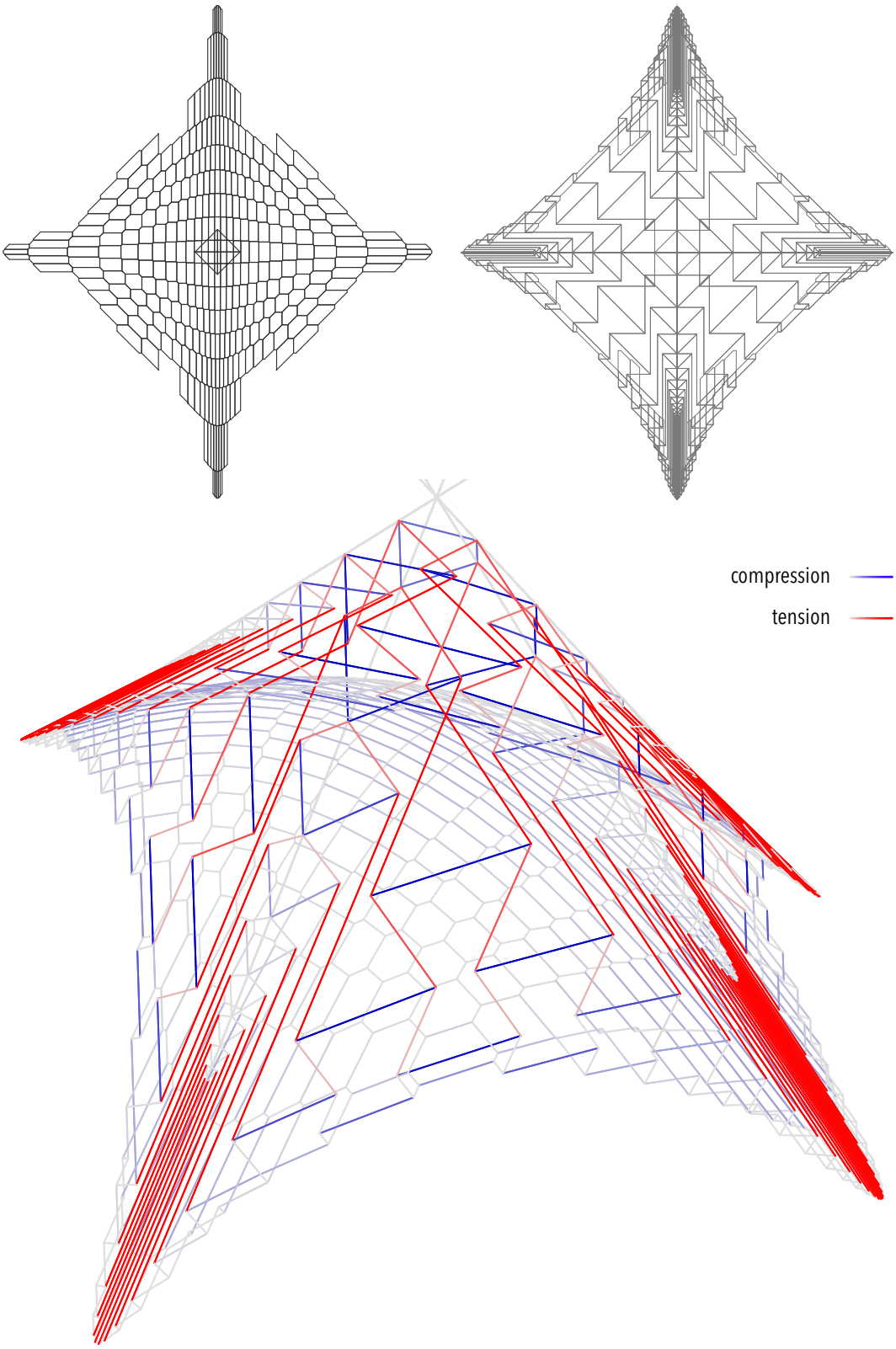

Figure 5.35: Reciprocal figure of Airy stress from rectangular shell on semi-rigid support; compression-only (top left), tension and compression (top right) and holistic image (bottom)

Airy stress function from a dome-like structure

In both previous examples tensile forces occur towards the corners, resulting in geometry that is difficult to interpret as form diagram. The part that works purely in compression, however, appears to have a circular footprint. It is therefore interesting to create the reciprocal figure of a dome-like structure to get a better understanding of the process.

A conceptual Airy stress mesh with a parabolic section is created as in Figure 5.36. Since there are no convex angles between planes, we can expect the reciprocal figure to solely acct in compression. Calculating the angle and colouring the Airy stress edges by magnitude gives Figure 5.37. Its reciprocal figure is shown in Figure 5.38. The tangential edges appear to be uniform towards the edges. The radial forces are minimal in the centre, but increase outwards. At the supports, a number of lines go towards a focal point *f*. It is likely that these forces represent the resultants at the supports.

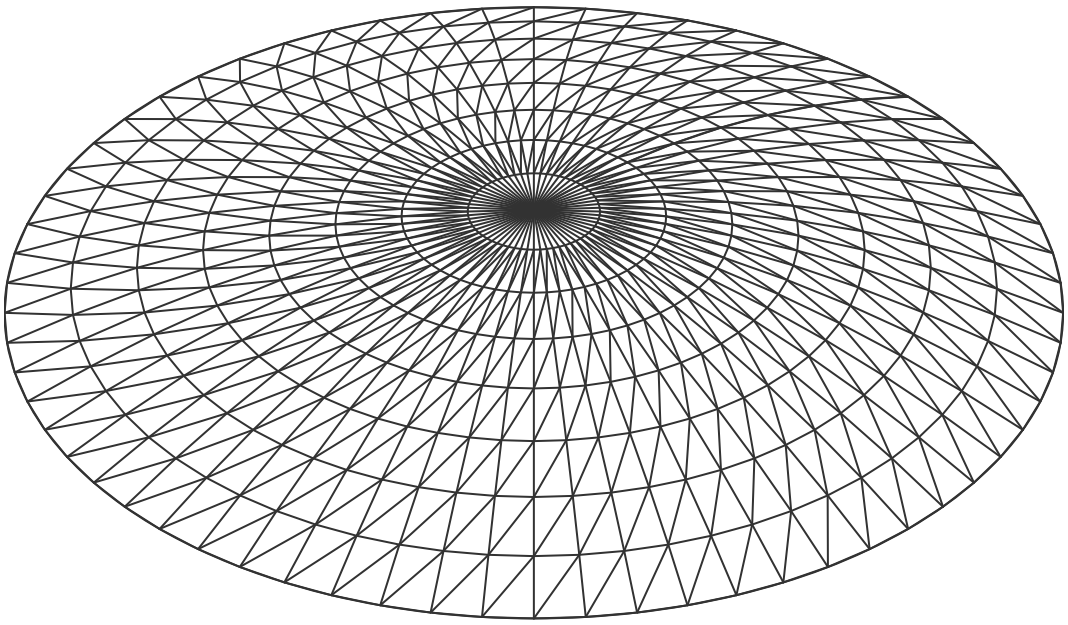

Figure 5.36: Meshed Airy stress function of a dome-like structure

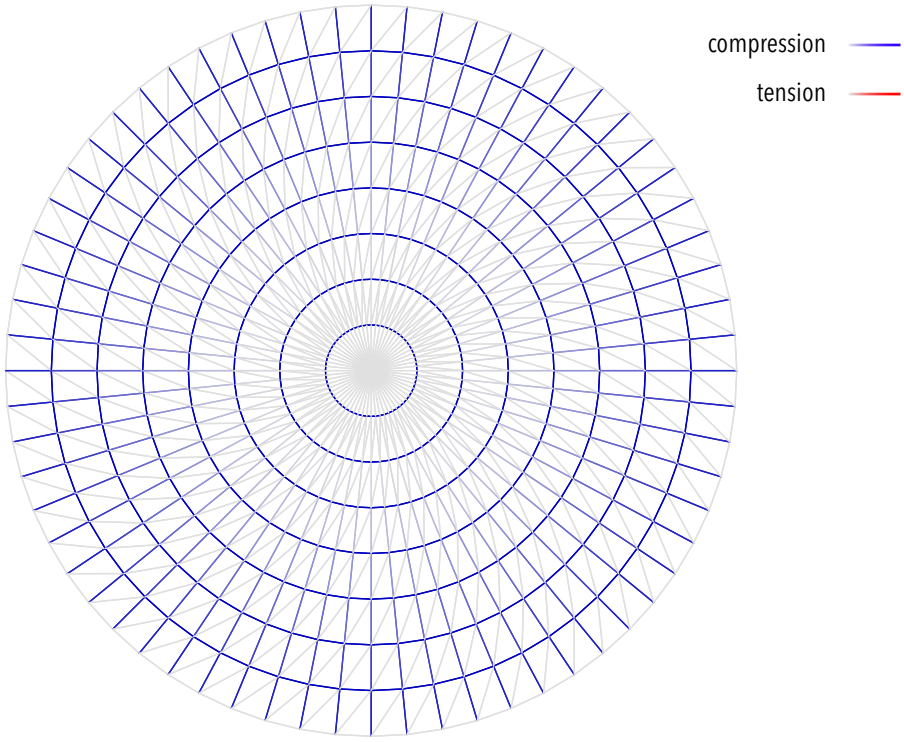

Figure 5.37: Top view reciprocal figure of Airy stress from dome-like structure

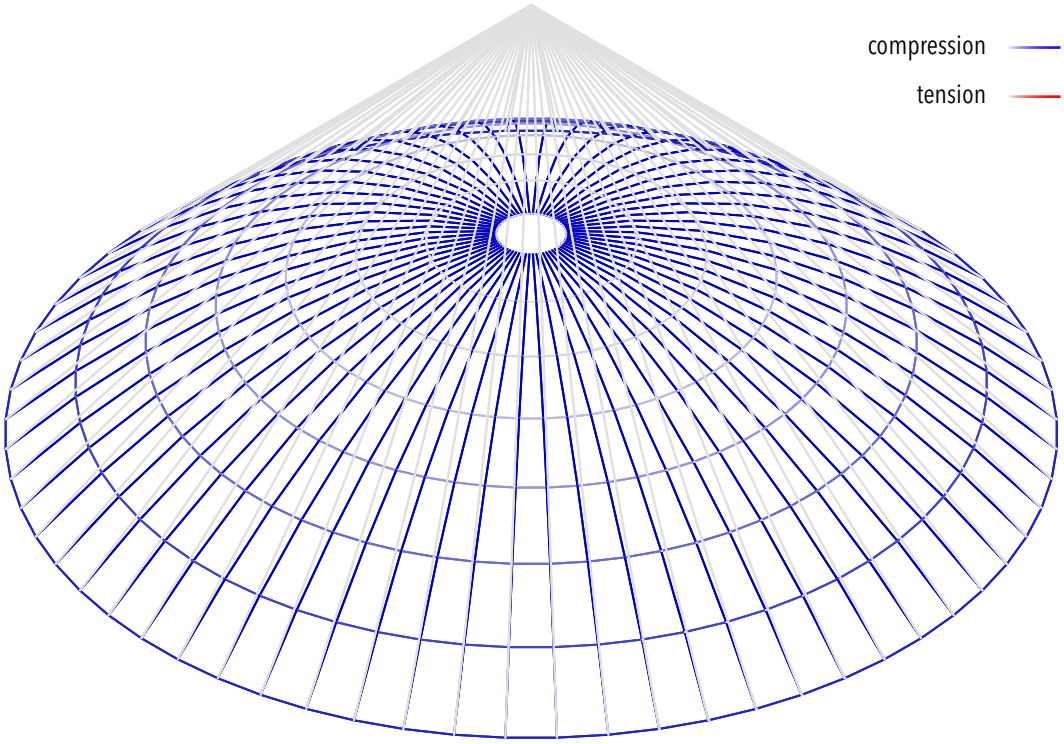

Figure 5.38: Reciprocal figure of Airy stress from a dome-like structure

5.3.4 DISCUSSION OF THE RESULTS

Three different Airy stress functions were used to create the reciprocal figure from. A number of conclusions can be drawn from analysing the results, that are discussed here.

Edges in tension

Different from the first proposed tool, this tool is capable of not only converting synclastic, but also converting anticlastic parts of the Airy stress function. These edges are considered to be in tension in the reciprocal figure. When producing the head-to-tail diagrams via the second tool, it was already observed that polygons in tension flipped in direction, resulting in a self-intersecting polyhedron in projection. The same occurrence is observed upon creating the reciprocal figure with this tool. Creating a continuous polyhedron appears therefore not to be possible in a single process. It appears that the 'tensile' polygons are drawn in the correct plane, but in the wrong direction. When we look at the reciprocal figure of the circular Airy stress function, all polygons that meet at the focal point *f*, could well be imagined to continue in the other direction (or form the support reactions).

Force density

When comparing the forces N_i derived from the Airy stress function to the length l_i' of each edge, it appears that this ratio varies across certain structures. In other words, the force density is not equal. From this it can be concluded that the reciprocal figure is not a force polyhedron, since the lengths of the edges do not correspond with the forces going through them. In order to create the force polyhedron, the force density must be distributed evenly. In order to do so, the length of each edge E_i' in the reciprocal figure must be scaled in correspondence with the normal force N_i that is related to it.

Scaling

Since the forces through each edge are known, the horizontal reaction forces can theoretically be determined. By means of the complementary energy, it is then possible to determine the optimal scale of the structure. This thesis does not elaborate further on how to execute this.

5.4 CONCLUSION

In *5.1*, a parametric tool has been proposed with which the force diagram of a shell surface could be made. It makes use of the mathematical notion of reciprocal figures. This parametric tool is used on the Airy stress function, which could be computed with the tool from previous graduate Kris Riemens. By creating a plane-faced polyhedron from this stress function, the reciprocal force diagram could be generated. The parametric tool relies on the discretisation of the stress function, so the result is always an approximation.

A number of force diagrams have been created using the tool. Each result showed a network of edges through which only in-plane forces would travel. This gives insight into the possible occurrence of tension, since the geometry could be compared to the input geometry. This showed too, however, that some information was lost in the reciprocal figure. Especially for shell structures that showed imperfect shell behaviour, a lot of the geometry could not be converted. In this process, the connectivity between vertices was re-established, resulting in a continuous polyhedron.

The force diagrams created by means of the tool are of arbitrary scale. This is characteristic of shell structures, so additional information is needed to determine the optimal scale. Also, since the generated force diagram is of an indeterminate character, the scale between the different edges should be evaluated. Taking a three-valent Airy stress mesh does result in a determinate structure.

Since the force diagram is just a summation of single force polygons, the shell could also be assessed by creating force polygons from the Airy stress polyhedron. For this, an additional parametric tool was created. This tool gives insight into shell parts that are in tension, and creates a more holistic force diagram. By combining these two tools, the optimal scale of the force diagram can potentially be created.

Ultimately, a parametric design tool was proposed that creates the reciprocal figure of the Airy stress function via connectivity. It was proven here that the connectivity between two vertices in the first polyhedron, is reciprocal to the connectivity between two faces in the second. It also showed, however, that creating a reciprocal figure from a partially

anticlastic shell structure resulted in a polyhedron that is self-intersecting in projection. Such polyhedrons were still in equilibrium, so could be considered a force polyhedron rather than a form diagram.

6. CONCLUSION

6 CONCLUSION

6.1 CONCLUSIONS

This research started with the question: *'How can a better understanding of the relation between geometrical and mechanical properties of shell structures be formulated and result in an intuitive and graphical design tool for (structural) designers?'* In order to provide a conclusive answer, first a theoretical framework was created. This framework comprised of basic understanding of curved geometry, differential equations of shells, and established boundary conditions that are used throughout this thesis. Then, a number of topics were discussed that were more specifically related to the design and evaluation of shell structures.

In *1.4.2*, a hypothesis was stated as follows: *'An analogy is present between (1) the geometry of a moment hill of a plate and (2) the thrust surface of a shell subjected to a distributed load, and their boundary conditions are mutually related.'* This analogy has been thoroughly assessed. In this process, an attempt was made to relate flat plates to their shell equivalents. The rainflow analogy proved helpful in the understanding of the structural behaviour of each shell. This resulted in a number of proposals for analogies between two-dimensional geometries and their three-dimensional shell equivalents.

Additionally, the mathematical notion of reciprocal figures has been studied carefully, and was implemented in combination with the Airy stress function. It was established that the reciprocal figure of the Airy stress polyhedron was the force diagram of a shell structure, and the expectation was stated that combining these would allow for the design and assessment of shell structure geometry. Graphic statics proved to be applicable here, and provided a better understanding of reciprocal figures in general. Finally, a relationship between the moment hill of a flat plate, the Airy stress function, and the thrust surface of a shell was presented.

A parametric tool has been proposed with which the force diagram of a shell surface could be made using the notion of reciprocity. This parametric tool is used on a discretised approximation of the Airy stress function. A number of force diagrams have been created using the tool. Each result showed a network of edges through which

only in-plane forces would travel. This showed too, however, that some information was lost in the reciprocal figure. Especially for shell structures that showed imperfect shell behaviour, a lot of the geometry could not be converted. Also, since the generated force diagram is of an indeterminate character, the scale between the different edges should be evaluated.

Another tool was created to form individual force diagrams from the stress resultants of Airy stress functions. Since the force diagram is just a summation of single force polygons, the shell could also be assessed by creating these from the Airy stress polyhedron. The tool gave insight into shell parts that were in tension, and created a more holistic force diagram. By combining these two tools, the optimal scale of the force diagram can potentially be created.

Ultimately, a parametric tool has been created that allows for the creation of holistic reciprocal figures of any Airy stress function. This tool makes use of the connectivity between vertices in the Airy stress mesh, which is reciprocal to the connectivity of planes in the generated figure. A number of examples were assessed, each resulting in a closed polyhedron. The parametric tool allows for visualisation of the magnitude of the forces through the structure, as well as separating compression and tension. In cases where tension occurs, however, a reciprocal figure is created with a self-intersecting projection. A continuous figure can only be created for Airy stress functions in which solely compression occurs.

To conclude, let us once again review the research question. A clear relationship between the moment hill of a flat plate and its shell equivalent was established. By using the Airy stress function and its reciprocal figure, this relationship could further be exploited into the design and assessment of shell structures. For this, three parametric tools were generated that allow for the design of shells, but also gives insight in the force trajectories. For now, the scale of the generated shell is determined arbitrarily, but this could be elaborated further in a following research project. Since the forces in the edges are known, the horizontal resultants in the supports can also be determined, and with that the optimal scale.

6.2 RECOMMENDATIONS

Analogies were proposed between square plates and shells and circular plates and shells. Other geometric shapes such as asymmetrical cases for instance, have not been within the scope of this research. It could, however, be interesting to research whether the same analogies exist in different shapes. Similarly, different boundary conditions could also be assessed in future research.

In the creation of the moment hills of twistless cases, DIANA FEA was used. It was already discussed that this could have led to inaccuracies in the shell geometry. In a further research, a more accurate method to create shells from twistless plates, such as the FDM could be explored. These shells are expected to show even better shell-like behaviour.

The proposed parametric tools showed good performance in the creation of a reciprocal figure from a convex Airy stress mesh, but posed challenges in case of concave parts. Since the concave parts correspond with tensile forces in the structure, interpreting the results proved to be difficult. The force polygons in which tension occurs are often self-intersecting, and are difficult to imagine as structure. Also, these polygons flipped towards the centre point of the figure. A lot of research can still be done on this occurrence, and on how to create a continuous reciprocal figure from any Airy stress function.

6.3 REFLECTION

Graduation process

The Building Technology master track is positioned between architecture and civil engineering, and incorporates a variety of courses. Across these courses, a design aspect - which is closely related to architecture - is manifested. And with that, the reasoning behind all design decisions is required to be substantiated. The engineering aspect, whether in building physics, material science or structural mechanics, forms the foundation of any of these design decisions. This combination makes the course unique, as it enables its graduates to operate in between architecture and engineering practice.

Throughout my university career I developed an increasing interest in the influence technology can have on architectural decisions. This is why I decided to study Building Technology, and later why I chose to graduate in the track of structural design. The topic of shell structures is relevant for architectural applications, but also helps in exploiting the theory behind its mechanics. In that, a clear mix between design and engineering is found by design through research. In other words, my graduation project explores the mechanics behind shell structures, to better understand how to design them. The parametric tool, which is a product of the project, helps in making these mechanics insightful. Thus, the design and evaluation of shell structures becomes more accessible and understandable to the structural designer or architect.

A number of research methods have been employed throughout. The research process started with a broad literature study, that ranged from basic understanding of curved geometry to thorough study on complex mathematics. Later, iterative testing was done by means of finite element analysis, in order to get a better understanding of the mechanics of shell structures. Part of the process was envisioned early on, but a lot of the methods developed along the way. A combination between theory and application remained present throughout. This proved to be a very effective work-flow, as it allowed for the understanding of otherwise complicated matter. In hindsight, the planning has broadly been followed. Some changes were made along the way, as the direction of the project developed gradually.

Societal impact

Over the years, a lot of research has been done on shell structures. The thrust surface proved to be helpful in understanding the force flow through the structure. The shape of this surface, however, was considered complicated to determine. Philippe Block and his team proposed a method called the Thrust Network Analysis, but this method still produces many possible surface geometries, and not one optimal case. The method also turned out very complicated and tedious to use.

In my project, I propose the use of the Airy stress function in creating the thrust surface, a relation (between form and force diagram) that was already observed in 1870 by Maxwell. This allows to both analyse existing shell structures as well as to design new shells. Further research into the moment hill of certain plates allowed for the generation of better stress functions. Little experience exists on the application of the Airy stress function in assessing and designing shell structures. In my graduation proposal, this possibility has been further explored in combination with the reciprocal figure. The Airy stress as the form diagram and the thrust surface as the reciprocal force diagram is an idea not executed before. At the same time, applying graphic statics to the Airy stress enabled extra possibilities in exploiting this relationship. This provided extra insight into the mechanical behaviour, i.e. where tensile stresses occur, and how these can be minimised.

Shell structures only comprise a small part of the built environment. They can be considered a niche element in the diverse sectors of structural design. Shell structures are, however, significant, in that they require practically all that is known of structural mechanics to come together. In order to understand the behaviour of shell structures, we must understand all these aspects. At the same time this means that our findings on shell behaviour are applicable across the entire discipline, potentially presenting new architectural possibilities.

BIBLIOGRAPHY

- Beranek, W. J. (1974). *Vlakke constructiedelen: elasticiteitstheorie*. Delft: Technische Hogeschool Delft, afdeling Bouwkunde.
- Beranek, W. J. (1976). *Berekening van Platen, Deel 1: Theoretische Grondslagen*. Delft: TU Delft.
- Beranek, W. J., & Hobbelman, G. (1984). *Space Frames Designed as 'Twistless Case'*. Paper presented at the Third International Conference on Space Structures, University of Surrey.
- Beranek, W. J. (1989). *Krachtswerking deel 3: Vakwerken standzekerheid*. Delft: TU Delft.
- Blaauwendraad, J. (2002). *Theory of Elasticity Ct 5141: Energy Principles and Variational Methods:* Delft University of Technology: Faculty of Civil Engineering and Geosciences.
- Blaauwendraad, J. (2010). *Plates and FEM: Surprises and Pitfalls*: Springer.
- Blaauwendraad, J., & Hoefakker, J. H. (2014). Introduction to Shells *Structural Shell Analysis: Understanding and Application*. Dordrecht: Springer Netherlands.
- Block, P. (2009). *Thrust Network Analysis, Exploring Three-dimensional Equilibrium*. (PhD), Massachusetts Institute of Technology, Massachusetts.
- Block, P., & Ochsendorf, J. (2007). Thrust Network Analysis: A New Methodology for Three-dimensional Equilibrium. *Journal of the International Association for Shell and Spatial Structures J. IASS, 48*(3).
- Block, P., DeJong, M., & Ochsendorf, J. (2006). As Hangs the Flexible Line: Equilibrium of Masonry Arches. *Nexus Network Journal, 8*(2), 13-24.
- Borgart, A., & Liem, Y. (2011). *Force Network Analysis using Complementary Energy*. Paper presented at the Taller, longer, lighter: Joint Annual Symposium of the International Association for Bridge and Structural Engineering (IABSE) and the International Association for Shell and Spatial Structures (IASS), London, UK.
- Borgart, A., & Oosterhuis, M. (2010). *Parametric model of 3D shear force and bending moment diagrams for out-of-plane loaded plates*. Paper presented at the Proceedings of the International Association for Shell and Spatial Structures (IASS) Symposium 2010, Shanghai, China.

- Calladine, C. R. (1977). The static-geometric analogy in the equations of thin shell structures. *Mathematical Proceedings of the Cambridge Philosophical Society, 82*(02), 335-351.
- Crapo, H., & Whiteley, W. (1993). *Plane Self Stresses and projected Polyhedra I: The Basic Pattem* (Vol. 20).
- van Dijk, N. (2014). *Graphic statics in arches and curved beams*. (MSc), Delft University of Technology, Delft.
- Greenwold, S., & Allen, E. (Producer). (2001, May 22nd, 2018). Active Statics.
- Heyman, J. (1977). *Equilibrium of Shell Structures* (Vol. 6): Clarendon Press.
- Hoogenboom, P. C. J. (2008). *Ronde schijven en platen*. Technische Universiteit Delft: Sectie Constructiemechanica.
- Hooke, R. (1675). *A description of helioscopes, and some other instruments. London.*
- Isler, H. (1959). New shapes for shells. I*nternational Colloquium on construction Processes of Shell Structures, 8*(IASS Bulletin).
- Lewis, W. J. (2003). *Tension Structures: Form and Behaviour*. Warwick: Thomas Telford.
- Konstantatou, M., D'Acunto, P., & McRobie, A. (2018). Polarities in structural analysis and design: n-dimensional graphic statics and structural transformations. *International Journal of Solids and Structures, 152-153,* 272-293.
- Liang, D. (2012). *A Parametric Structural Design Tool (Grasshopper Interface) for Plate Structures*. (MSc), University of Technology Delft, Delft.
- Konstantatou, M., & McRobie, F. (2016). *Reciprocal constructions using conic sections & Poncelet duality.*
- Liem, Y. (2011). *Graphic statics in funicular design: Calculating force equilibrium through complementary energy*. (MSc), University of Technology Delft, Delft.
- Maxwell, J. (1870). Reciprocal Figures, Frames and Diagrams of Forces. *Transactions of the Royal Society of Edinburgh, 26*(I), 1-40.
- Maupertuis, P. (1744). Accord de différentes loix de la nature qui avoient jusqu'ici paru incompatibles.
- Oosterhuis, M. (2010). *A parametric structural design tool for plate structures*. (MSc), Delft University of Technology, Delft.

- Pavlovic, M. N. (1984). A statically determinate truss model for thin shells: two-surface analysis (bending theory). *International Journal for Numerical Methods in Engineering, 20*(October), 1863-1884.
- Riemens, K. (2015). *A Parametric Structural Design Tool for Shell Structures*. (MSc), Delft University of Technology, Delft.
- Ros, J. (2017). *Graphically calculating arcs and shells by using the lowest complementary energy*. (MSc), Delft University of Technology, Delft.
- Schek, H. J. (1973). The force density method for form finding and computation of general networks. *Computer methods in applied mechanics and engineering, 3*(1974), 115-134.
- Simpson, R. (1998). The Mycenaean Highways. *Echos du monde classique: Classical views, XLII*(N.S. 17), 239-260.
- Tiggeler, L. (2009). Interactief drukvlak. (MSc), Delft University of Technology, Delft.
- Van Mele, T., Lachauer, L., Rippman, M., & Block, P. (2012). Geometry-based Understanding of Structures. *Journal of the International Association for Shell and Spatial Structures J. IASS, 53*(4), 285-295.
- Vansice, K., Kulkarni, A., Hartz, C., Konstantatou, M., & Baker, W. (2018). *A 3D Airy Stress Function Tool for Reciprocal Graphic Statics*. Paper presented at the IASS Symposium 2018, Boston.
- Whiteley, W., Ash, P. F., Bolker, E., & Crapo, H. (2013). Convex Polyhedra, Dirichlet Tessellations, and Spider Webs. In M. Senechal (Ed.), *Shaping Space: Exploring Polyhedra in Nature, Art, and the Geometrical Imagination* (pp. 231-251). New York, NY: Springer New York.

LIST OF FIGURES

APPENDICES

APPENDIX A: PARAMETRIC TOOL LIANG

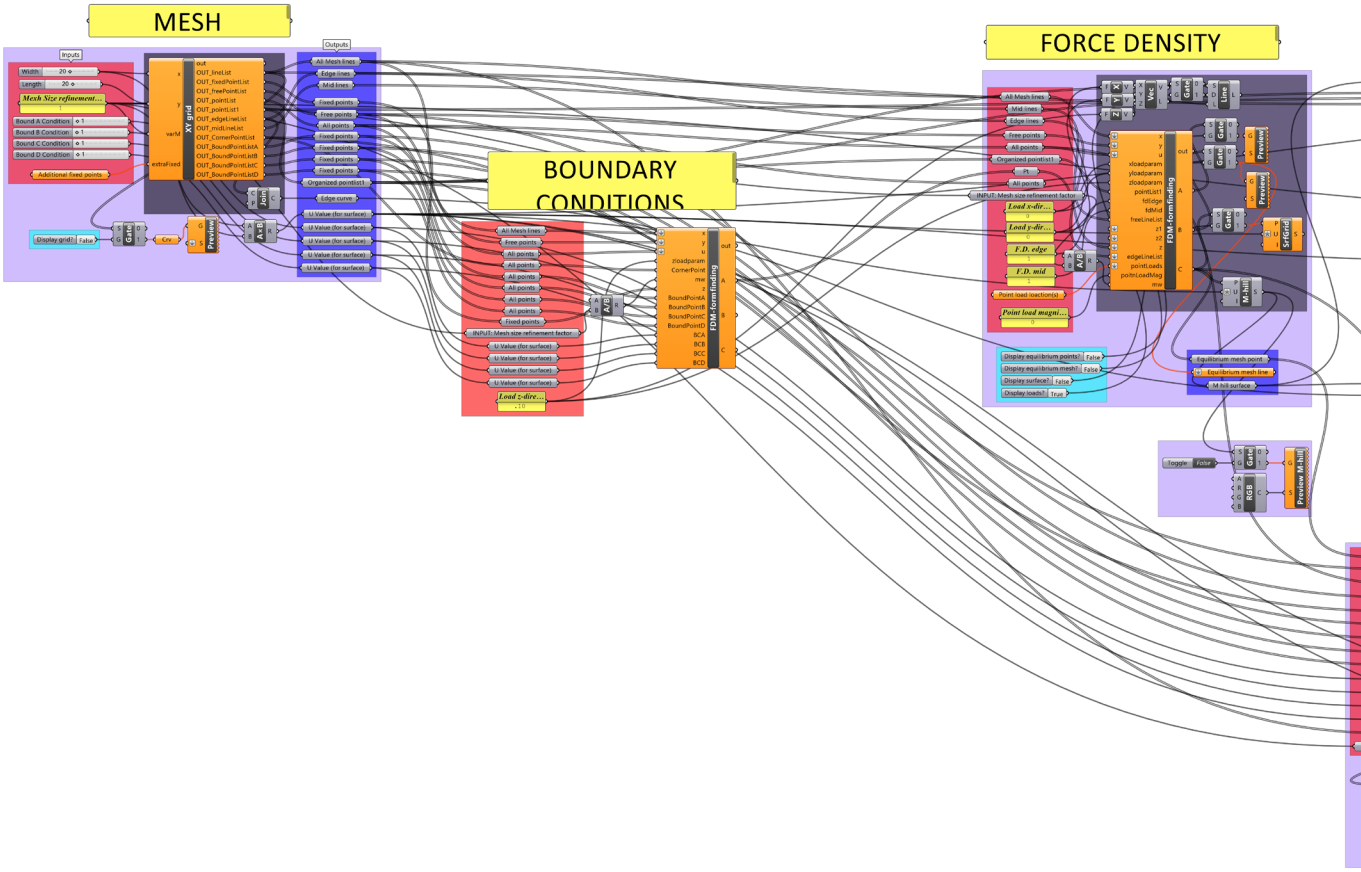

Figure A.1: Grasshopper script of parametric tool from Liang (2012)

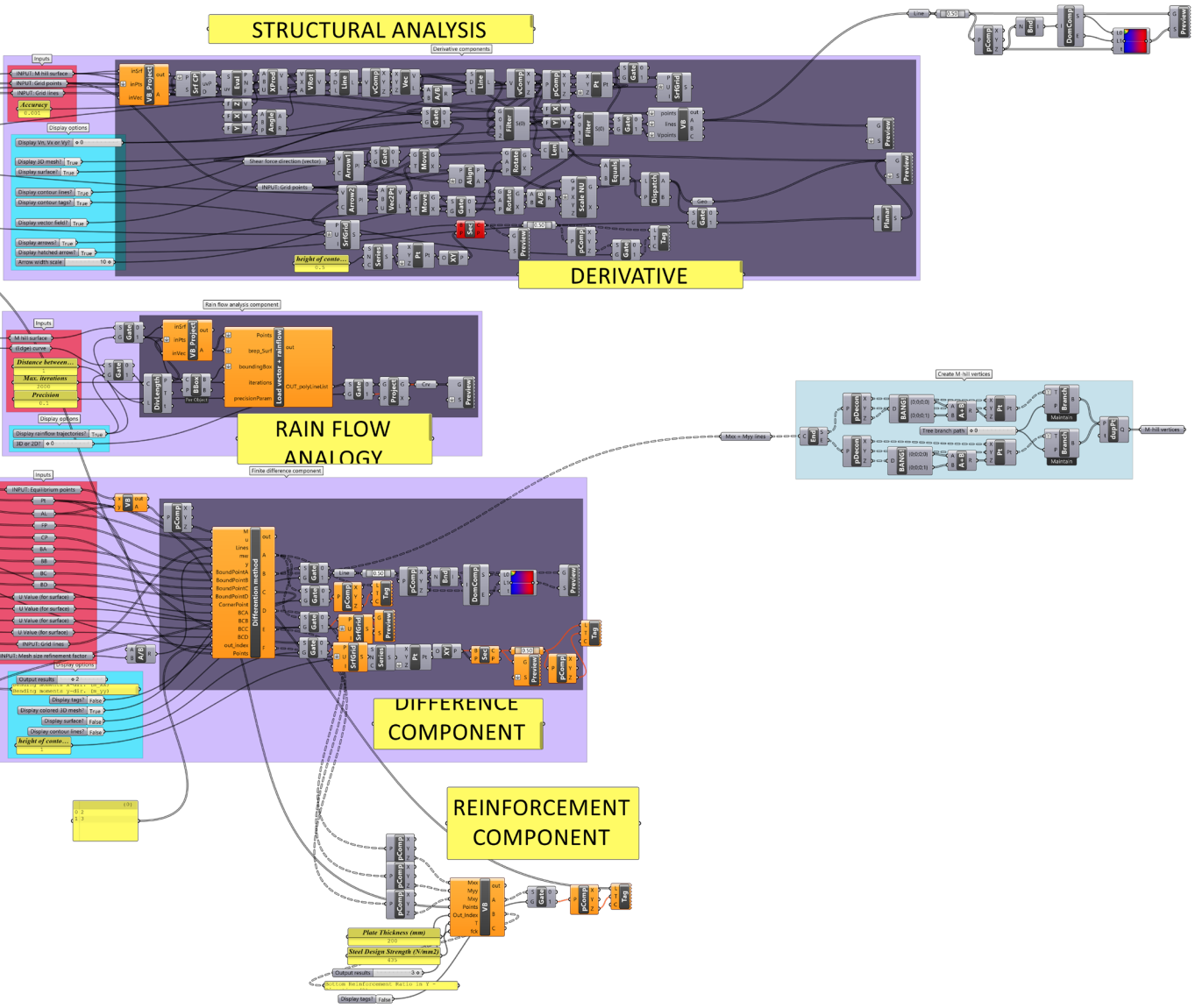
STRUCTURAL ANALYSIS
DERIVATIVE
RAIN FLOW ANALOGY
DIFFERENCE COMPONENT
REINFORCEMENT COMPONENT

APPENDIX B: LOOPING OPERATION TO CREATE POLYHEDRON B

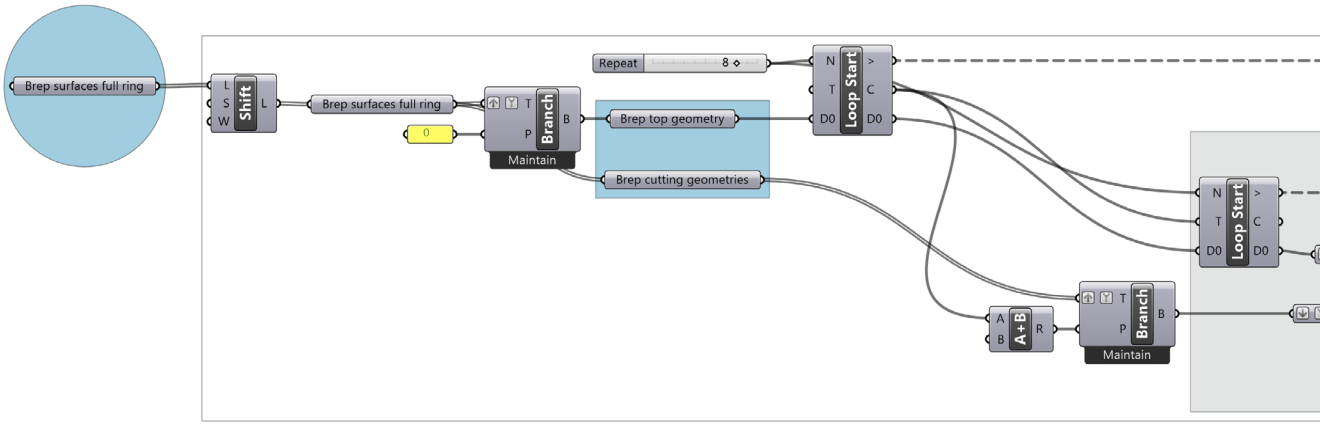

Figure B.1: Grasshopper script looping operation intersecting rings with one another

APPENDIX C: RELATE TRIMMED SURFACES TO AIRY STRESS VERTICES

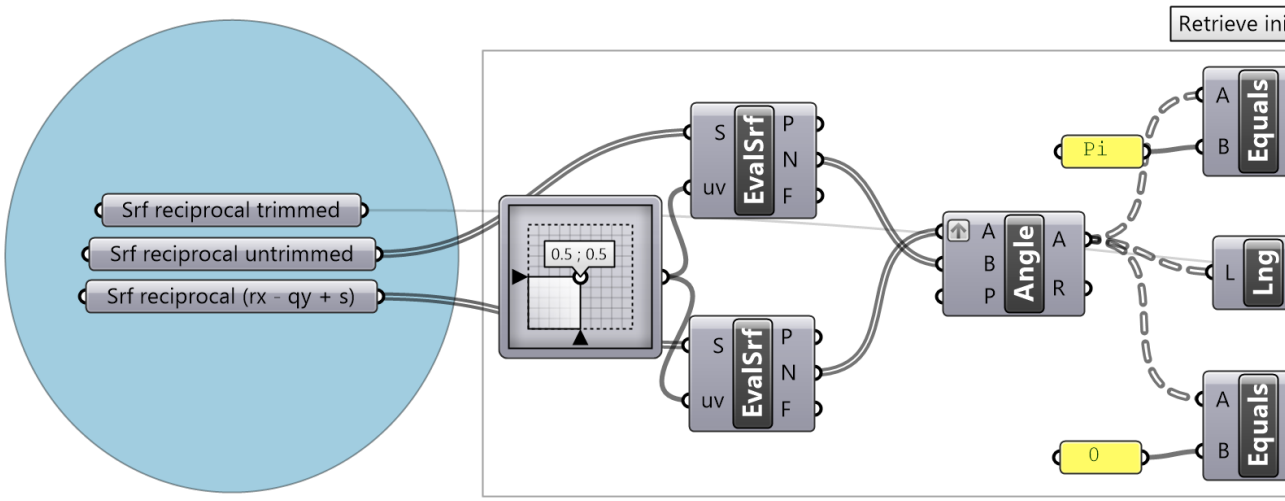

Figure C.1: Grasshopper script that connects created surfaces back to initial vertices from the Airy stress mesh

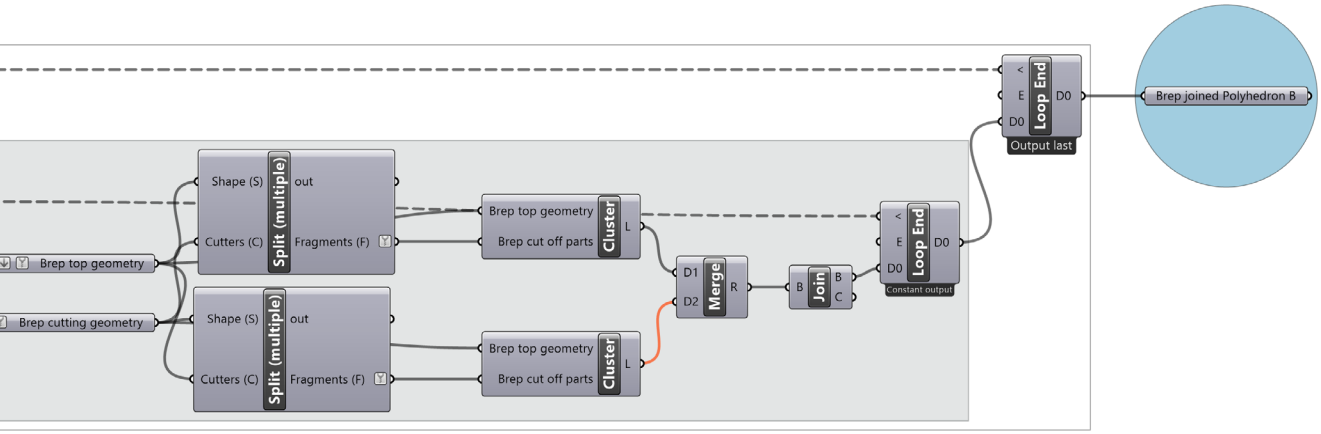
Brep joined Polyhedron B
Loop End
Output last
Brep top geometry
Brep cutting geometry
Shape (S)
Cutters (C)
Split (multiple)
out
Fragments (F)
Brep top geometry
Brep cut off parts
Cluster
Merge
Join
Constant output

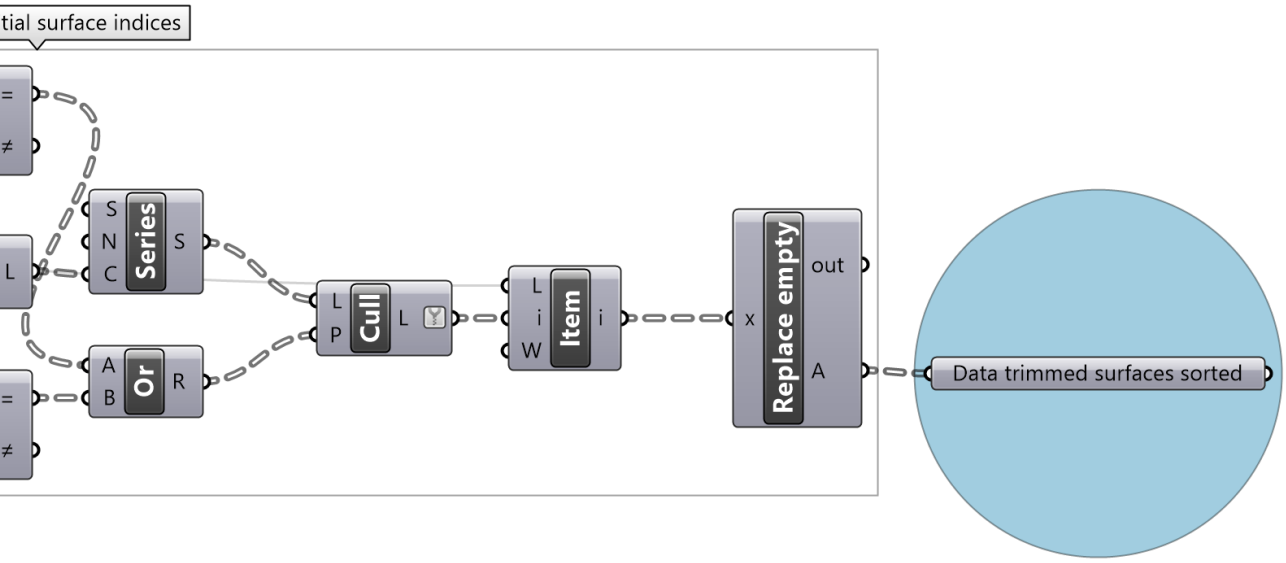
tial surface indices
Series
Or
Cull
Item
Replace empty
out
Data trimmed surfaces sorted

APPENDIX D: DETERMINE DUALITY BETWEEN EDGES

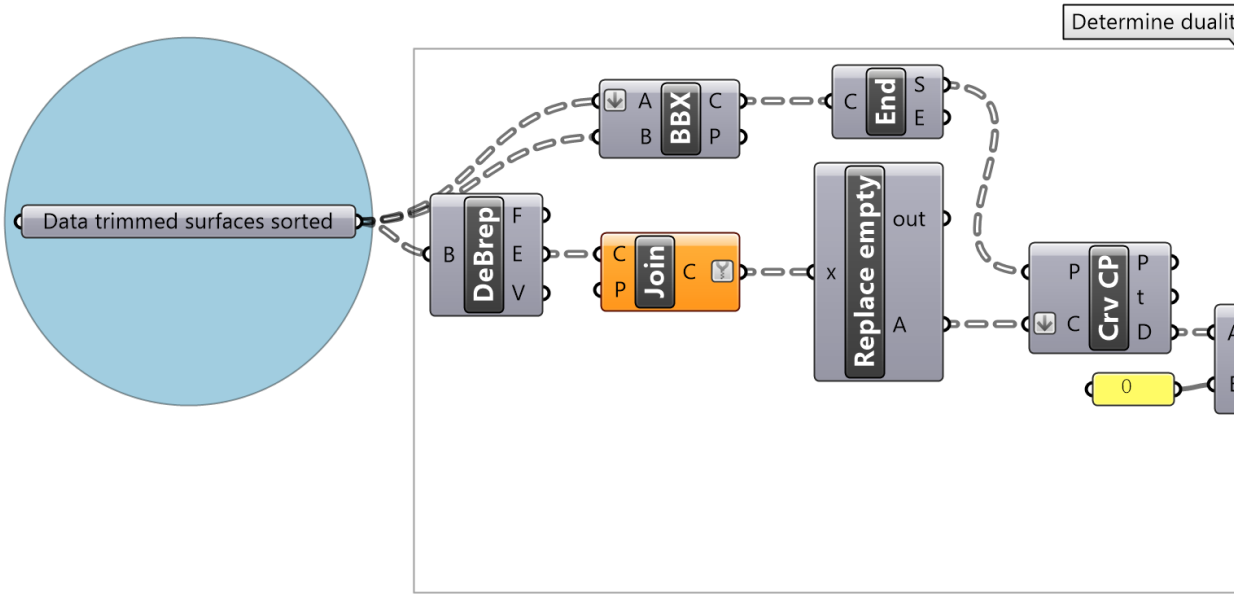

Figure D.1: Grasshopper script that determines duality between edges of the Airy stress mesh and the reciprocal figure

APPENDIX E: DETERMINE CONNECTIVITY BETWEEN VERTICES

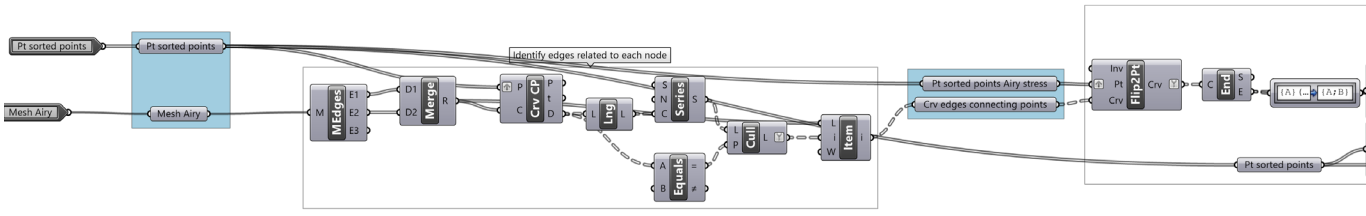

Figure E.1: Grasshopper script that determines connectivity between vertices in a mesh

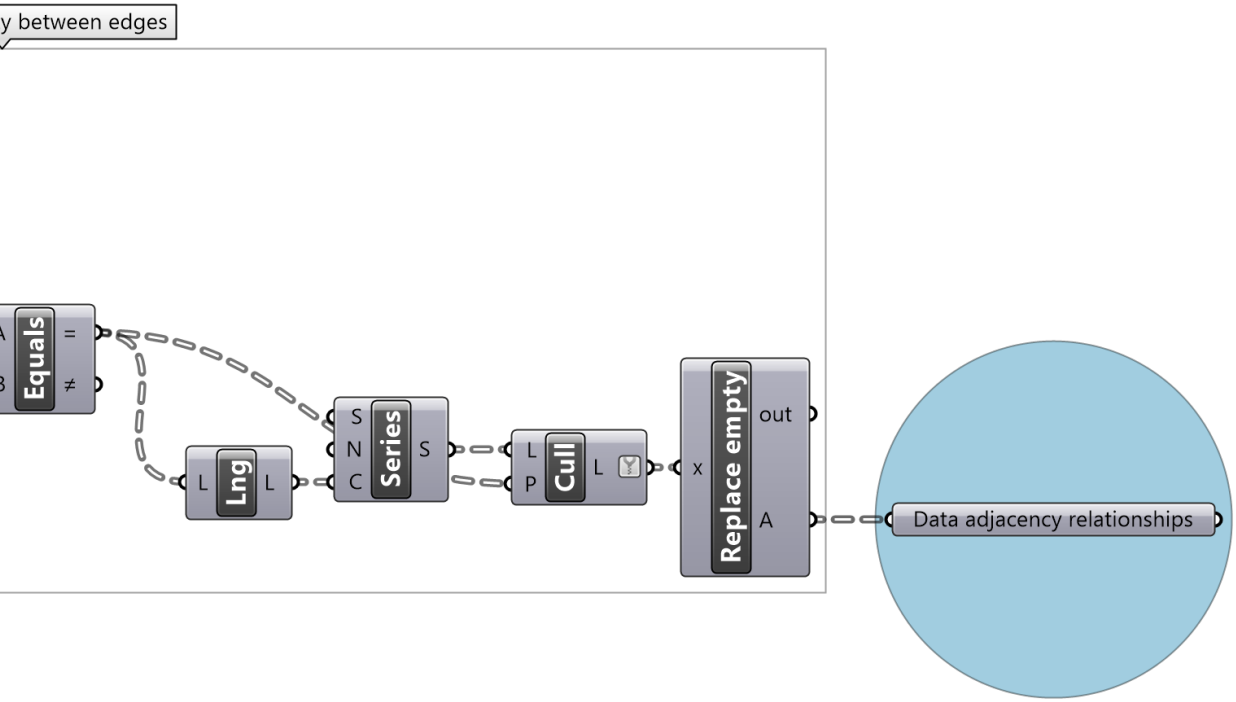
y between edges
Equals
Lng
Series
Cull
Replace empty
out
Data adjacency relationships

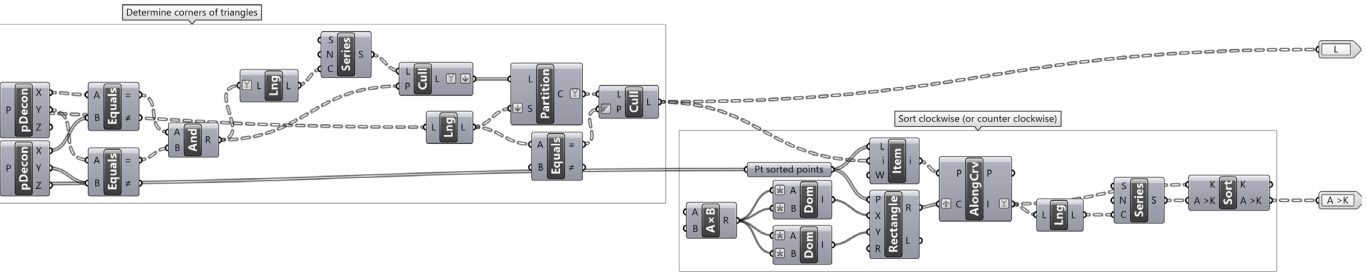
Determine corners of triangles
Sort clockwise (or counter clockwise)
Pt sorted points

APPENDIX F: RECIPROCAL FIGURE VIA CONNECTIVITY

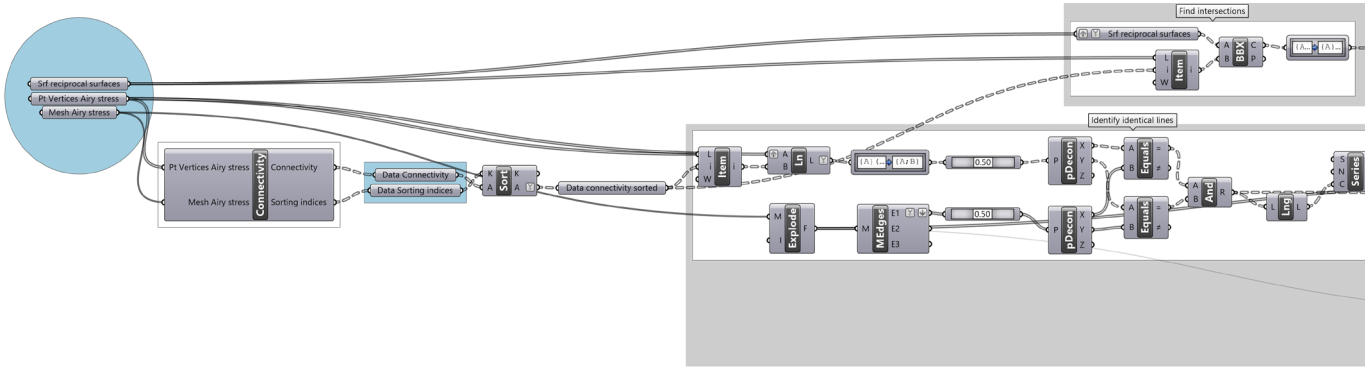

Figure F.1: Grasshopper script reciprocal figure via connectivity

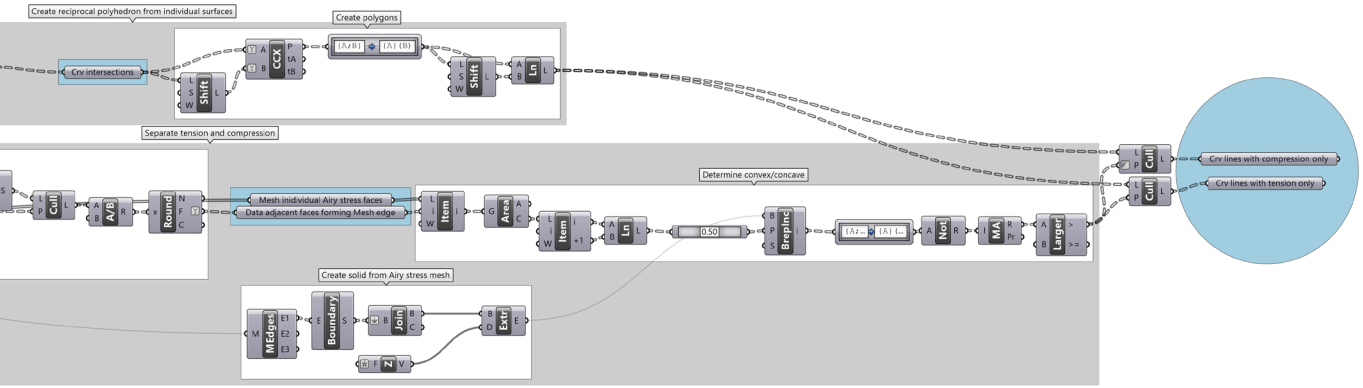
Create reciprocal polyhedron from individual surfaces
Create polygons
Crv intersections
CCX
Shift
Ln
Separate tension and compression
Cull
A/B
Round
Mesh inidividual Airy stress faces
Data adjacent faces forming Mesh edge
Item
Determine convex/concave
Area
0.50
Breps
Not
MA
Larger
Create solid from Airy stress mesh
MEdges
Boundary
Join
Extr
Crv lines with compression only
Crv lines with tension only

APPENDIX G: ADDITIONAL RESULTS PARAMETRIC TOOL CONNECTIVITY

Square shell on semi-rigid supports

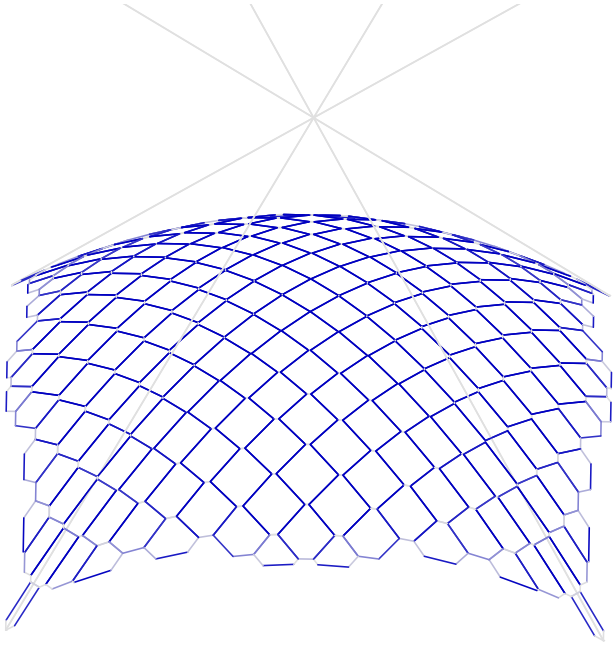

Figure G.1: Reciprocal figure of Airy stress function of square shell on semi-rigid edges with compression-only polygons

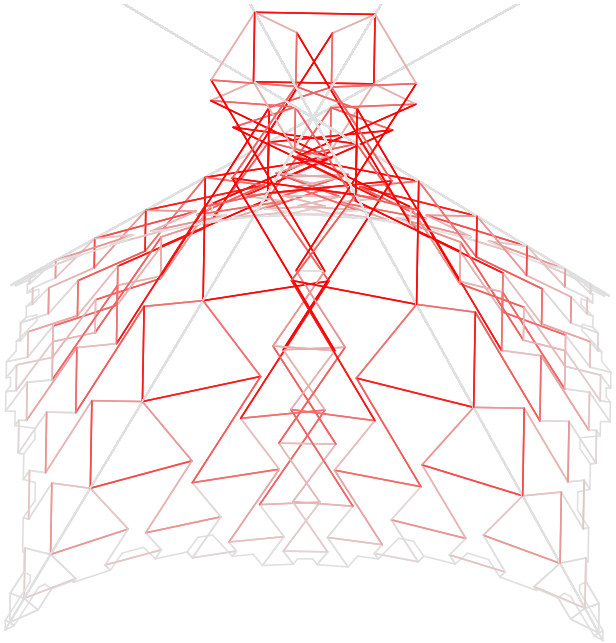

Figure G.2: Reciprocal figure of Airy stress function of square shell on semi-rigid edges with tension and compression polygons

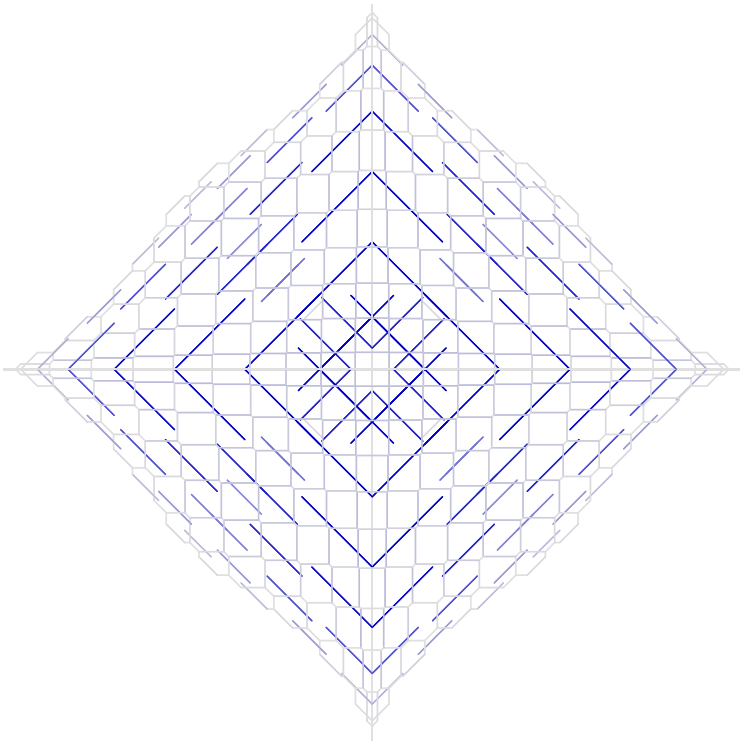

Figure G.3: Top view of reciprocal figure of square shell on semi-rigid supports with only edges in compression

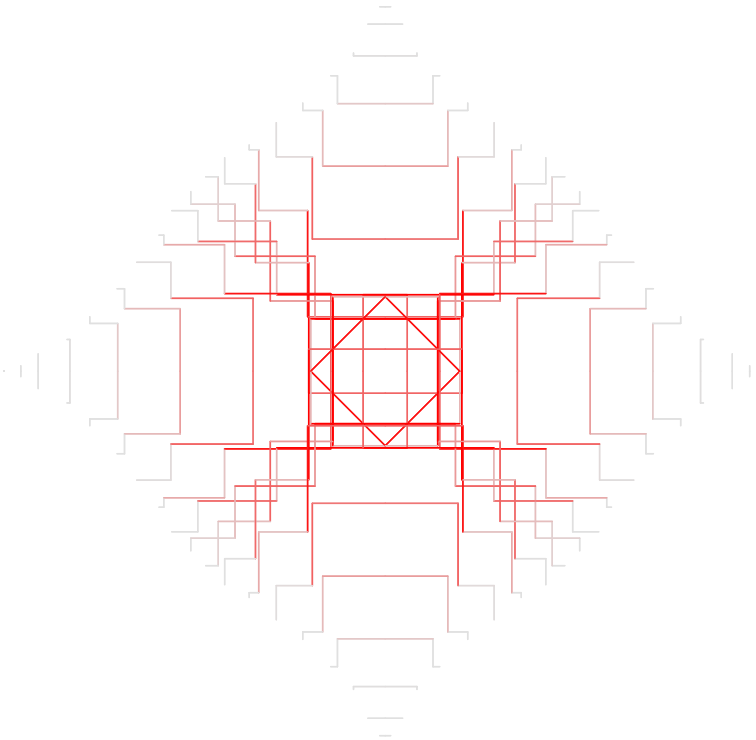

Figure G.4: Top view of reciprocal figure of square shell on semi-rigid supports with only edges in tension

Rectangular shell

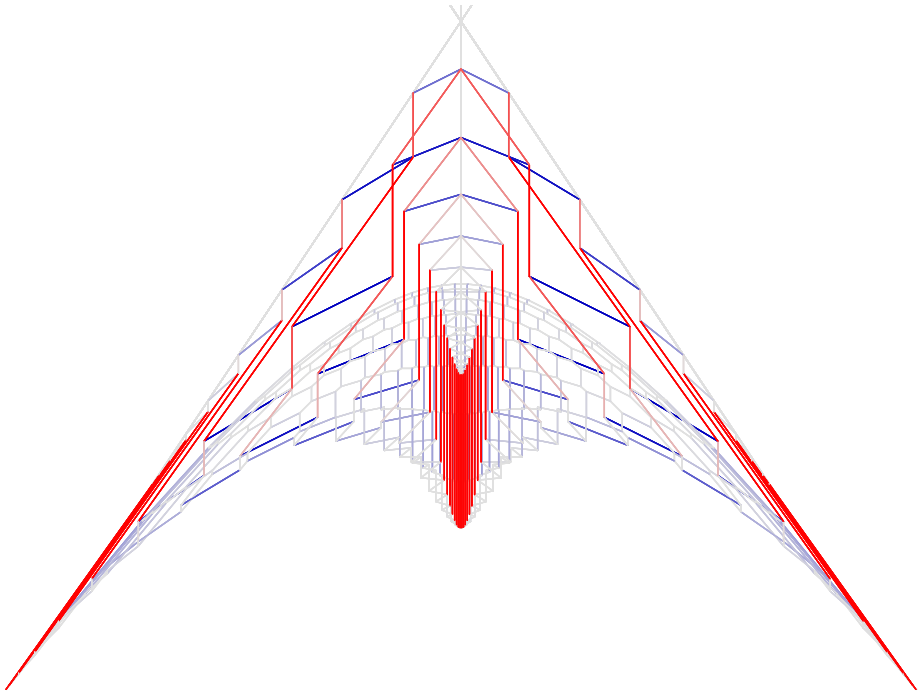

Figure G.5: Short side of reciprocal figure of Airy stress from square shell on semi-rigid supports

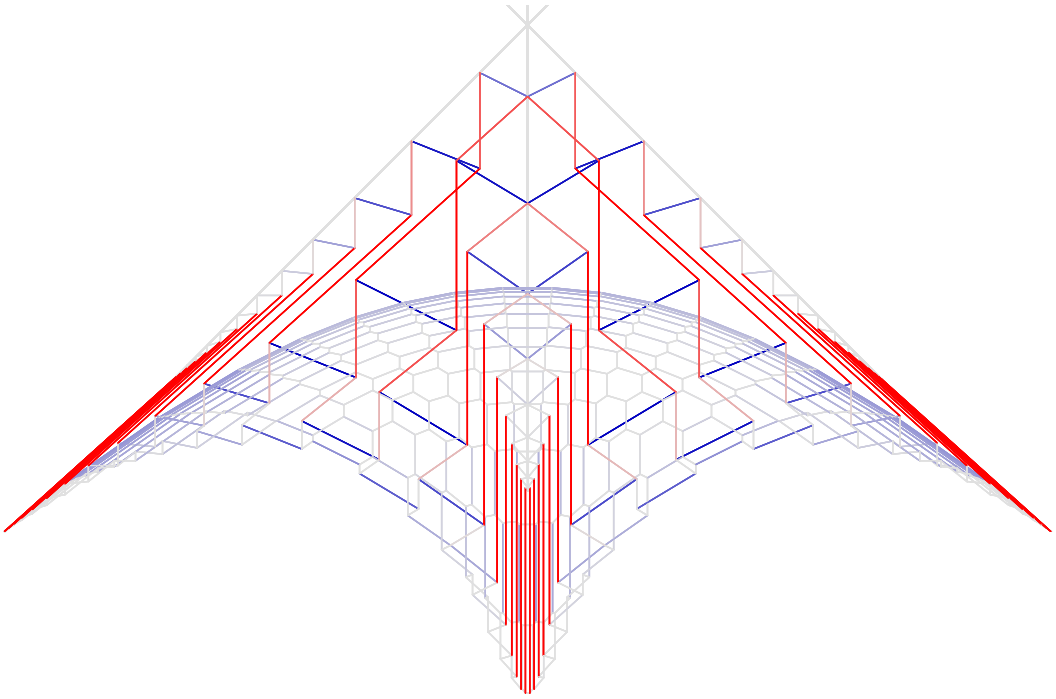

Figure G.6: Long side of reciprocal figure of Airy stress from rectangular shell

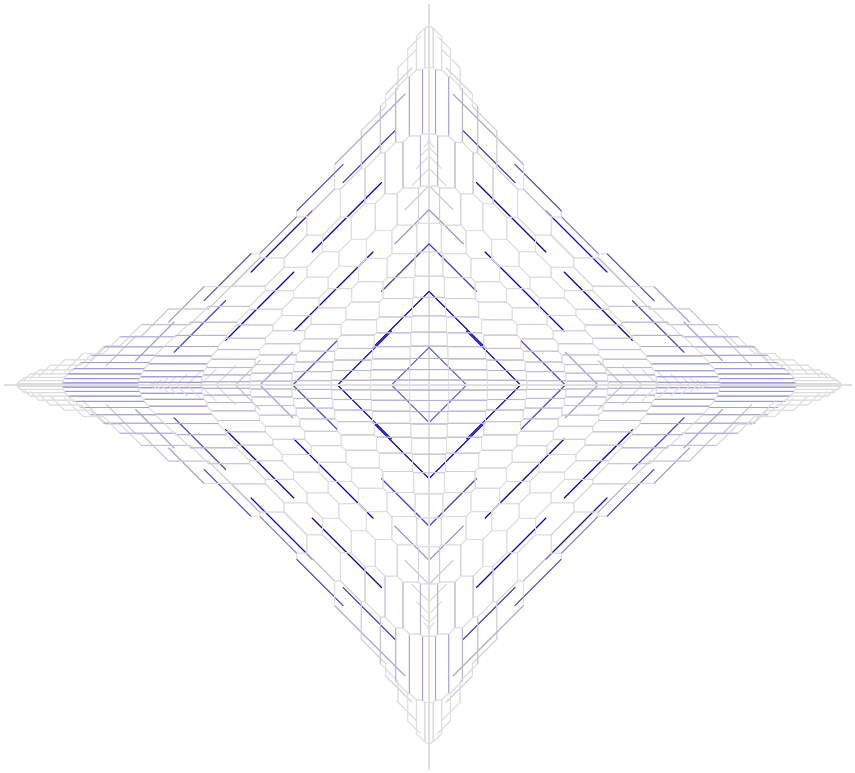

Figure G.7: Top view of reciprocal figure of rectangular shell with only edges in compression

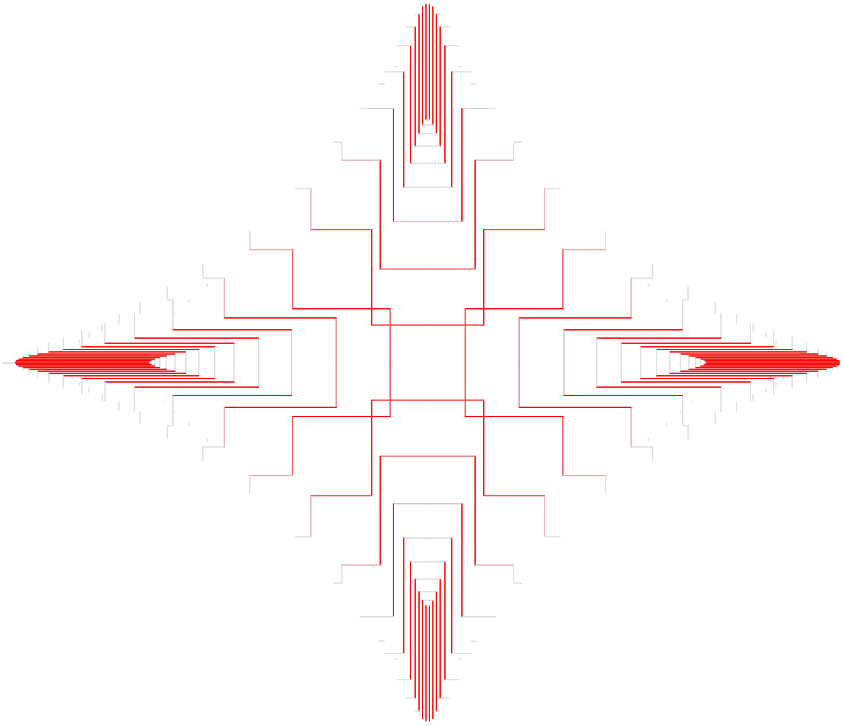

Figure G.8: Top view of reciprocal figure of rectangular shell with only edges in tension

Dome-like structure

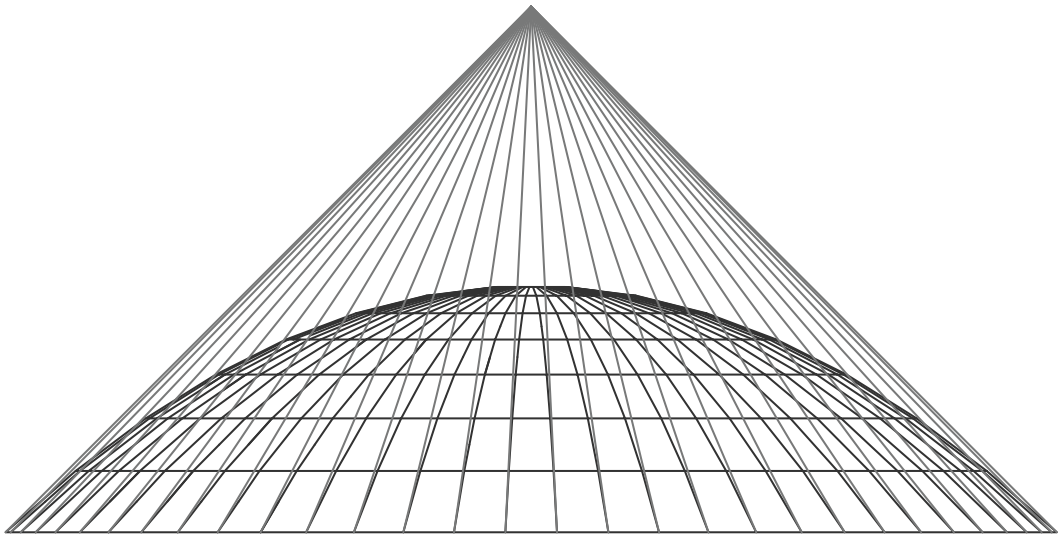

Figure G.9: Side view of reciprocal figure of Airy stress from dome-like structure

Three-valent Airy stress mesh

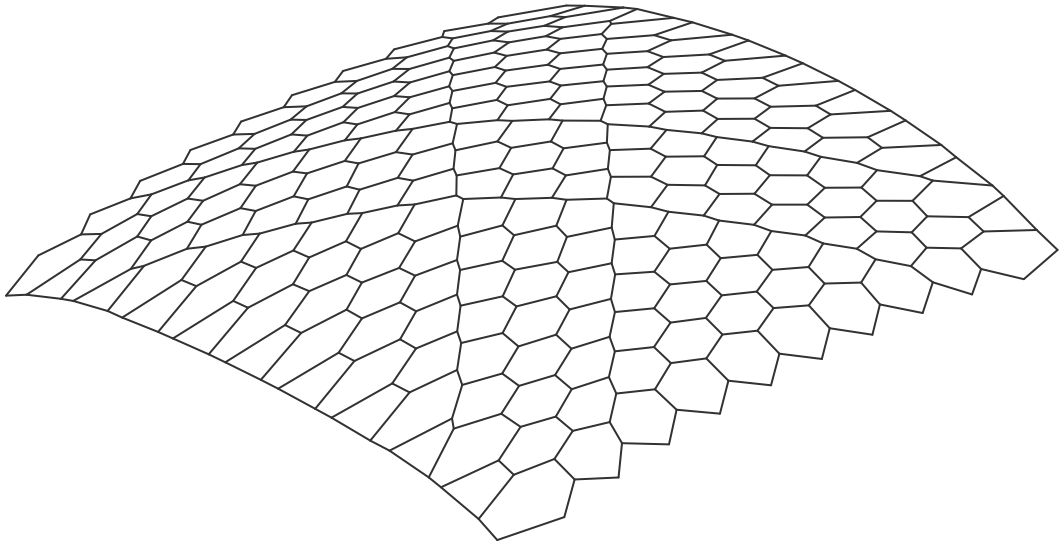

Figure G.10: Conceptual three-valent Airy stress polyhedron

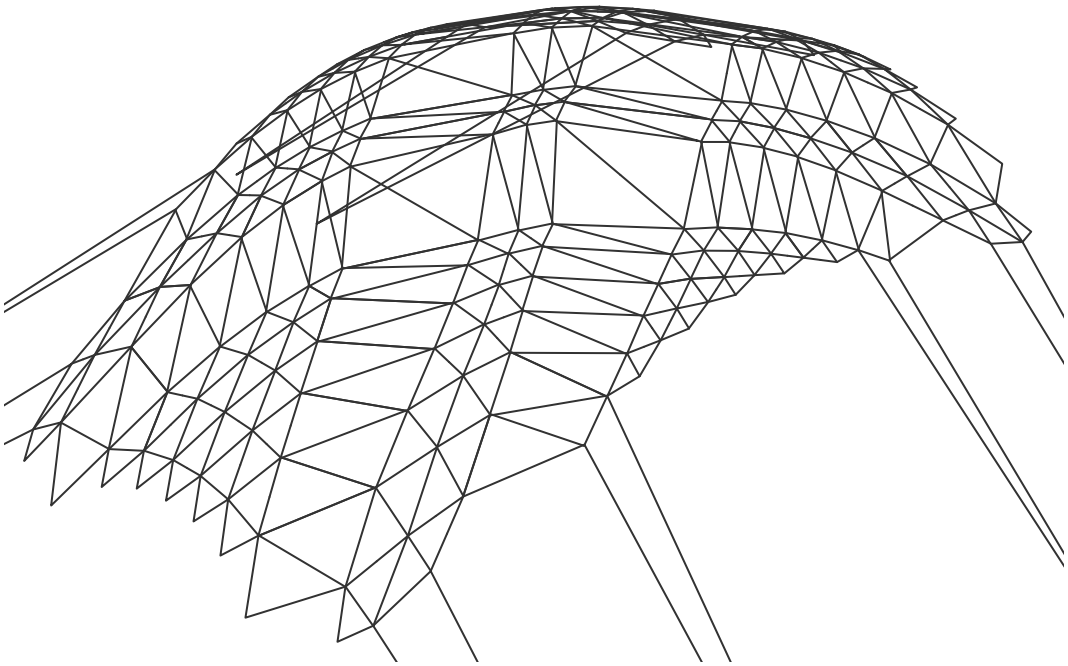

Figure 5.39: Three-dimensional view of reciprocal figure of three-valent Airy stress mesh

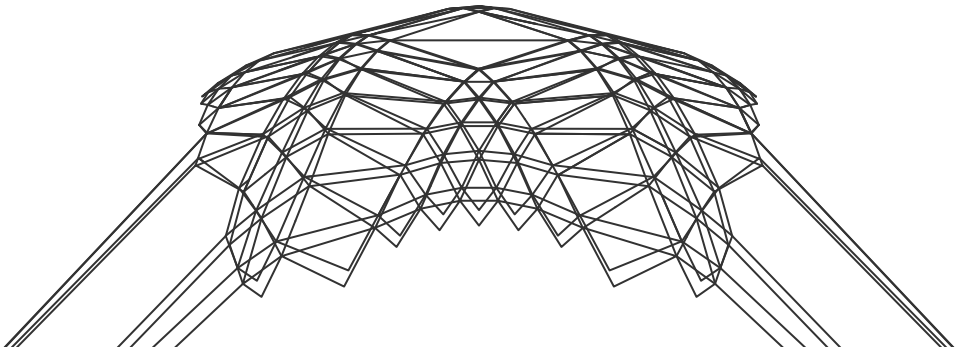

Figure G.11: Short side of reciprocal figure of three-valent Airy stress mesh

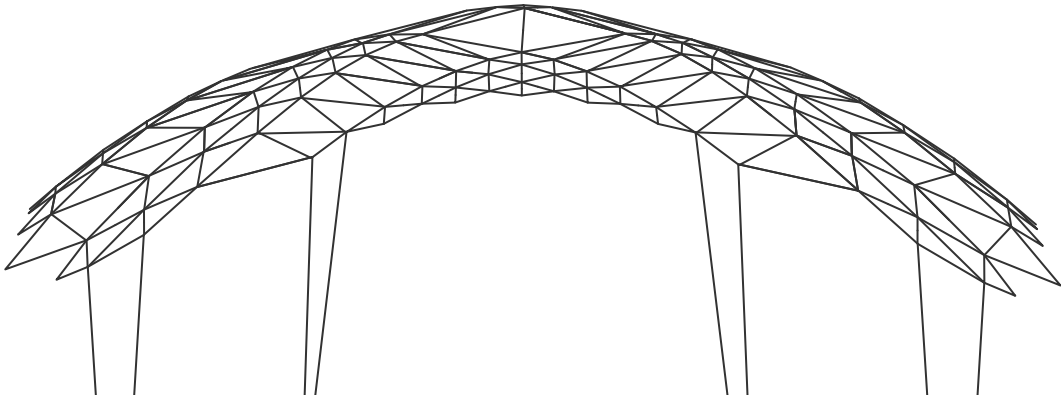

Figure G.12: Long side of reciprocal figure of three-valent Airy stress mesh

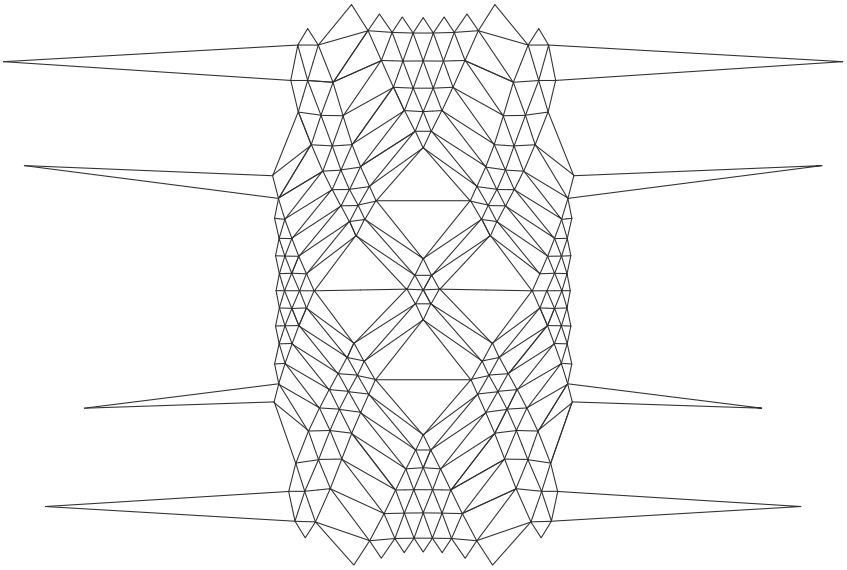

Figure G.13: Top view of reciprocal figure of three-valent Airy stress mesh